

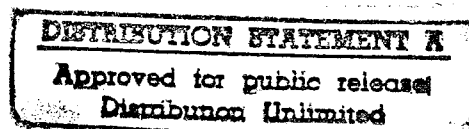
# **BIOSENSOR-BASED DETECTION AND VERIFICATION SYSTEM FOR BIO-CHEMICAL WARFARE AGENTS**

## **FINAL REPORT**

**Compiled by  
JOHN C. OWICKI**

**MOLECULAR DEVICES CORPORATION**

**8 JULY 1996**



**Sponsored by  
ADVANCED RESEARCH PROJECTS AGENCY,  
DEPARTMENT OF DEFENSE**

**DEFENSE SCIENCE OFFICE**

**ARPA ORDER NO. 8143**

**ISSUED BY DARPA/CMO UNDER CONTRACT  
#MDA972-92-C-0005**

**19960719 049**

The views and conclusions contained in this document are those of the authors and should not be interpreted as representing the official policies, either expressed or implied, of the Defense Advanced Research Projects Agency or the U.S. Government.

**DTIC QUALITY INSPECTED 4**

# REPORT DOCUMENTATION PAGE

Form Approved  
OMB No. 0704-0188

Public reporting burden for this collection of information is estimated to average 1 hour per response, including the time for reviewing instructions, searching existing data sources, gathering and maintaining the data needed, and completing and reviewing the collection of information. Send comments regarding this burden estimate or any other aspect of this collection of information, including suggestions for reducing this burden, to Washington Headquarters Services, Directorate for Information Operations and Reports, 1215 Jefferson Davis Highway, Suite 1204, Arlington, VA 22202-4302, and to the Office of Management and Budget, Paperwork Reduction Project (0704-0188), Washington, DC 20503.

1. AGENCY USE ONLY (Leave blank)		2. REPORT DATE 8 July 1996	3. REPORT TYPE AND DATES COVERED Final Report (9 Jun 91 - 9 Jun 96)	
4. TITLE AND SUBTITLE Biosensor-Based Detection and Verification System for Bio-Chemical Warfare Agents, <i>Final Report</i>			5. FUNDING NUMBERS MDA972-92-C-0005	
6. AUTHOR(S) John C. Owicki				
7. PERFORMING ORGANIZATION NAME(S) AND ADDRESS(ES) Molecular Devices Corporation 1311 Orleans Drive Sunnyvale, CA 94089			8. PERFORMING ORGANIZATION REPORT NUMBER DA9196	
9. SPONSORING/MONITORING AGENCY NAME(S) AND ADDRESS(ES) ARPA / DSO 3701 N. Fairfax Dr. Arlington, VA 22203-1714			10. SPONSORING/MONITORING AGENCY REPORT NUMBER	
11. SUPPLEMENTARY NOTES The view, opinions and/or findings contained in this report are those of the author(s) and should not be construed as an official ARPA position, policy, or decision, unless so designated by other documentation.				
12a. DISTRIBUTION/AVAILABILITY STATEMENT Approved for public release; distribution unlimited.			12b. DISTRIBUTION CODE	
13. ABSTRACT (Maximum 200 words)  The purpose of this contract was to explore and demonstrate the application of technology based on the Light Addressable Potentiometric Sensor (LAPS) to detection and verification problems for bio-chemical warfare agents. The principal analytical method employed was microphysiometry, by which perturbations of cell physiology are detected using the LAPS. The work was done in three principal segments. First, silicon microtechnology was used to design and fabricate sensor chips and microfluidic components suitable for the project. Second, a systems-engineering effort designed and assembled a prototype high-performance microphysiometer. Third, a biological effort employed a wide variety of cellular and ligand-receptor model systems to validate the generality of the method and the performance of the prototype instrument.				
14. SUBJECT TERMS Biosensor, CBW agent detection, microphysiometer, microfluidics			15. NUMBER OF PAGES 207	
			16. PRICE CODE	
17. SECURITY CLASSIFICATION OF REPORT UNCLASSIFIED	18. SECURITY CLASSIFICATION OF THIS PAGE UNCLASSIFIED	19. SECURITY CLASSIFICATION OF ABSTRACT UNCLASSIFIED	20. LIMITATION OF ABSTRACT UL	

NSN 7540-01-280-5500

Standard Form 298 (Rev. 2-89)  
Prescribed by ANSI Std. Z39-18  
298-102

DTIC QUALITY INSPECTED 4

## Table of Contents

<b>Summary of Final Report .....</b>	<b>3</b>
<b>Body of Final Report .....</b>	<b>6</b>
<b>Silicon Engineering .....</b>	<b>6</b>
• Demonstrate on-chip controlling electrode.....	6
• Demonstrate on-chip reference electrode.....	6
• Demonstrate through-chip fluidics. ....	7
• Demonstrate high-performance microfluidics. ....	10
<b>System Engineering .....</b>	<b>21</b>
• Demonstrate two-dimensional microphysiometry. ....	21
• Demonstrate prototype (breadboard) LAPS device for on-site inspection.....	26
• Demonstrate metabolic signal from tissue slices.....	27
• Demonstrate virtual electrodes for tissue slices .....	28
<b>Biology.....</b>	<b>29</b>
• Demonstrate detection of anti-metabolic agents in thawed cells using LAPS. ....	29
• Demonstrate detection of anti-receptor agents in thawed cells using LAPS.....	29
• Demonstrate detection of anti-receptor agents in rehydrated cells using LAPS .....	29
• Demonstrate detection of anti-metabolic agents in rehydrated cells using LAPS.....	29
• Demonstrate enzyme capability and sensitivity in cell-system format. ....	31
• Demonstrate immunoassay capability and sensitivity in cell-system format.....	31
• Demonstrate device gain by manipulation of transfected receptor density.....	33
• Demonstrate device gain by genetic manipulation of second-messenger system.....	33
• Demonstrate mixed-cell system for detection of secondary toxins .....	34
• Demonstrate detection feasibility with all major types of (non-transfected) neuroreceptors.....	34
• Demonstrate LAPS response with transiently transfected human ion channel receptor.....	36
• Demonstrate LAPS response with stably transfected human ion channel receptor. ...	36
<b>Appendix 1: Draft Software Manuals for Instrument..... (Bound Separately)</b>	
<b>Appendix 2: Bibliography of Publications Resulting from This Contract   ..... (Bound Separately)</b>	
<b>Appendix 3: Selected Publications..... (Bound Separately)</b>	

# **SUMMARY OF FINAL REPORT**

## **I. TASK OBJECTIVES**

Following are the 20 task objectives for the contract, grouped according to the three main technical components of the effort

### **Silicon Engineering**

- Demonstrate on-chip controlling electrode.
- Demonstrate on-chip reference electrode.
- Demonstrate through-chip fluidics.
- Demonstrate high-performance microfluidics.

### **System Engineering**

- Demonstrate two-dimensional microphysiometry.
- Demonstrate prototype (breadboard) LAPS device for on-site inspection.
- Demonstrate metabolic signal from tissue slices.
- Demonstrate virtual electrodes for tissue slices .

### **Biology**

- Demonstrate detection of anti-metabolic agents in thawed cells using LAPS.
- Demonstrate detection of anti-receptor agents in thawed cells using LAPS.
- Demonstrate detection of anti-metabolic agents in rehydrated cells using LAPS.
- Demonstrate detection of anti-receptor agents in rehydrated cells using LAPS .
- Demonstrate enzyme capability and sensitivity in cell-system format.
- Demonstrate immunoassay capability and sensitivity in cell-system format.
- Demonstrate device gain by manipulation of transfected receptor density.
- Demonstrate device gain by genetic manipulation of second-messenger system.
- Demonstrate mixed-cell system for detection of secondary toxins .
- Demonstrate detection feasibility with all major types of (non-transfected) neuroreceptors.
- Demonstrate LAPS response with transiently transfected human ion channel receptor.
- Demonstrate LAPS response with stably transfected human ion channel receptor .

## II. TECHNICAL PROBLEMS

Gaining the twenty objectives listed above requires solving a variety of technical problems ranging from several engineering disciplines to cell biology. Some of the most important included:

- Increasing the multiplicity of cell types and sensing sites in a microphysiometer flow chamber from one (in the commercial Cytosensor Microphysiometer System) to 32, while maintaining adequate signal-to-noise ratio.
- Designing and implementing a microfluidic system to deliver small ( $<100\ \mu\text{L}$ ) samples to and through the sensor chamber.
- Determining whether microphysiometry is a suitable means of detecting not only known threat agents, but as-yet unanticipated agents that may act by a variety of mechanisms that have heretofore not been exploited for CBW.
- Increasing the robustness of the cells to be used for the detection of CBW agents, so that the methodology can be used more easily outside a cell-biology laboratory.

## III. GENERAL METHODOLOGY

The twenty objectives required the application of a variety of different engineering and biological methodologies. Some of the most important included:

- Application of micromachining techniques to the MDC LAPS chip to provide a two-dimensional array of sensing spots of high multiplicity, with integrated microfluidics.
- Use of gated integration and improved analytical algorithms to improve the signal-to-noise ratio of the data acquired from LAPS, to accommodate the increased multiplicity of sensing sites.
- Integration of the improved LAPS chips into a system capable of handling a large number of small samples (96-well microplate format) in an automated fashion. The use of the LabVIEW® instrumental software development program was key to this effort.
- Use of existing Cytosensor Microphysiometer System platform to demonstrate that microphysiometry can be used to detect a broad range of types of threat agents. The utility of microphysiometry in the CBW arena depends on its ability to detect a wide variety of physiological changes in cells. The model systems investigated include not only neuroreceptors, but a variety of other cellular systems outside the nervous system that may represent targets for threat agents that are as yet unrecognized.
- Use of molecular biology and cryopreservation technologies to generate indicator cells with improved viability for applications outside the cell-biology laboratory.

## **IV. TECHNICAL RESULTS**

The technical results are grouped according to the three main components of effort: silicon engineering, system engineering, and biology. The level of documentation provided in this section depends on the complexity of the task and whether the results have already been published elsewhere (in which case a copy of the publication is in most cases included in Appendix 3).

## **V. SIGNIFICANT HARDWARE DEVELOPMENT**

A prototype high-performance microphysiometer was constructed, as described in the previous section. At a component level, a microfluidic valve technology was developed that is suitable for biological fluids.

## **VI. SPECIAL COMMENTS**

This contract ultimately was funded at 89% of the level upon which the objectives were based. The two most important objectives (prototype high-performance microphysiometer and demonstration of the broad relevance of microphysiometry for detection of CBW agents) were completed. Overall, 17 of the 20 objectives were completed; leaving three uncompleted: on-chip reference electrode, virtual electrodes, and demonstration of response to receptor activation in rehydratable cells (though responses to ion-channel blockage in rehydratable cells were observed). The completion of the objectives was in line with the resources available.

## **VII. IMPLICATIONS FOR FURTHER RESEARCH**

This work demonstrated the feasibility of detecting a broad array of CBW agents with a LAPS-based platform, principally employing microphysiometry. Additional R&D should focus on three areas:

- Additional increases in the number of cell sites per unit volume of instrument.
- Further development of rehydratable cells as indicators for anti-receptor agents.
- Additional development and exploitation of the valve technology for microfluidic biological applications.

# MAIN BODY OF FINAL REPORT

## A. SILICON ENGINEERING

- **Demonstrate on-chip controlling electrode.**

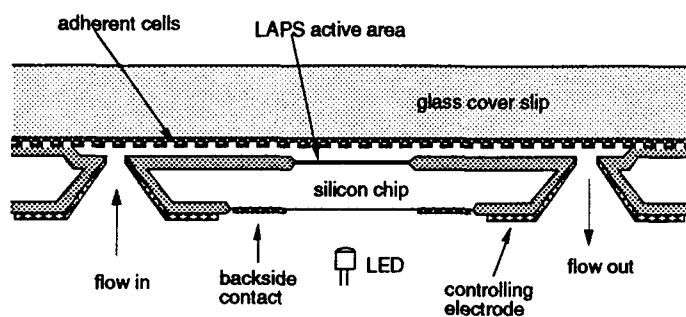
The method we used to integrate a controlling electrode on a LAPS chip was to make use of the flow-through chip shown in Fig. Si-1 [Fig. of chip X-section]. As can be seen in that figure, the holes that allow fluid flow to reach the channel in which cells are immobilized are etched from the backside only. This creates a slope of 55° with the plane of the chip, due to the angle of the crystal plane on which the etch terminates. We evaporated a layer of gold/chrome on these slopes, and connected these electrodes together with interconnects leading to a contact pad on the chip (see Fig. Si-2 for a schematic view of the back of the chip with controlling electrodes). These controlling electrodes thus made contact up to both ends of the flow channels. The resistance of the flow channel is still too high, however, for this to be an adequate controlling electrode. To reduce that resistance and allow the AC signal to be detected, the glass covers slip has a layer of conductive oxide (indium-tin oxide).

Figures Si-3 and Si-4 show examples of data gathered with the on-chip controlling electrode. This version of the chip had eight separate flow channels and one active area per flow channel.

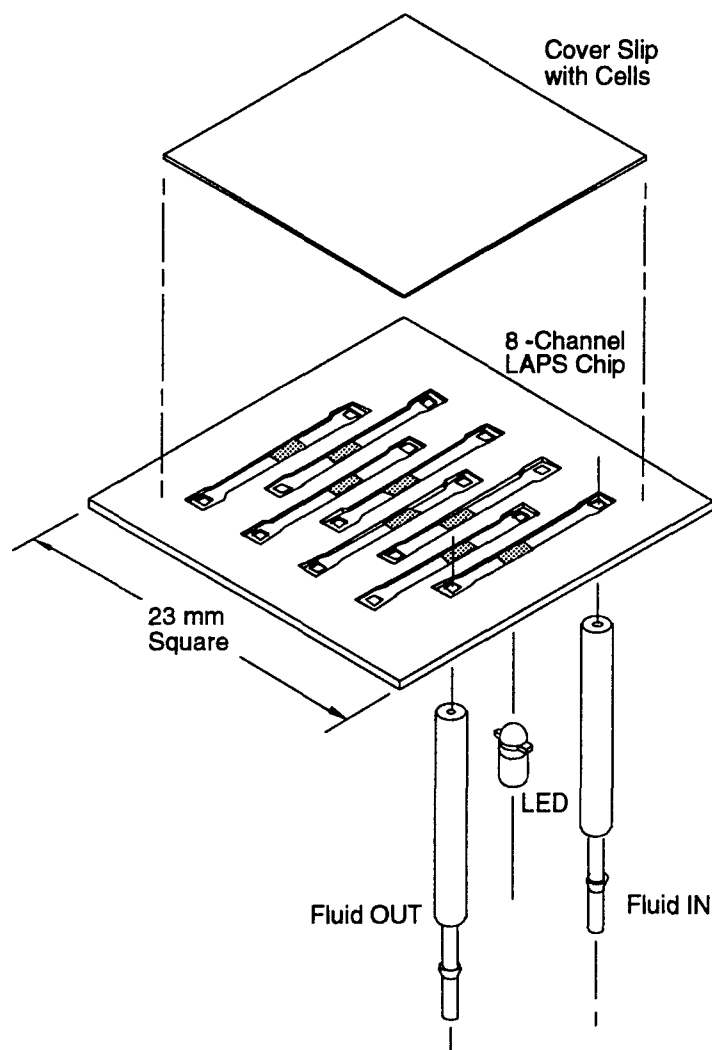
These results demonstrate the feasibility of using on-chip controlling electrodes. Subsequent versions of the flow-through chips, however, did not incorporate these integrated controlling electrodes. The main reason for this was that these electrodes significantly reduced the yield and lifetime of the chips. The controlling electrodes, the interconnect traces, and the contact pad all sit on a 1  $\mu\text{m}$  layer of oxide. Any pinholes in that oxide will cause a short that destroys the LAPS device. We found an alternative method of placing the controlling electrode near the flow channel, namely inserting a thin platinum wire in the tubing leading to the chip. This worked as well as the on-chip version, and allowed us to fabricate new versions of the sensor chip with high yields.

- **Demonstrate on-chip reference electrode.**

This task was not completed. We created a mask design for a chip that had an electrode connection near the fluid exit, where it would be possible to deposit an Ag/AgCl reference electrode. That chip has not, however, yet been produced.

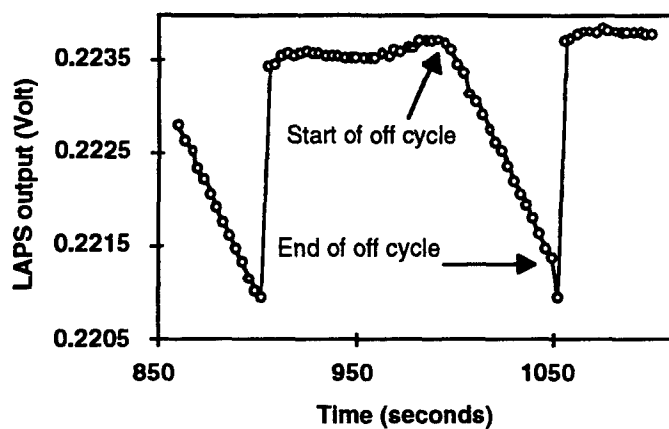


**Figure SI-1.** Cross-section of the sensor chip with on-board controlling electrode

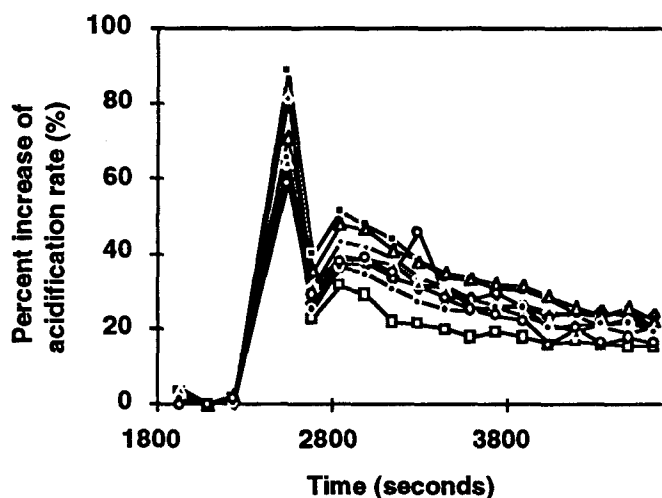


**Figure SI-2.** Three-dimensional view of the eight-channel chip with integrated controlling electrode.





**Figure SI-3.** Example of the output of a LAPS during a flow on/flow off cycle., measured on a chip using the on-board controlling electrode. The extracellular acidification is the rate of pH change during the flow off period.



**Figure SI-4.** Response of all eight channels to the introduction of 1 mM carbachol, an analog of acetylcholine, measured on a chip using the on-board controlling electrode. The cover slip contained CHO-K1 cells expressing the m1 muscarinic acetylcholine receptor.

- **Demonstrate through-chip fluidics.**

### **1. Introduction**

The key silicon component of the high-performance microphysiometer system is a multichannel flow-through chip. This section of the report describes the fabrication process with which these chips were made. There have been several versions of this chip made in the course of the project, and the evolution of the fabrication process will also be described.

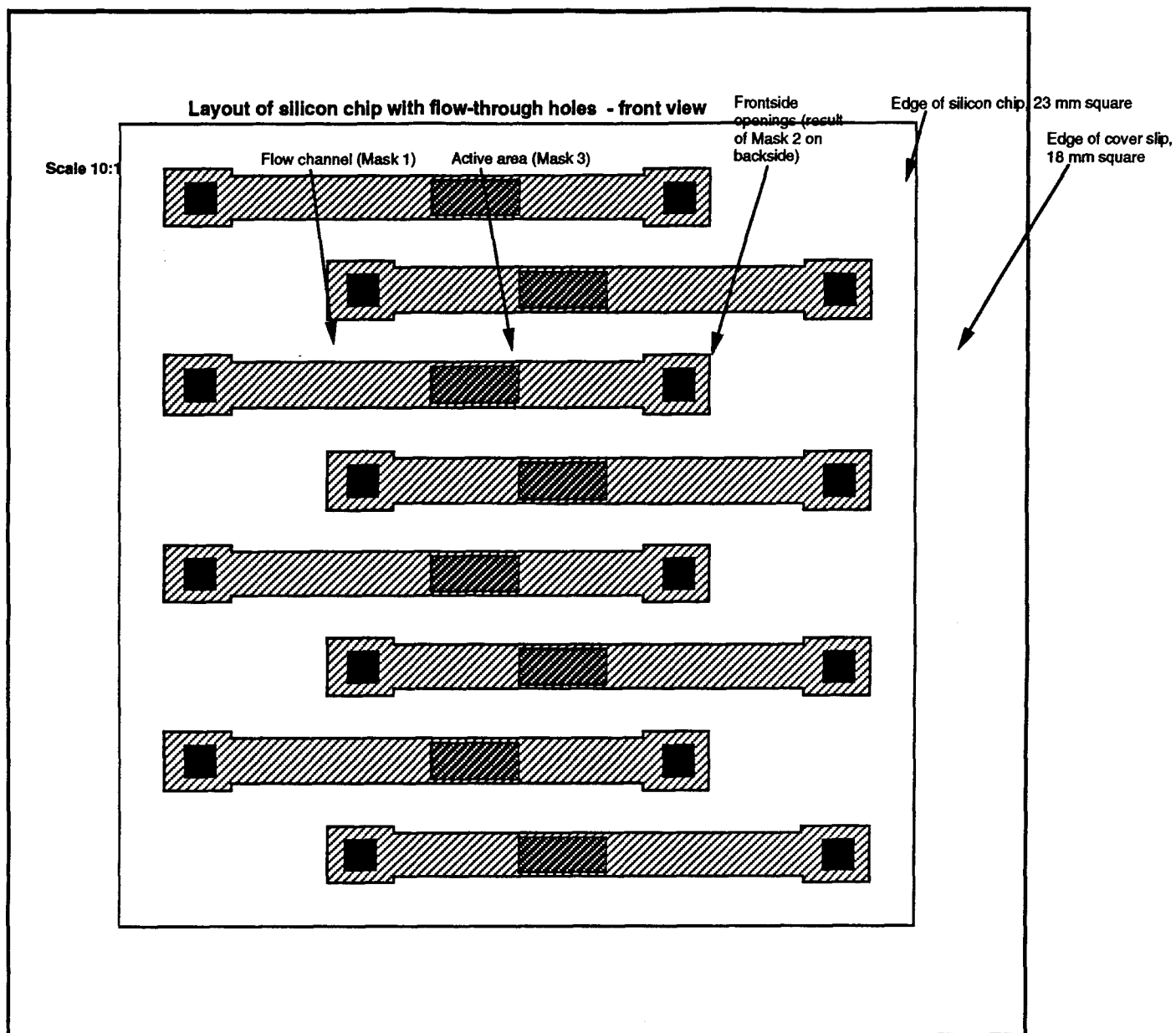
### **2. LAPS Process 1**

The original layout of the flow-through chip is shown in Figure Si-5. The first version of the chip had the following features:

- Eight flow channels, each 1 cm long, 1 mm wide, and 100  $\mu\text{m}$  deep, for a volume of 1  $\mu\text{l}$ .
- One LAPS sensing area per flow channel, with dimensions 2 by 1 mm.
- Square flow holes at the end of the flow channels.
- Single-sided anisotropic etching of the flow holes.
- Extra channel space around the opening of the flow hole, to allow for error in the back-to-front alignment (see Figure Si-5).
- A gold controlling electrode in the flow hole, with a backside contact.

All processes to be described in this section use the same starting material: 100 mm diameter silicon wafers, with double side polish, 15-30 ohm-cm, float zone material, 500  $\mu\text{m}$  thick. The processing steps were:

1. Grow 5000  $\text{\AA}$  masking oxide;
2. Pattern/etch 100  $\mu\text{m}$  deep channels frontside. This etch is an anisotropic silicon etch optimized to produce a very smooth surface.
3. Strip oxide in buffered HF, grow 1  $\mu\text{m}$  masking oxide;
4. Pattern/etch flow holes from backside, using the same anisotropic silicon etchant.
5. Strip oxide, grow 1  $\mu\text{m}$  field oxide;
6. Pattern/etch active areas: the size of the active areas is 2 by 1 mm. Note that the field oxide is retained on the backside in this step, by using a protective photoresist coating on the back during the etching step.
7. Grow 300  $\text{\AA}$  gate oxide;
8. Deposit 1000  $\text{\AA}$  LPCVD nitride;
9. Pattern/etch backside nitride and oxide in areas where the contact to the bulk silicon will be.
10. Deposit backside metal: gold, with a chrome adhesion layer for the controlling electrode portion
11. Pattern/etch backside contact and controlling electrode.



Chip Size: 23 X 23 mm

**Figure Si-5.** Layout of the first version of the flow-through LAPS sensor chip. Frontside view.

The yield of this run was low, due to two weaknesses:

1. Controlling electrode shorts to silicon. Since this electrode occupies a significant area, a very low pinhole density is needed to avoid shorts. This electrode is also vulnerable to mechanical handling, which can create these shorts.
2. The cross-section of the channel shows that there is a vulnerable piece of silicon at the flow hole opening to the channel. The insulator there can be chipped, leading to shorts from the solution to the silicon.

In spite of these problems, some working chips were obtained from this run. These chip were used to obtain the first published data on a high-performance microphysiometer system. They also led to the demonstration of the feasibility of an on-chip controlling electrode.

### 3. LAPS Process 2

In the next run, a number of changes were made to address the problems encountered in the first process. Specifically, the changes were:

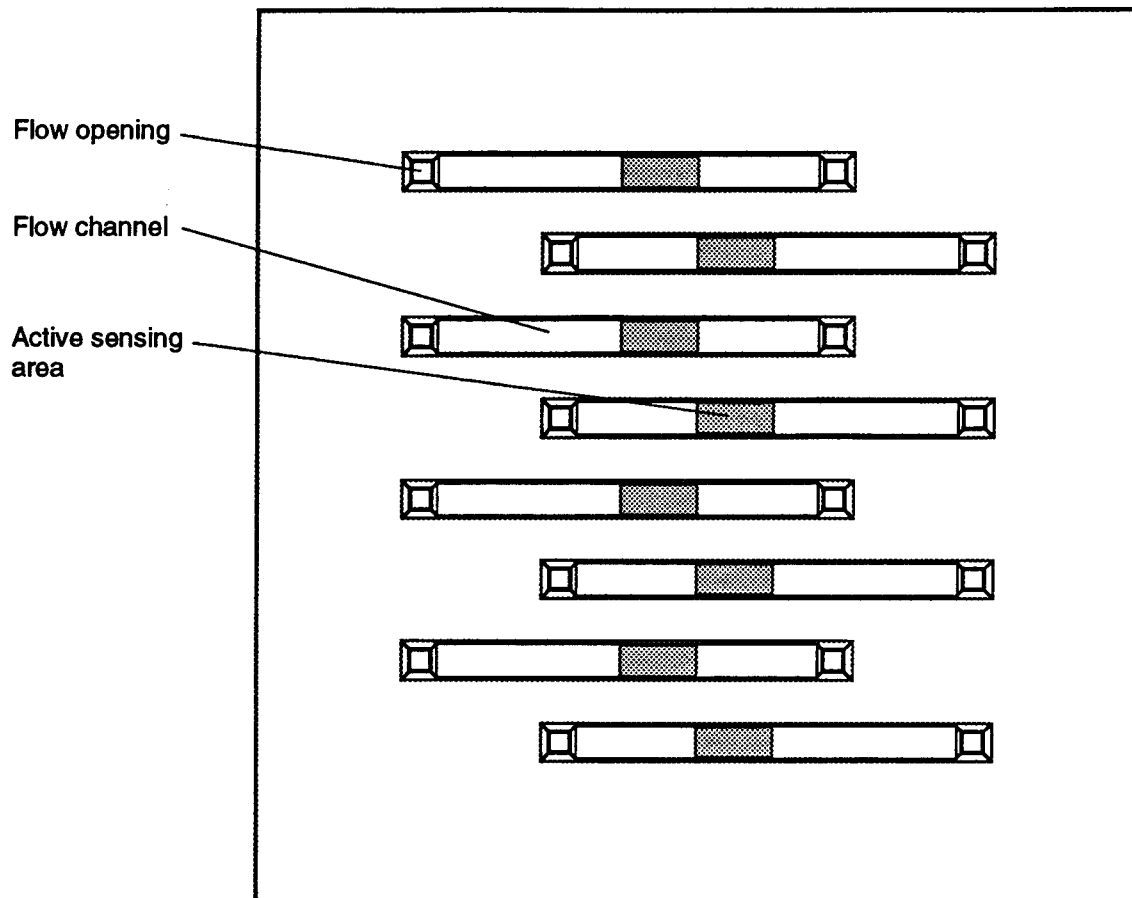
- In step 2, we added the simultaneous etching of alignment targets on the backside. The lithography for this step was done on a double-sided mask aligner which ensures accurate registration of the front and back patterns.
- In step 4, the etching was done from two sides simultaneously, thereby halving the etching time, and eliminating the section of the hole opening that was prone to chipping.
- The on-chip controlling electrode was removed to improve the yield (a pogo pin through the flow hole was used instead).
- The layout was changed to eliminate the extra channel space around the opening of the flow hole, to eliminate the dead volume this created. This became possible due to the improved back-to-front aligning accuracy. Figure Si-6 shows this new layout.
- In some wafers, the layout of active areas was changed to create four individual 1 by 1 mm active areas in each channel, for a total of 32 sensing spots. This layout is shown in Figure Si-7.

This run had good yields, and produced many chips used for the biological experiments described elsewhere in this report. The main cause of remaining problems were defects in the masking oxide which lead to etch defects during a long anisotropic etch. This is particularly severe at the edges of the wafers which are not adequately protected.

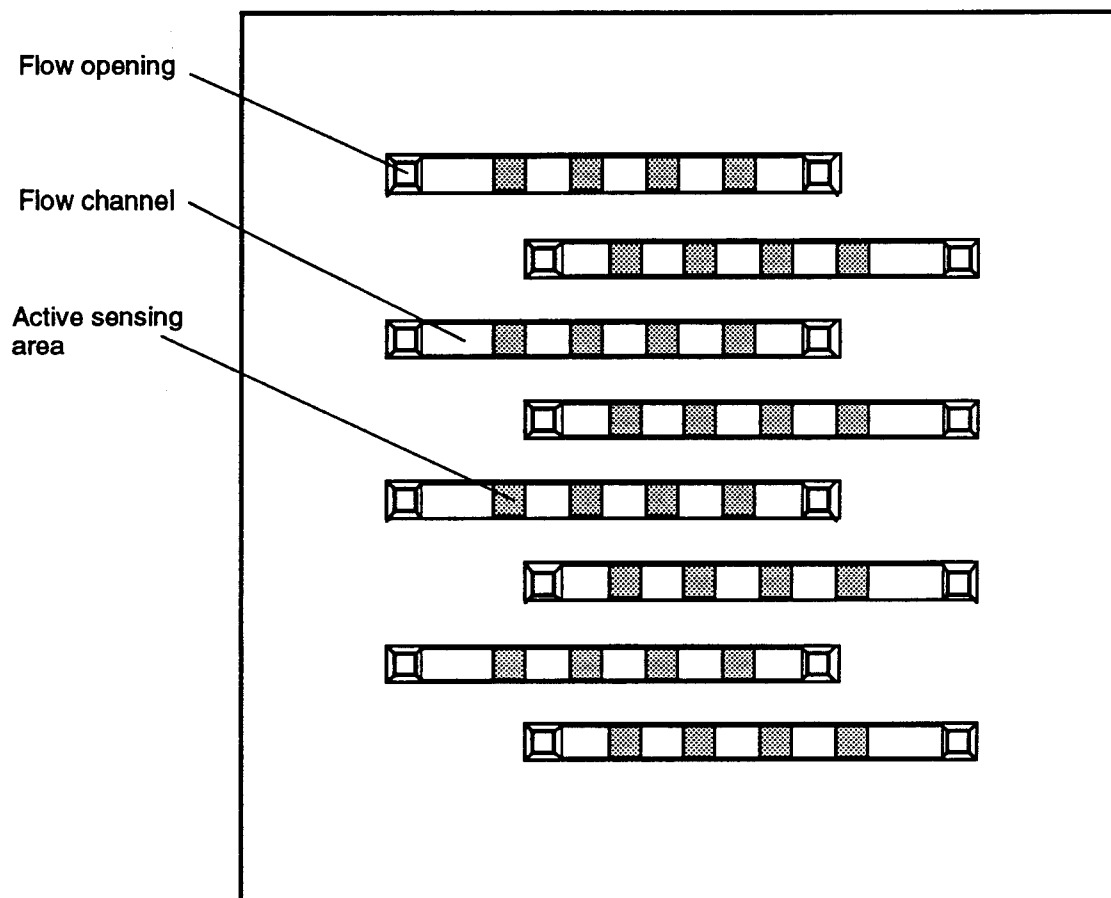
### 4. LAPS Process 3

In the next run, we used silicon nitride in addition to silicon oxide as a masking material during the anisotropic etches. Another aim of this run was to vary the channel depth. The layout of the devices was identical to the previous run, and consisted mainly of devices with 32 sensing spots. The modified fabrication process for this run was:

1. Grow thin oxide, deposit 1000 Å LPCVD nitride;
2. Pattern/etch 100 µm and 50 µm deep channels frontside, and aligned targets on the backside.



**Figure Si-6.** Layout of flow-through chip used in second and third versions of the process. This figure shows the version of the active area layout with one active area per channel.



**Figure Si-7.** Layout of flow-through chip used in second and third versions of the process. This figure shows the version of the active area layout with four active areas per channel, for a total of 32.

3. Strip oxide and nitride to bare silicon, grow thin oxide, deposit 1000 Å LPCVD nitride;
4. Pattern/etch flow holes from frontside and backside, using the anisotropic silicon etchant.
5. Strip oxide and nitride to bare silicon, grow 1.5 µm field oxide;
6. Pattern/etch active areas;
7. Grow 300Å gate oxide;
8. Deposit 1000Å LPCVD nitride;
9. Pattern/etch backside nitride and oxide in areas where the contact to the bulk silicon will be.
10. Deposit backside metal: gold, with a chrome adhesion layer for the controlling electrode portion
11. Pattern/etch backside contact.

The results of this run were: (1) the nitride masking layer was indeed superior to oxide only with respect to defect density and the quality of the wafer edges; and (2) channels shallower than 100 µm had poor fluidics performance due to the much higher shear forces on the walls.

#### **5. LAPS Process 4**

This process run was intended to establish an alternative method of drilling round holes through the wafer. This method has some potential advantages over square pyramidal holes: (1) a round hole can more easily be interfaced to round tubing; (2) the hole can be smaller and take up less volume; and (3) the round hole is easier to deal with during the subsequent active area lithography. The only changes compared to process 3 are in the following steps:

2. Pattern/etch 100 µm deep channels frontside, and aligned targets on the backside.
3. Strip oxide and nitride to bare silicon, and grow 1 µm protective oxide;
4. Drill round flow holes at each end of the channels;

This process also resulted in good yields.

#### **6. Evolution of the process used to make cover slips**

The cover slip is a critical element in the high-performance microphysiometer system, since it contains the biological component. Starting with relatively simple square pieces of unpatterned glass, cover slips gradually became more complex, and required more microfabrication.

The evolution of cover slip fabrication can briefly be described as follows:

##### Cover Slip Process 1: Commercial 18 mm glass laboratory cover slips

1. Deposit/oxidize 1500Å Indium Tin Oxide

Results: Poor dimensional uniformity, extensive edge damage and surface quality. High resistivity and operating noise.

Cover Slip Process 2: Hoya Soda Lime Optical Mask discs, 100 mm, 525 $\mu$  thick, ultra flat.

1. Deposit/oxidize 2500Å Indium Tin Oxide;
2. Deposit 300Å Cr/1  $\mu$ m Au;
3. Pattern/etch Cr/Au, in a pattern as shown in Figure Si-8.

Results: Improved in all problem areas. However, there still were gold lift off problems during the sterilization process.

Cover Slip Process 3: Same material as Process 2.

1. Deposit 5000Å Titanium;
2. Pattern/etch Ti;
3. Deposit/oxidize 2500Å Indium Tin Oxide;

Results: Good performance and wear characteristics.

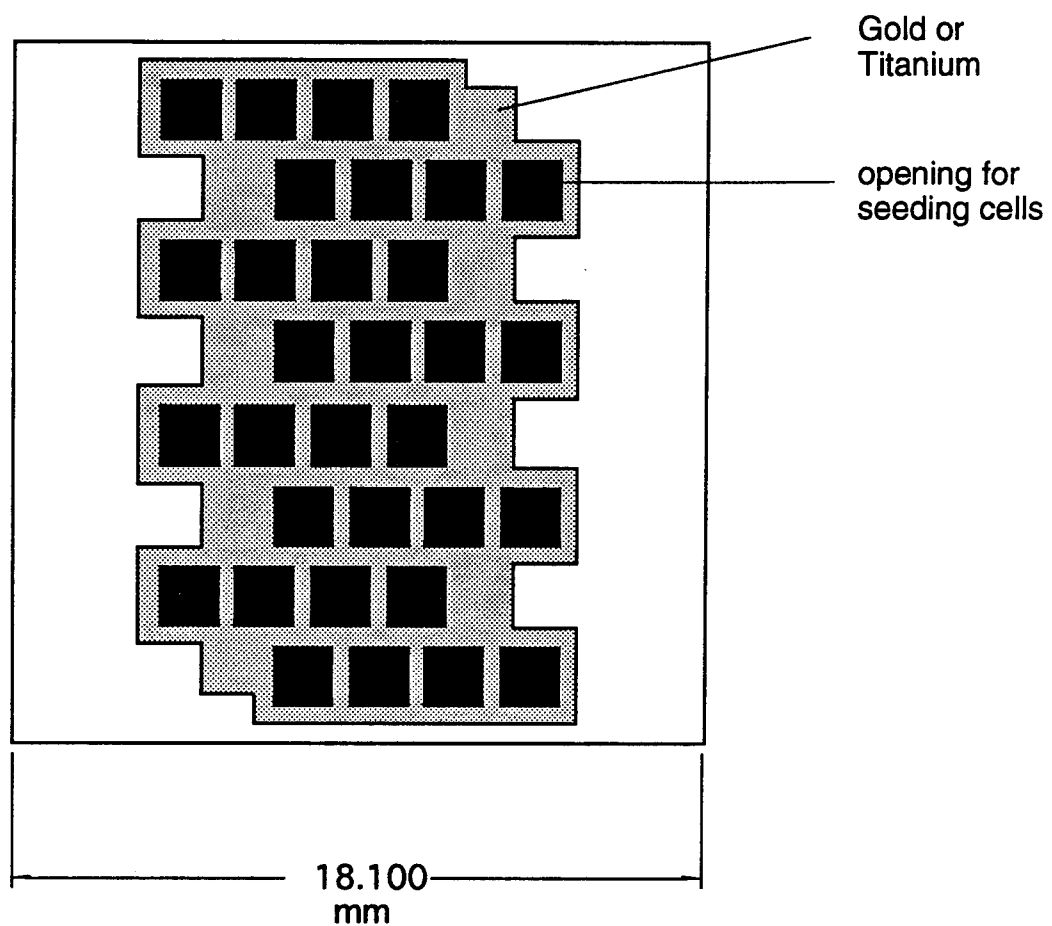
• **Demonstrate high-performance microfluidics.**

**1. Background**

The motivation for this goal is made clear, for instance, in Figure 17 of the proposal, which shows an arrangement consisting of four 4-way valves and two microphysiometry chambers. This allows, when desired, fluid that has been conditioned by going through the cells in one chamber, to be sent to another chamber. Other possible arrangements could recirculate the same fluid in a chamber for some period. All this relies on the availability of complex valve arrays. To preserve rapid response times, these arrays must have very low dead volumes, of the same order of magnitude as that of the microphysiometer chambers (1  $\mu$ L per channel in the flow-through LAPS chips). Both the complexity of the array and the low dead volume requirement make it very difficult to implement such valve arrays with conventional means. What is required is a micromachined valve array fabricated on a planar substrate with an interconnection level.

Since the application of the valve array is well-defined, it is possible to deduce the design requirements for the valve array. First, to maintain a low-volume interface between a valve array and the multi-channel flow-through chip, they have to be very close to each other and of comparable size (2.3 cm square, or 5.3 cm<sup>2</sup>). The minimum desirable number of valves is one four-way valve per flow channel, to enable fluid selection. A four-way valve needs four one-way valves to implement, and there are eight flow channels per chip. Thus, we need a valve array technology that can make 32 valves in 5 cm<sup>2</sup>, or about 6 valves/cm<sup>2</sup>. A single-chip array capable of implementing the circuit of Fig. 17 of the proposal for each pair of two channels would have to be twice as dense. Clearly, valve densities in this order of magnitude also require that the flow channels be narrow, in the order of 1 mm wide.





**Figure Si-8.** Pattern of cover slip used together with the version of the Flow-through chip with 32 sensing areas.

As will be discussed below, there is no existing technology to make valve arrays with such density. This led us to initiate work on developing such a technology. In the sections below, we will discuss the design requirements, the limitations of existing approaches, the rationale behind the technology we developed, the detailed description of the process, and the results obtained.

## **2. Design requirements**

The previous section has discussed the requirements of a valve array in terms of valve dimensions and number of valves per unit area. Another set of requirements relates to the fluidic capability of each valve. During the flow-on periods, the flow in each microphysiometer chamber is in the order of  $0.5 \mu\text{L/s}$ . To allow for some margin, each valve must thus have a maximum flow capability of at least  $1 \mu\text{L/s}$ . More importantly, during the flow-off period, the volume of medium in which the extracellular acidification is developed must not move. In the version of the flow-through LAPS chip with four sensing areas per channel, that volume is  $0.1 \mu\text{L}$  (1 mm by 1 mm by  $100 \mu\text{m}$ ). An acceptable error in the acidification rate would be less than 1%, so we are led to the requirement that there should be less than 1 nL of parasitic flow during flow-off periods. This period typically lasts about 25 seconds, and thus the parasitic flow must be below  $4 \times 10^{-5} \mu\text{L/s}$ . Combined with the flow-on requirement above, we see that five orders of magnitude of dynamic range in flow control are needed.

Another set of issues relates to compatibility. Clearly, all materials in contact with the fluid flow must be compatible with the tissue culture medium used. Also important is the issue of carryover: any surfaces or materials must not absorb compounds from the fluid stream, and then release them later.

We can summarize all these design requirements for a valve array as follows:

1. The array must be on a single substrate.
2. The size of each valve must be such that at least about 10 valves/cm<sup>2</sup> can be reached (equivalent to about 3 by mm per valve), including interconnects.
3. Interconnections between valves should be 1 mm or less wide, and have dead volumes of  $1 \mu\text{L}$  or less
4. On-rates (flow when valve is open) must be at least  $1 \mu\text{L/s}$ , with a pressure drop below 1 psi.
5. Off-rates (flow when valve is closed) must be below  $4 \times 10^{-5} \mu\text{L/s}$  at 5 psi.
6. All materials must be compatible with tissue culture media.
7. Carryover of compounds from one experiment to the next is nonexistent or acceptably low.

## **3. Description of previous technology**

Having listed the precise requirements for our high-performance microfluidics, the logical next step is to investigate whether existing technology can meet these requirements. This section will briefly review the current state of the art in microvalves and microfluidics.

One obvious method of making small valves is to use modern microfabrication and micromachining technology, in particular silicon microfabrication. Several workers have

made valves in this way. Mostly these are valves for gases, and cannot be applied to liquids, because the actuation mechanism is exposed to the flow. A conductive liquid would cause electrical shorts, and could also conduct away heat used in actuation. A good review of existing microvalve technology has recently been published by Gravesen et al. [1].

There are, however, a few examples of valves or pumps made for liquid flow (pumps use similar technology, and usually include one-way valves). These include the van der Schoot pumps and valves [2], which use a 10 mm piezoelectric disc, and similar work by Esashi et al. [3] using a macroscopic (relatively large) piezoelectric stack. Zdeblick et al. [4, 5] have demonstrated valves with thermopneumatic actuation; the normally-open version of these devices can switch both liquids and gases, and is about 6 mm on a side. Valve arrays using thermopneumatic technology have not yet been demonstrated. Other references that describe the state of the art for microvalves can be found in Ref. [1].

Therefore, although the valves listed above are fabricated with silicon technology and photolithography, their size is in the range of 6 to 10 mm on a side, corresponding to a density of 1 to 2 valves/cm<sup>2</sup>. This is inadequate for our needs. Part of the problem is the nature of the flexible membrane: because only a limited amount of flexing can be obtained from a rigid material such as silicon or glass, a large membrane is needed to obtain any appreciable displacement perpendicular to the membrane. Thus, using a rigid material as a membrane will typically preclude attaining the density we require.

Recently, some work has been reported in which polymeric moving membranes are used in microvalves or micropumps. One of the polymers used is polyimide, which is about 70 times less stiff than silicon. A micropump about 5 mm on a side has been reported [6], made with thermoplastic molding. Other authors have used negative photoresist [7], or silicone rubber [8]. The work by Vieider et al. is particularly significant in that they demonstrate arrays of valves with a density of at least 2 cm<sup>-2</sup>, and potentially much more [8]. Another example of valve arrays using rubber membranes has been described in the patent literature, but that work does not use micromachining technology or photolithographic definition of features, so it is limited to what can be achieved with conventional machining. This makes it difficult to achieve the dimensions and density we are aiming for.

#### **4. Choice of a valve array technology**

As mentioned above, one of the obstacles to high valve densities is the need for high displacements in small distances. More specifically, a valve for fluids must be capable of opening in the order of 50 to 100  $\mu$ m. Smaller openings, while suitable for gas valves, create too much flow resistance for liquids, and become vulnerable to clogging by particulates. Also, the flow channel must be less than 1 mm wide. So we need a displacement of 100  $\mu$ m in at most 500  $\mu$ m (half the flow channel width). It is intuitively obvious that it is difficult or impossible to achieve such bending in rigid materials such as silicon or steel. The strain will be too high, and the membrane will tend to break. In addition, the force needed to achieve such large displacements in rigid materials is very high.

In the theory of beams or plates, the displacements under a given force and for a given geometry are always inversely proportional to the stiffness, or Young's modulus, of the material used. In most structural problems, a high Young's modulus is desirable; in this case however, since we want large displacements in a short distance, we need a low Young's modulus. The following table shows the stiffness of some common materials, including those used in silicon micromachining:

Table of Youngs's Modulus (in MP	
silicon	190,000
SiO <sub>2</sub>	73,000
steel	210,000
polyimide	3,000
silicone rubber	1

Clearly, the largest decrease in Young' modulus occurs in going from rigid polymers such as polyimide (available as flexible thin films but also as rigid materials such as Ultem™) to elastomers such as silicone rubber: the modulus goes down by a factor of about 3000. On the other hand, replacing silicon by polyimide reduces the modulus only by a factor of about 60. Note that for elastomers the load/deflection characteristics are actually dominated by the magnitude of the internal stress [9, 10] . However, this does not alter the fact that elastomers provide the highest displacement for a given load of all the materials in the table above. The type of elastomer we choose to be most compatible with silicon microfabrication technology is silicone rubber.

The use of silicone rubber has several other advantages. First, it is easily deformable, and the strain achievable before rupture is in the order of 100%. This means that the rubber conforms in shape to other rigid surfaces and acts as a tight seal. This is, of course, why elastomers are always used in applications where tight seals are required. Second, silicone rubbers are hydrophobic, which enhances their sealing ability. Finally, silicone rubber is chemically resistant. No materials likely to be encountered in biological applications will cause compatibility problems.

The type of rubber we have used is a heat-curing silicone rubber. The chemistry is that of an addition-cure silicone rubber, which has the property of forming covalent bonds with most surfaces such as glass, ceramics, and many metals. In the context of silicon technology, this material will therefore strongly adhere to silicon, silicon dioxide, silicon nitride, etc. This has the advantage of permanently attaching the thin membrane layer to a rigid substrate, and avoids the need to manipulate loose membranes. However, to use a silicon rubber membrane as the movable element of a valve implies that in some areas the rubber must be free, and not adhere to a rigid substrate. To achieve this, we have developed a sacrificial layer technique. This method allows the areas where the rubber is free to be defined by a lithographic process on a wafer scale, with excellent spatial resolution.

This concept of a sacrificial layer is inspired by the extensive body of work in which layers of silicon dioxide and polysilicon are deposited and patterned in sequence on a silicon substrate. The silicon dioxide layers are sacrificial, and at the end of the fabrication procedure they are selectively etched away in hydrofluoric acid. This frees

the polysilicon structures, some of which can become free to move, subject to constraints such as bushings, bearings, etc. This type of technology has been called surface micromachining. In this way, structures such as electrostatic micromotors or vibrating structures can be made.

## **5. Description of the valve fabrication technology**

This section describes the process used in the first device fabrication run. In this run, only individual valves were made, but with a wide range of geometrical parameters. Valve arrays and four way valves were made in a second fabrication run, to be described later on.

### **5.1 Description of the rubber deposition technology**

In order to make small valves, silicone rubber is used as the flexible membrane material. The material we use is a heat-curable silicone designed for high strength, and for bonding tightly to other surfaces. Prior to curing, the silicone is a viscous liquid (about 100 poise). In silicon processing, the usual method for applying coatings with uniform and controlled thicknesses to a wafer is spin coating. In the case of photoresists, the usual viscosities are about 100 times lower than for the silicone rubber, and the resulting thickness is in the order of 1  $\mu\text{m}$ . We can therefore expect rubber thicknesses in the order of 100  $\mu\text{m}$ .

This is in fact what was observed. Fig. Si-9 shows the rubber thickness after heat curing as a function of the spin speed. We see that the thickness can be controlled between 50 and 120  $\mu\text{m}$ . The uniformity of thickness is also good in almost all of the wafer, apart from an edge bead, and a peak in the middle of the wafer.

Thus, a rubber deposition technology that is compatible with standard wafer processing was developed and characterized. The range of thicknesses around 50 to 70  $\mu\text{m}$  was found to be good in terms of the required strength and resistance to applied pressure.

### **5.2 Sacrificial layer technology**

To define the flow channels between the rubber and the rigid substrate, a sacrificial layer is photolithographically patterned between the rubber and the substrate. The simplest type of sacrificial layer in this case is photoresist. Use of photolithography allows very accurate definition of this pattern. Subsequent removal of the sacrificial layer will then create a region where the rubber is not bonded to the substrate, and where flow can occur. To provide access to the flow channel, holes have to be made through the rigid substrate. There are a number of techniques for doing this, such as anisotropic etching of a silicon wafer.

Fig. Si-10 shows a cross-section of the type of valve structure we have fabricated. The operation of this device requires a force to be applied on the rubber membrane to close the valve. This can be done by several possible means: pneumatic, hydraulic, or a mechanical actuator. The simplest method, which we have used in testing the devices,

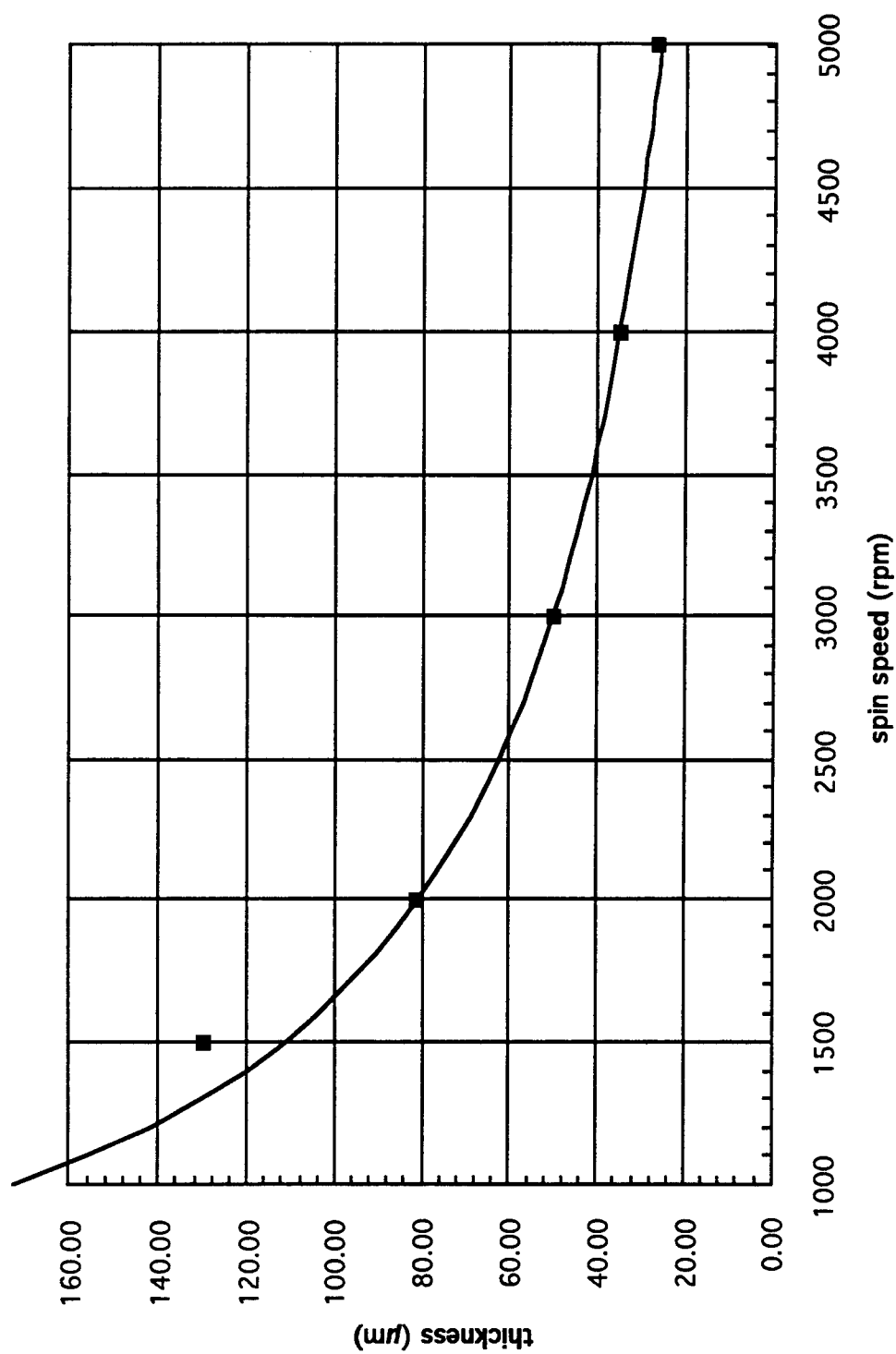


Figure Si-9. Thickness of Silicone Rubber vs. Spin Speed

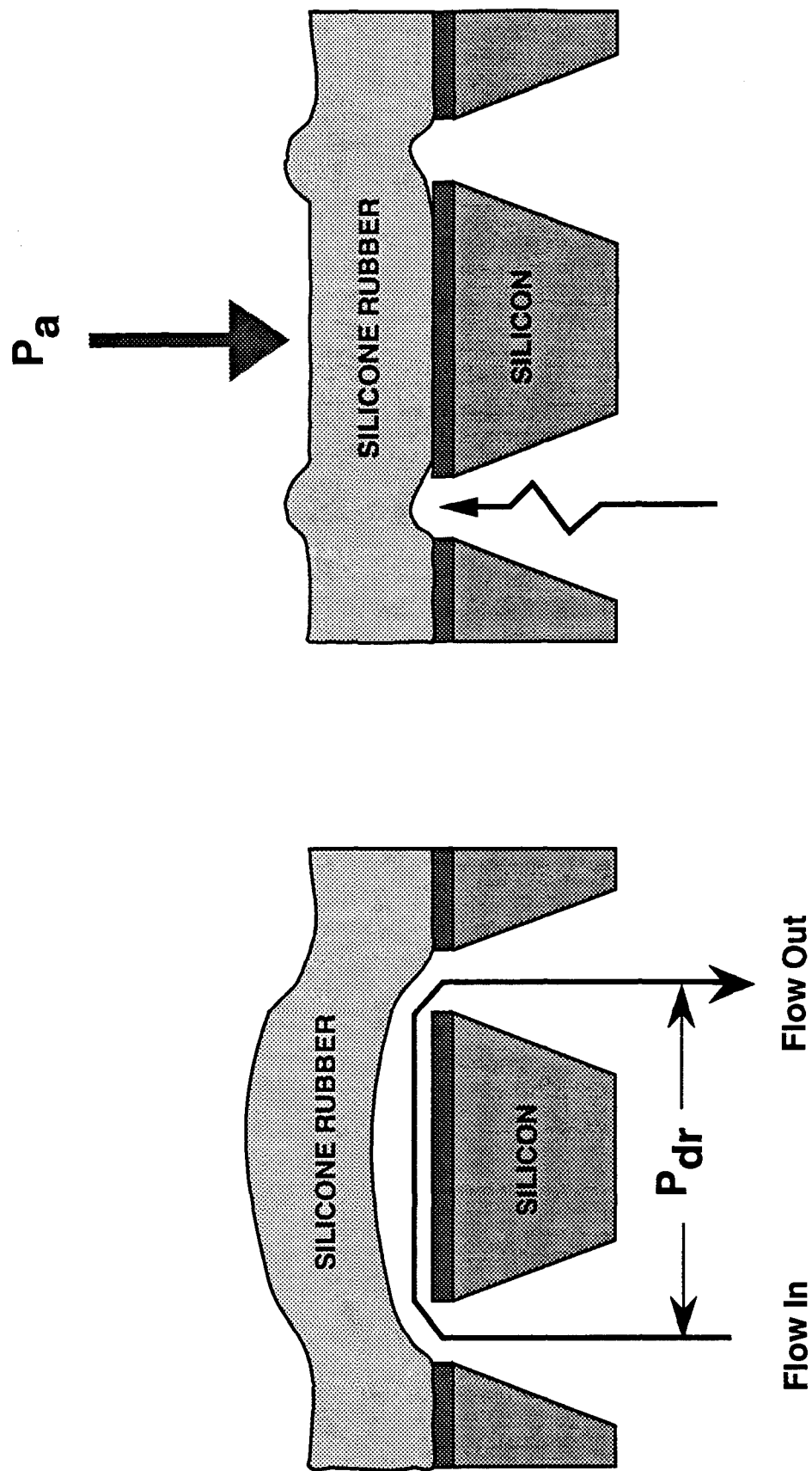


Figure Si-10. Basic Structure for Microvalve Arrays

is pneumatic. To close the valve, an amount of air pressure is applied to the top of the rubber membrane greater than the fluid pressure driving liquid through the valve.

### 5.3 Detailed process flow

The exact process we used to fabricate the valves is schematically illustrated in Fig. Si-11. It contains the following steps:

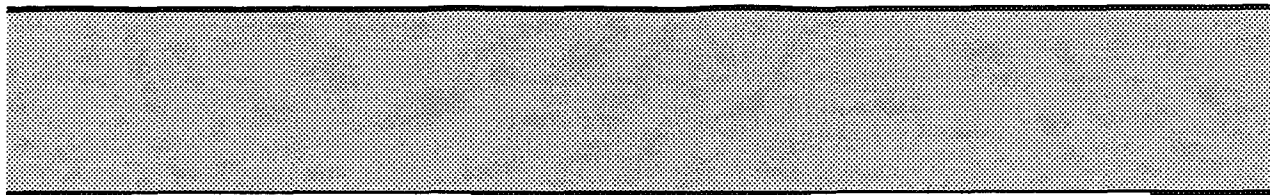
1. Starting material: 100 mm diameter silicon wafers, low-doped n-type, (100) orientation, 525  $\mu\text{m}$  thick.
2. Oxidation in a wet ambient, to form a 1  $\mu\text{m}$  thick oxide on both sides.
3. Photolithographically define openings in the oxide on the backside.
4. Spin-coat photoresist on the frontside of the wafer. In alignment with the hole pattern on the backside, pattern this layer to form the future flowchannels.
5. Spin-coat uncured silicone rubber on the frontside, on top of the photoresist.
6. Heat-cure the rubber. This also hard-bakes the photoresist underneath. The resulting thickness of the rubber layer is 30 to 120  $\mu\text{m}$ , depending on the spin coating speed.
7. Etch holes in the silicon from the bottom in an anisotropic etchant. This is done in a one-sided silicon etch fixture, so that the rubber on the frontside of the wafer is not damaged by the etchant. This etch step self-terminates when the oxide on the other side of the wafer is reached.
8. Etch the oxide windows in buffered HF, which also removes all the oxide exposed on the backside.
9. Removing the sacrificial photoresist layer. This is done by immersing the wafer in Microposit resist removing solution (Shipley), at about 80 to 100  $^{\circ}\text{C}$ . This solution is capable of penetrating through the silicone rubber, and liquefies the photoresist underneath the rubber. To remove the photoresist/Microposit solution in the long channels, ultrasonic agitation is very effective.
10. The wafer is diced in the conventional way; the presence of the rubber layer does not present a problem.

## 6. Test results

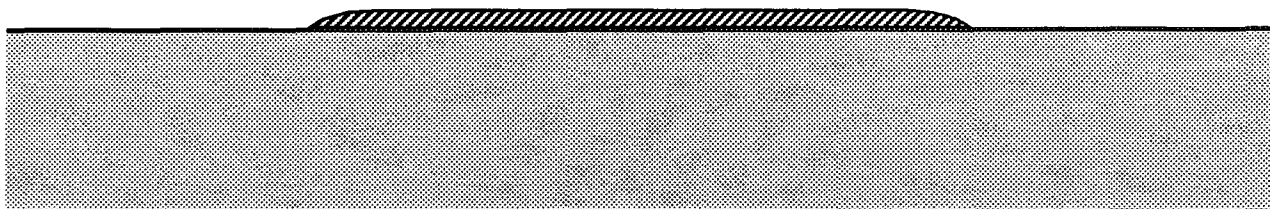
The geometrical parameters that describe each individual valve are shown in Fig. Si-12. They are: (1)  $W$ , the width of the fluid path, which varied from 250  $\mu\text{m}$  to 1750  $\mu\text{m}$ ; (2)  $L$ , the length of the fluid path, which was either 1900  $\mu\text{m}$  or 1400  $\mu\text{m}$ ; (3)  $HW$ , the width of the opening through the silicon seen at the front side, which was either 250  $\mu\text{m}$  or 550  $\mu\text{m}$ . A fourth important parameter is the thickness  $T$  of the sacrificial photoresist layer. Wafers with thicknesses of that layer of 26.5  $\mu\text{m}$ , 9.2  $\mu\text{m}$ , and 2.8  $\mu\text{m}$  were tested.

Testing consisted of measuring flow as a function of the air pressure applied to close the valve ( $P_{cl}$ ) and the pressure drop across the valve that drives the flow ( $P_{dr}$ ). Pressures were measured with solid-state pressure transducers. Two methods were used to measure liquid flow. For moderate to high flows, the measurement was gravimetric: determine the amount of water that entered a capture vessel in a given time by weighing. Precautions were taken to minimize errors caused by evaporation. For low flows (below 0.1 to 0.01  $\mu\text{L/s}$ ), this method is no longer accurate enough. The second method, used in the low flow regime, is to measure the rate at which a bubble travels in

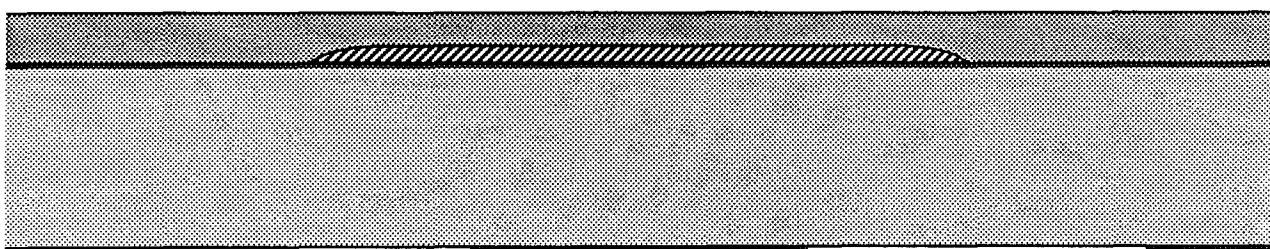




**Step 1.** Oxidize the silicon wafer to a thickness of  $1\text{ }\mu\text{m}$ , and photolithographically pattern the oxide on the bottom of the wafer.

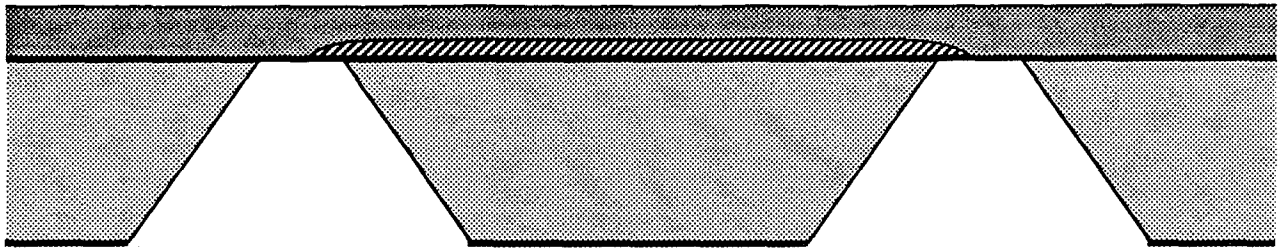


**Step 2.** Pattern a layer of controlled thickness of positive photoresist on the top side of the wafer, in alignment with the pattern on the bottom side.

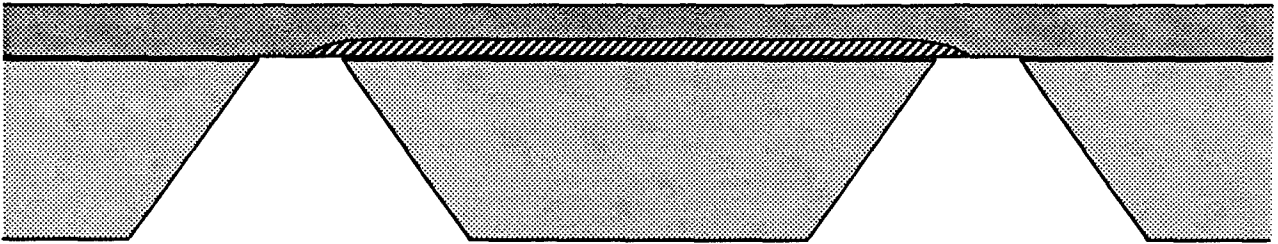


**Step 3.** Spin-coat uncured silicone rubber (about  $100\text{ }\mu\text{m}$  thick) on top of wafer, and heat-cure.

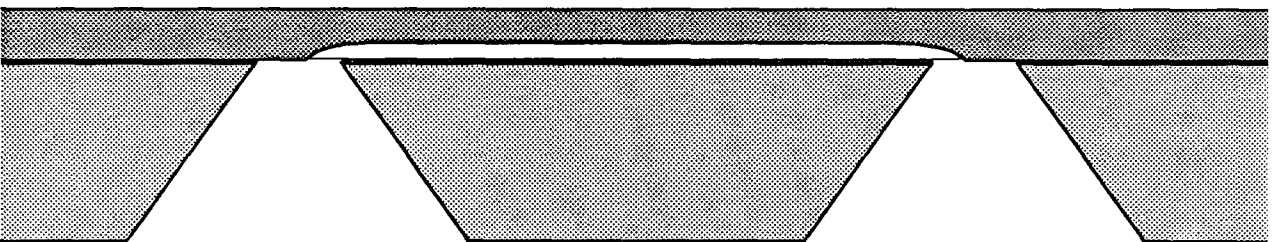
**Figure Si-11a.** Description of the process for making rubber-membrane sacrificial layer valves



**Step 4.** Place wafer in special fixture for one-sided etching. Anisotropically etch openings through the wafer, terminating at the oxide layer at the top.



**Step 5.** Etch away oxide using buffered HF, thereby exposing the photoresist.



**Step 6.** Remove sacrificial photoresist using hot Microposit resist remover (Shipley), with ultrasonic agitation as needed.

**Figure Si-11b.** Description of the process for making rubber-membrane sacrificial layer valve (copntinued).

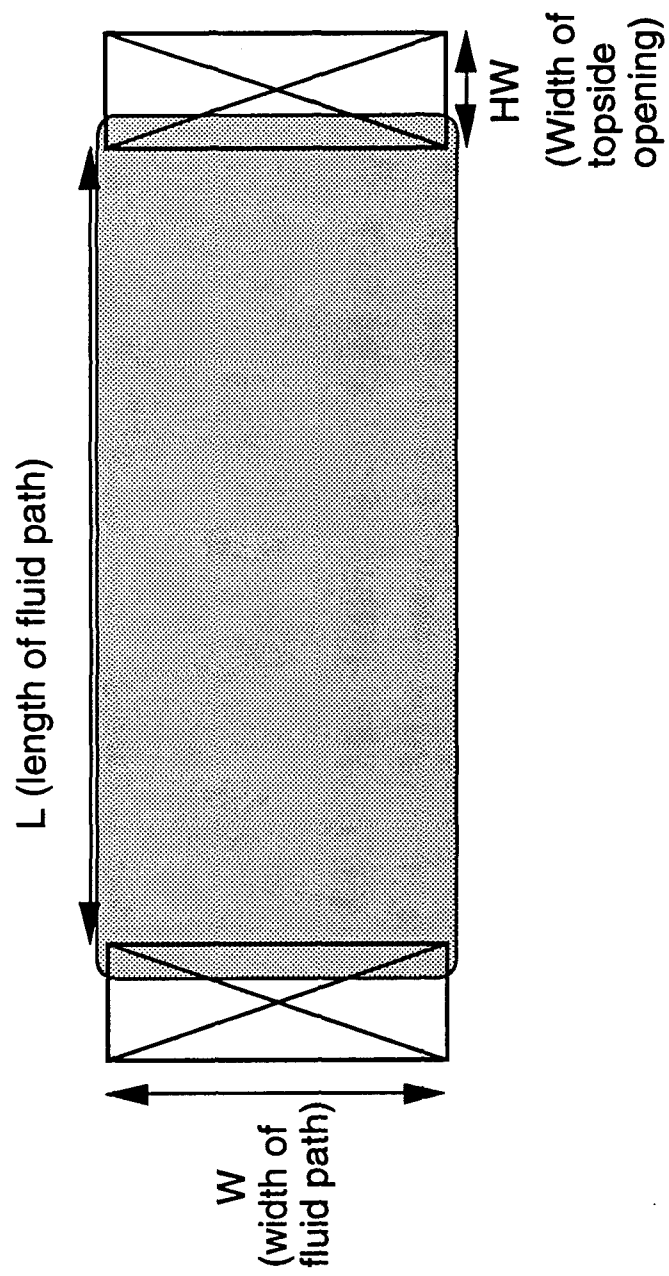


Figure Si-12. Geometry of a Valve

a calibrated capillary tube. This extends the measurement range down to about  $10^{-4}$   $\mu\text{L/s}$ .

Data demonstrating that a valve operates as intended are shown in Figures Si-13 and Si-14, for a valve with  $W=1250\text{ }\mu\text{m}$ ,  $L=1800\text{ }\mu\text{m}$ ,  $HW=250\text{ }\mu\text{m}$ , and  $T=26.5\text{ }\mu\text{m}$ . Fig. Si-13 shows flow as a function of driving pressure, with the closing pressure as a parameter. It indicates that the valve acts as a flow resistor, in which flow is modulated by  $P_{\text{dr}}-P_{\text{cl}}$ , provided that  $P_{\text{dr}}>P_{\text{cl}}$ . When closing pressure is greater than driving pressure, the flow becomes negligible compared to the on-flow. Fig. Si-14 shows the characteristics of the same valve in another way, as a function of closing pressure, with the driving pressure as a parameter.

Two of the geometric parameters listed above were found to not affect the data in a major fashion:  $L$  and  $HW$ . In both cases, the changes in flow characteristics caused by changing that parameter alone were less than the range of data measured with valves with identical geometry.

The two remaining parameters were found to have a major impact on a particular aspect of the flow characteristics. Fig. Si-15 shows the flow as a function of driving pressure, for several valves with different widths of the flow channel and zero closing pressure. It can be seen that the flow increases very rapidly as a function of channel width. For instance, increasing the width from  $750\text{ }\mu\text{m}$  to  $1250\text{ }\mu\text{m}$  increased the flow by a factor of 10. This can be explained by the fact that the flow resistance in a thin channel is proportional to the cube of the channel thickness. This channel thickness in turn depends on how much the input pressure deflects the rubber membrane. This is also a high-order dependence on the width of the membrane.

The other geometric parameter with a major impact on device characteristics is  $T$ , the thickness of the sacrificial photoresist layer. Fig. Si-16 shows the flow at 4 psi driving pressure as a function of closing pressure for valves with different sacrificial layer thicknesses. There is a leakage flow present when the valve is closed, which does not depend strongly on the closing pressure, but depends strongly on  $T$ . When  $T$  is thin enough, the leakage flow becomes so low it is difficult to measure accurately; the leakage flow data points shown in Fig. Si-15 for  $T=2.8\text{ }\mu\text{m}$  correspond to flows below  $2\times 10^{-4}\text{ }\mu\text{L/s}$  which could not be determined precisely.

The data of Fig. Si-16 prove that, with an appropriate choice of  $T$ , valves can be made with an on/off flow ratio of greater than  $10^6$  (limited by the difficulty in measuring very low flows). This means the devices do indeed function as nearly ideal valves for liquid flow, and that they can meet both the on-flow and off-flow requirements listed above.

Valve with  $W=1250\text{ }\mu\text{m}$ ,  $L=1880\text{ }\mu\text{m}$ , and  $T=26.5\text{ }\mu\text{m}$

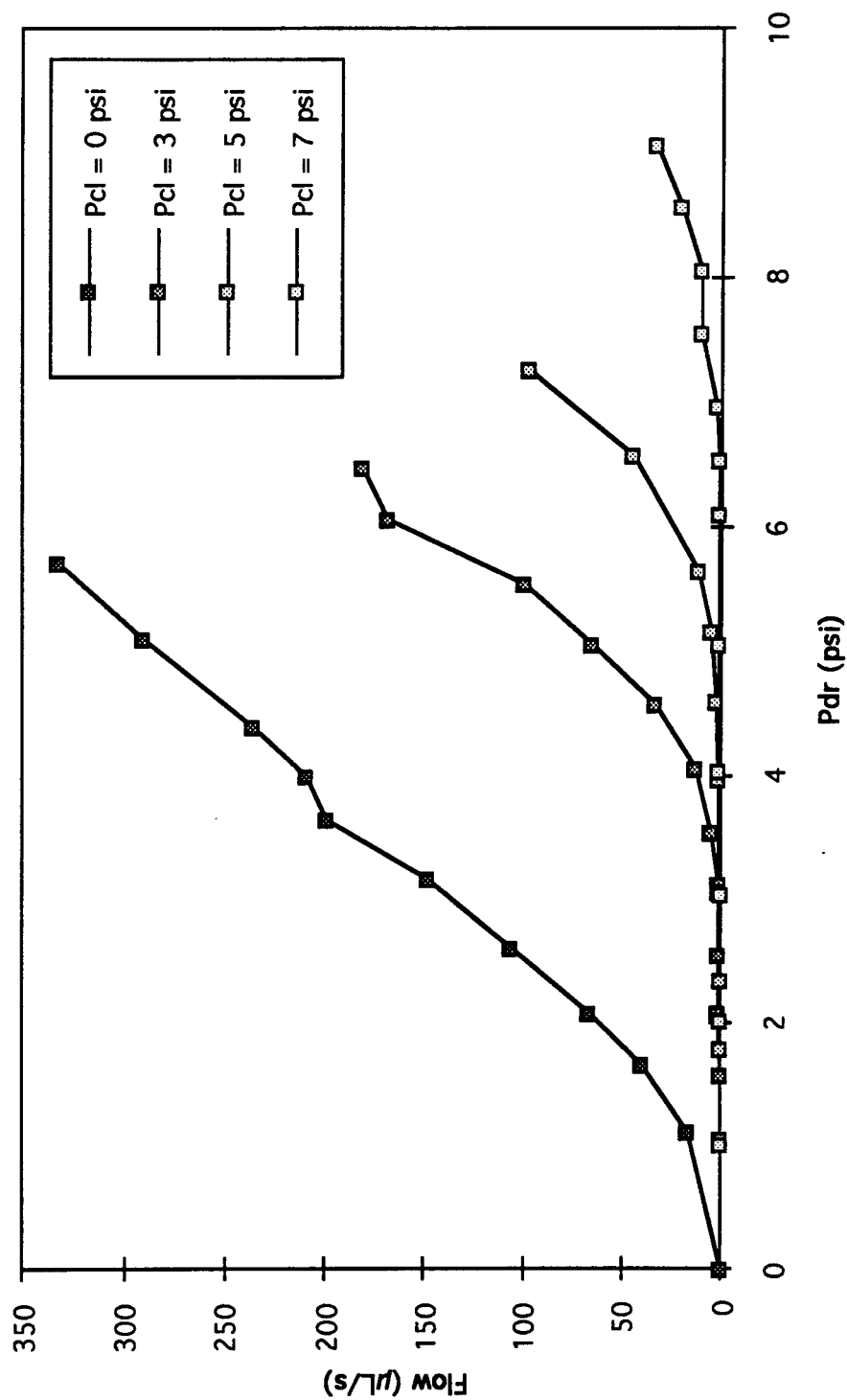


Figure Si-13. Flow vs. Driving Pressure; Closing Pressure as a Parameter

Valve with  $W=1250\text{ }\mu\text{m}$ ,  $L=1880\text{ }\mu\text{m}$ , and  $T=26.5\text{ }\mu\text{m}$

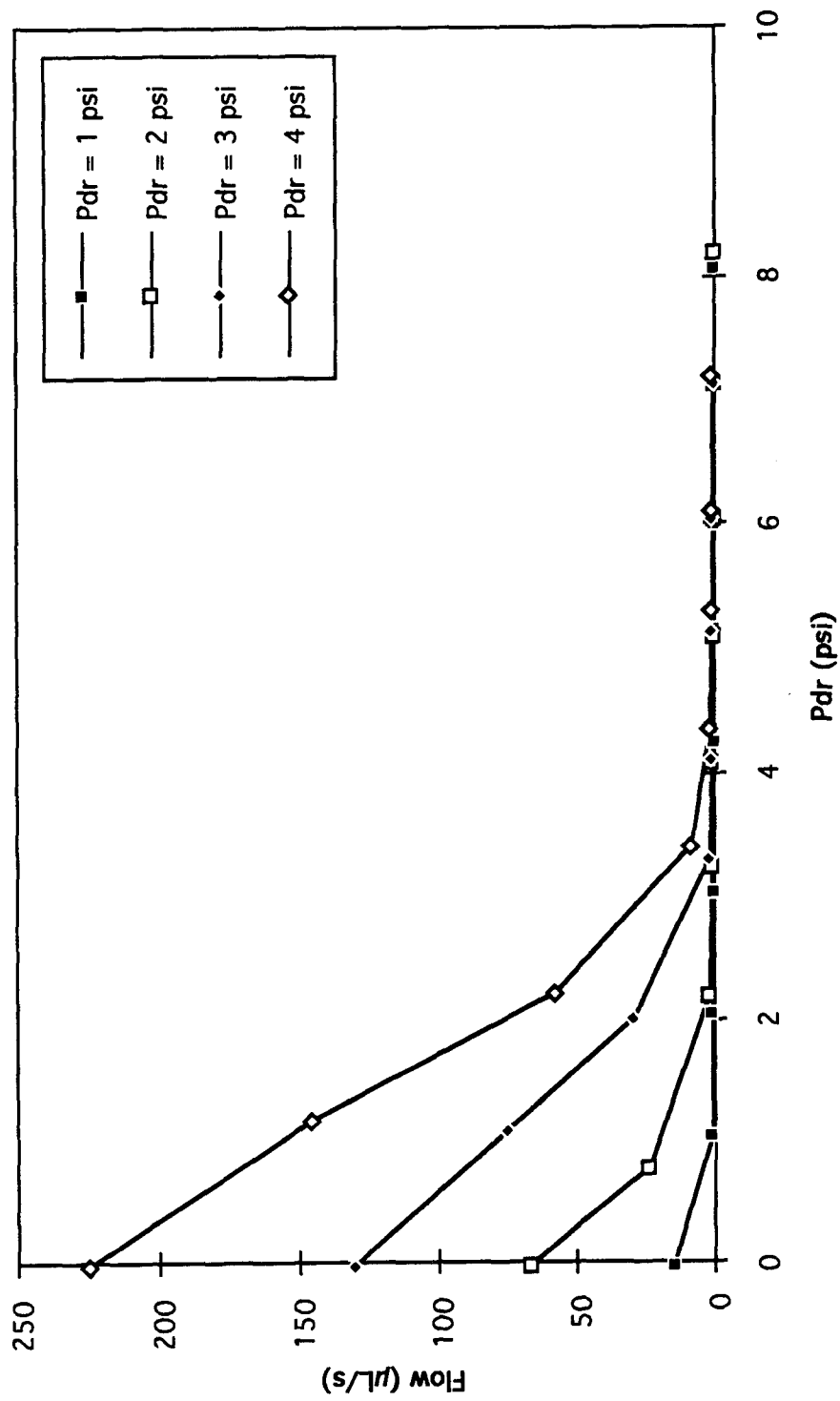


Figure Si-14. Flow vs. Closing Pressure; Driving Pressure as a Parameter

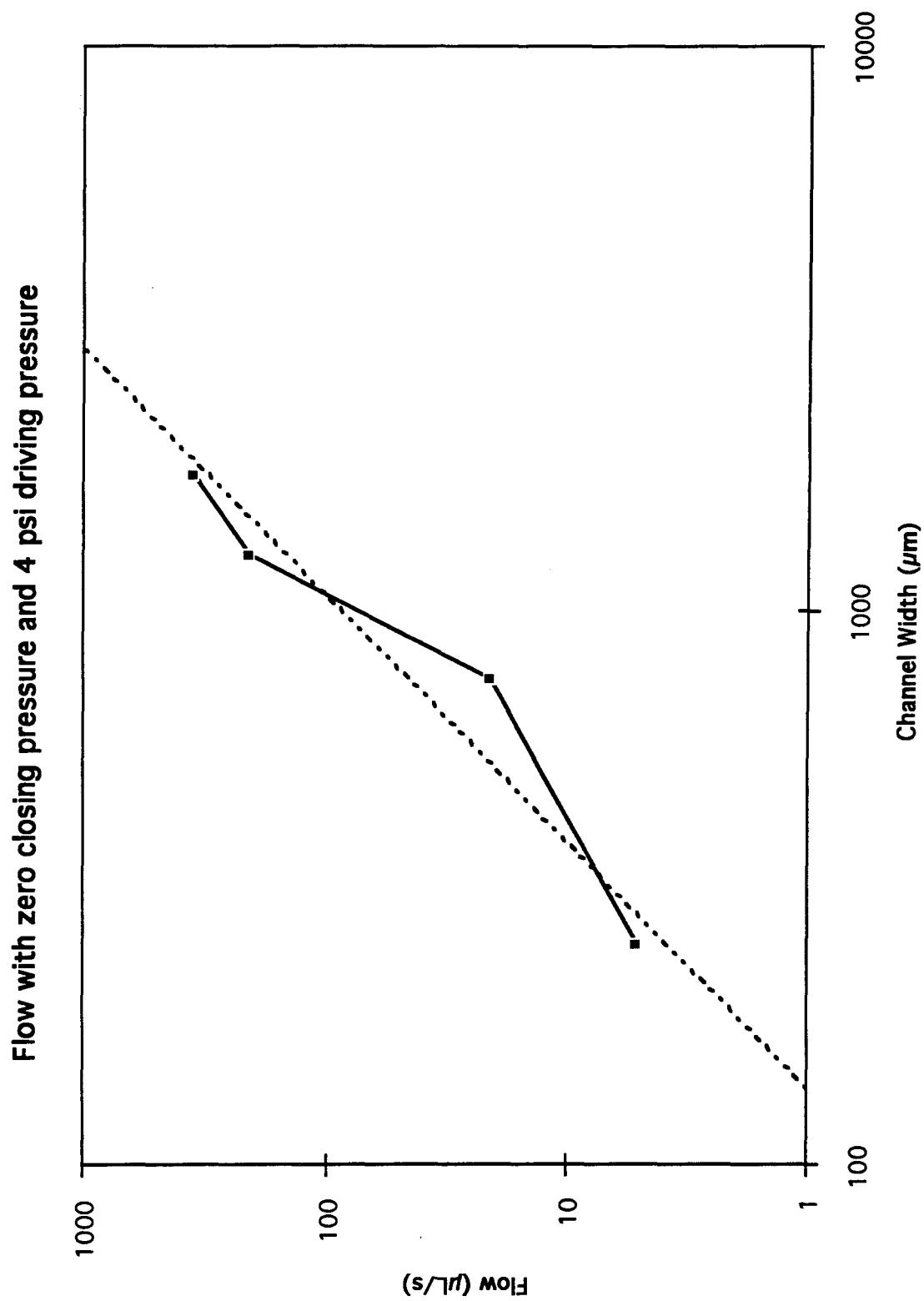


Figure Si-15. Flow vs. Channel Width

Flow with 4 psi driving pressure as a function of channel thickness

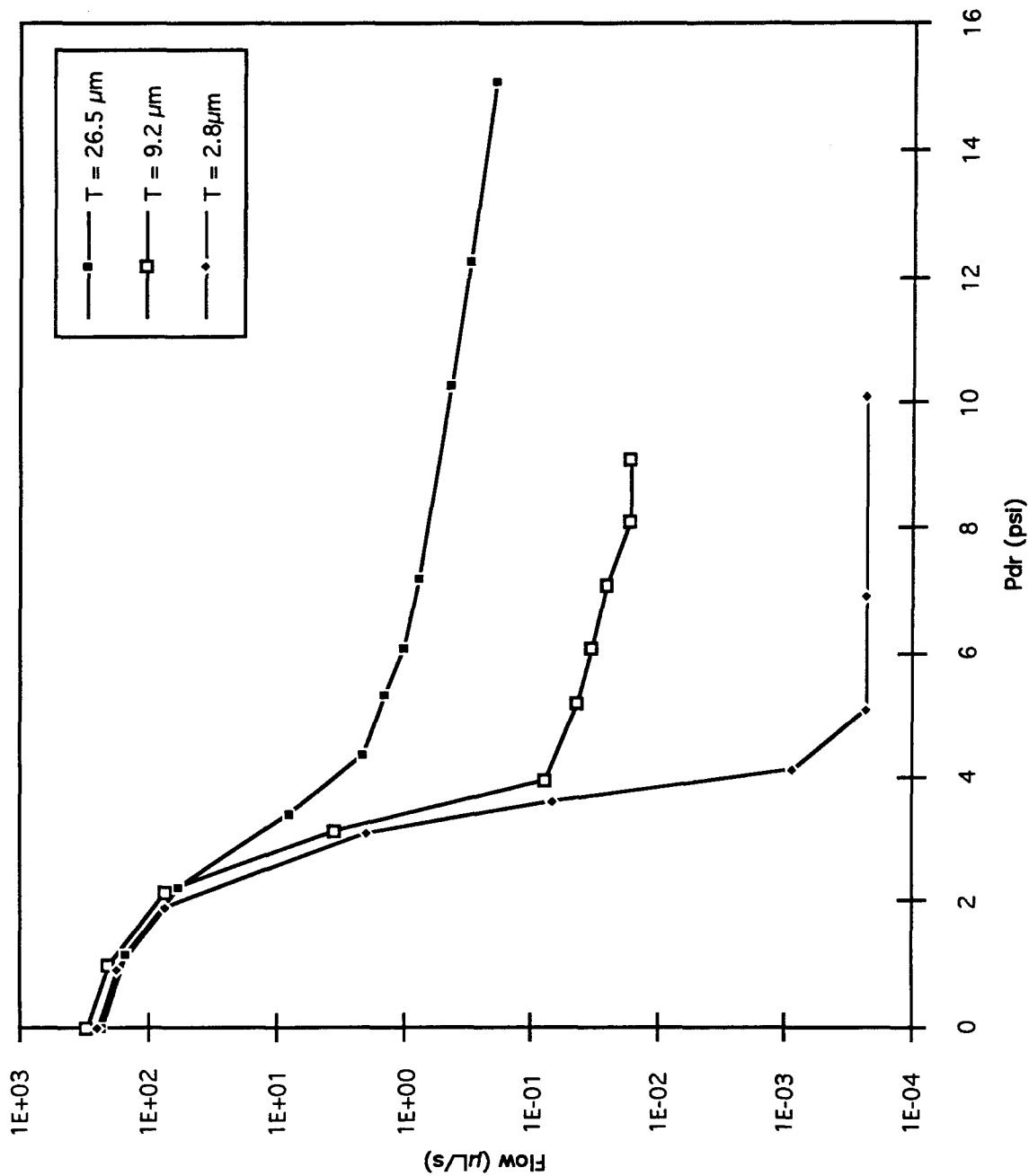


Figure SI-16. Flow vs. Driving Pressure; Sacrificial-Layer Thickness as a Parameter



## 7. Extension to valve arrays

### 7.1 Design and layout

The motivation of this work entails the fabrication of not just individual microvalves, but microvalve arrays. The difference between the two is that an array requires a layer of fluidic interconnects so that multiple valve can be connected together in some pattern. One way to create a layer of fluid interconnections is to etch a channel at the bottom of the valve chip. This channel can be used to connect several openings to different valves. Fig. Si-17 shows a cross-section of two valves connected together in this fashion. The fluid input is common for the two valves, and the output of each is not shown since it is assumed to lie outside of the plane of the drawing.

One simple type of valve array that is required in all microphysiometry applications is the four-way valve. In this arrangement, four inputs or outputs are arranged in a square and are connected by a valve between each adjoining pair (Fig. Si-18). Depending on which set of two opposing valves is opened, either In1 is connected to Out1 and In2 to Out2 (by closing valves B and D); or In1 is connected to Out2 and In2 to Out1 (by closing valves A and C). This provides the ability to essentially switch two flow channels. Typically, Out1 will be a channel of the flow-through microphysiometer chip, and Out2 will be waste.

An actual layout of a four-way valve is shown in Fig. Si-19. This layout consists of a square 4.6 mm on a side, implying that 4 of these squares would fit in 1 cm<sup>2</sup>. This means the valve density is 16 cm<sup>-2</sup>, since each four-way valve uses 4 individual valves. A square layout makes sense, since it conserves the symmetry of the layout as much as possible. But to use in conjunction with a microphysiometer chip, the width of each four-way valve should be as low as possible, so that each channel can have one. That would require 2 mm spacing; or for every other channel 4 mm spacing. It is possible to make the same four-way valve layout narrower and longer. Such an alternative layout is shown in Fig. Si-20.

This Fig. Si-20 also shows that three of the flow connections are intended to be made from the same side as the rubber layer, by making an opening through the rubber. This is intended for compatibility with the flow-through microphysiometer chip (see section 7.4). Fig. Si-21 shows a cross-section of a valve one of whose connections goes through an interconnect and crosses over to the rubber side of the wafer where an opening is made through the rubber.

### 7.2 Fabrication process

Compared to the process flow described above (section 5.3), an extra etch step is added to make the bottom fluid interconnect. This is done at the beginning of the process, before the definition of the holes through the wafer. The process sequence is now expanded to:

1. Oxidation of the silicon wafer, to a thickness of 1  $\mu$ m.
2. Photolithographically define openings in the oxide on the backside (bottom channel mask).

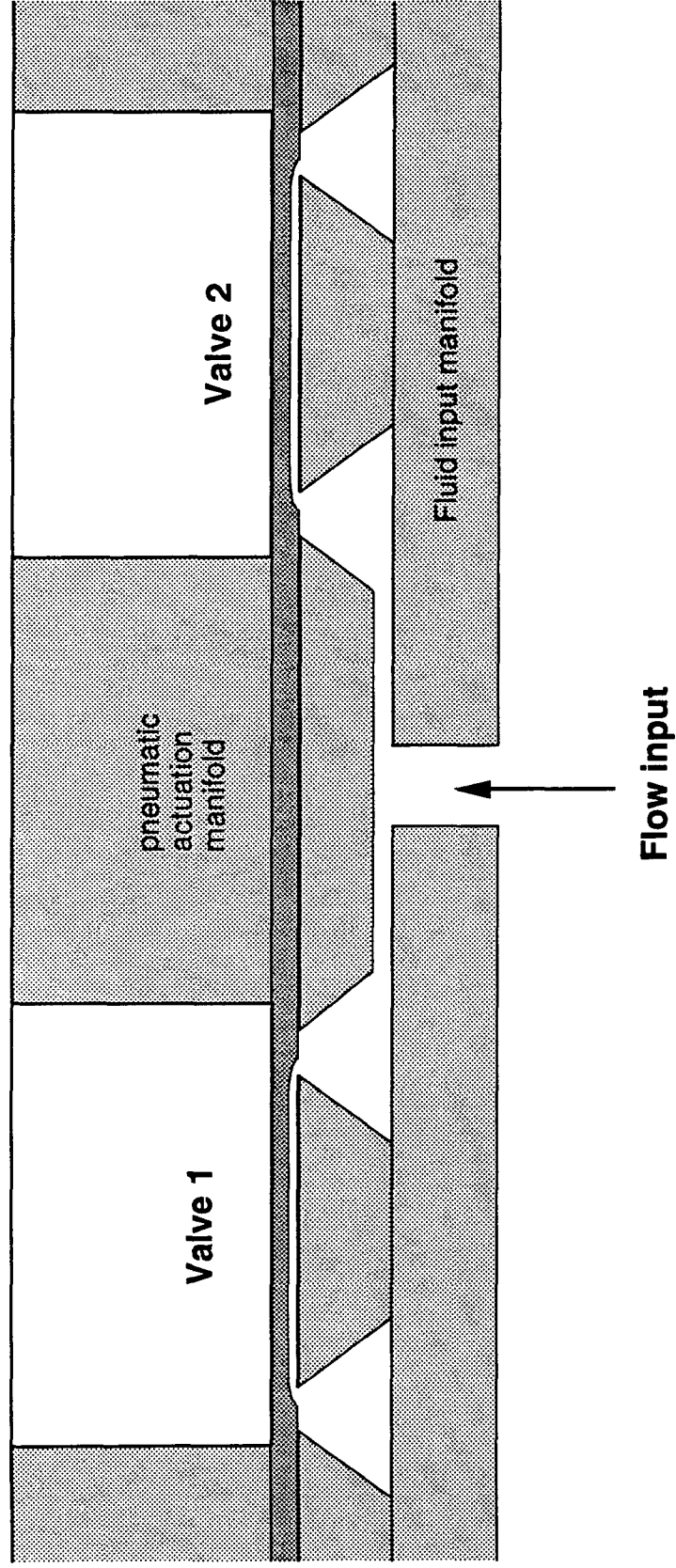
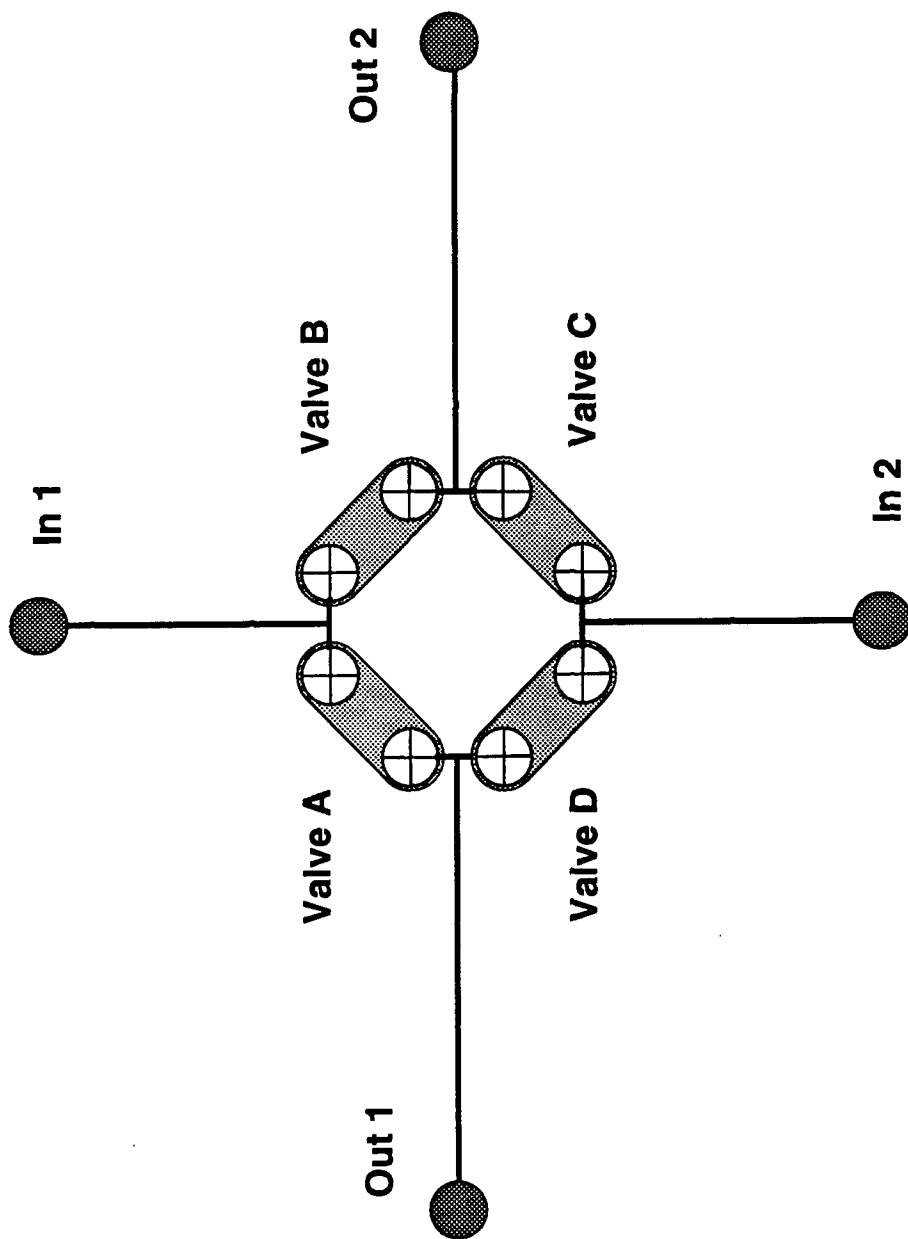
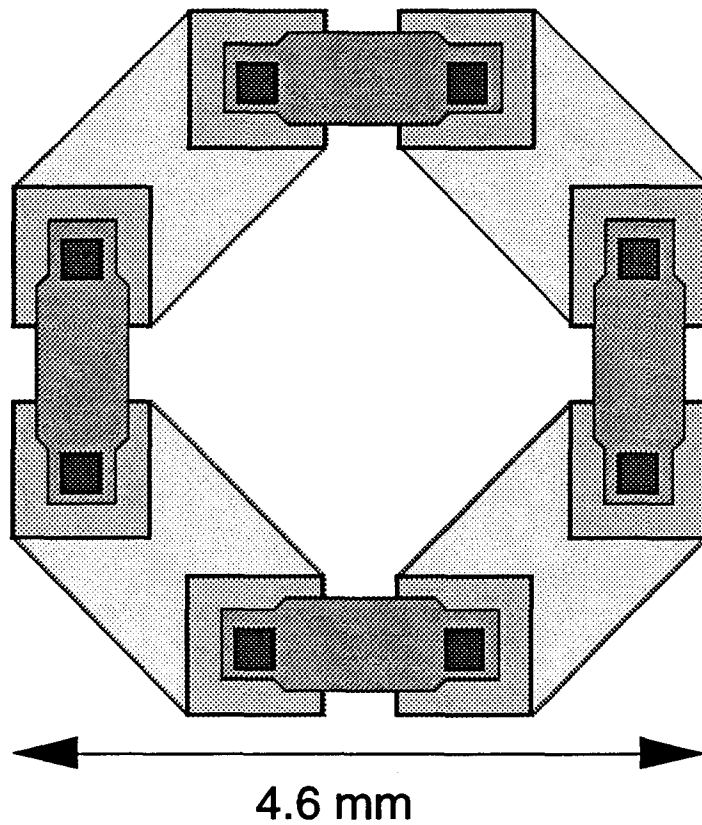


Figure SI-17. Interconnection of two valves

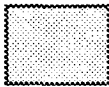
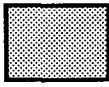
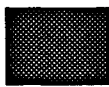
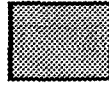


**Figure 18.** A Four-Way Valve

## Square layout of four-way valve

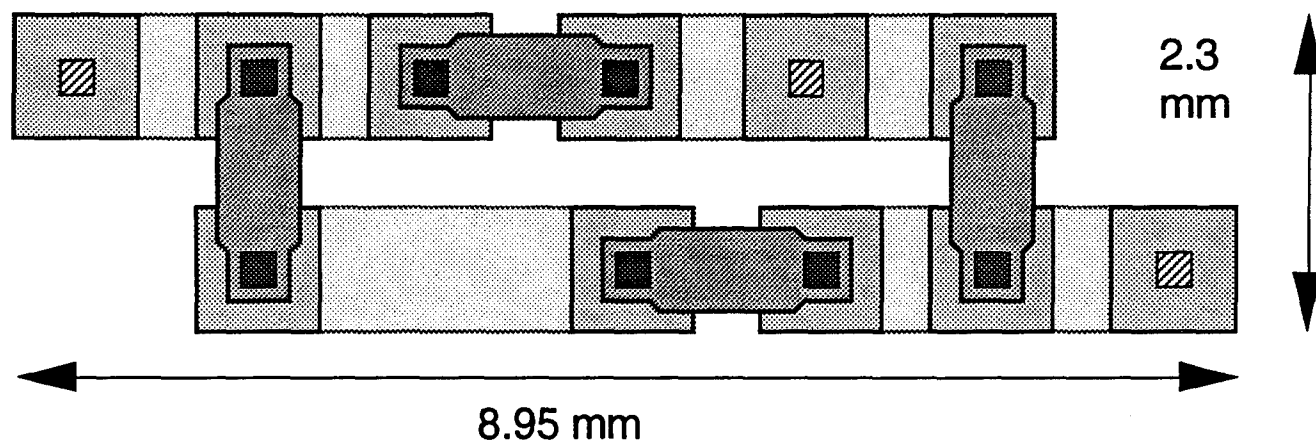


### Key to layers:


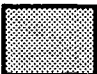



-  Bottom channel
-  Bottom openings (to front)
-  Top openings covered with sac layer, for valve
-  Sacrificial layer for valve formation (photoresist)

**Figure Si-19.** Actual Layout of Four-Way Valve

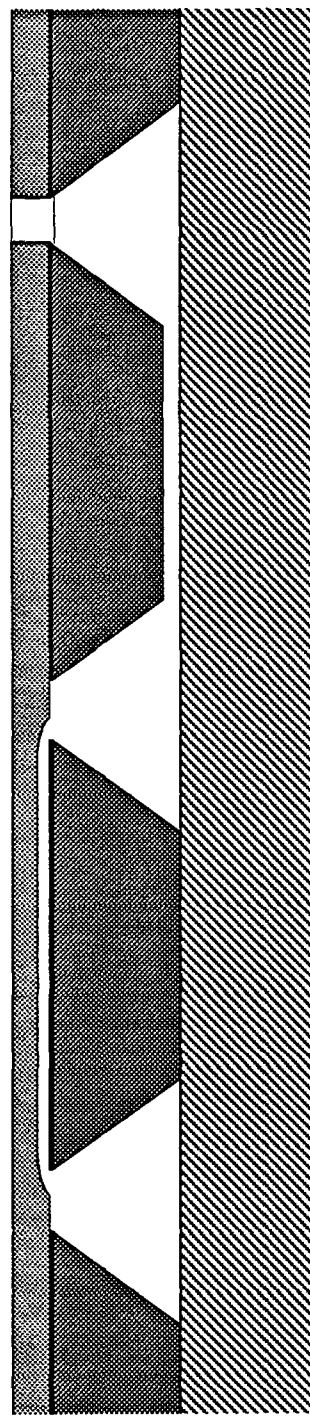
## Rectangular layout of four-way valve



### Key to layers:

-  Bottom channel
-  Bottom openings (to front)
-  Top openings covered with sac layer, for valve
-  Top openings in the rubber, for fluid connection
-  Sacrificial layer for valve formation (photoresist)

**Figure Si-20.** Alternative Layout of Four-Way Valve



Valve

Fluidic interconnect

**Figure SI-21.** Cross Section Through Interconnect in Valve in Figure SI-20

3. Etch the bottom channel with an anisotropic etchant, about 100  $\mu\text{m}$  deep.
4. Remove all the oxide with HF, and reoxidize to 1  $\mu\text{m}$ .
5. Photolithographically define openings in the oxide on the backside (through hole mask).
6. Spin-coat and pattern the sacrificial photoresist on the frontside of the wafer, in alignment with the pattern on the backside.
7. Spin-coat uncured silicone rubber on the frontside, on top of the photoresist.
8. Heat-cure the rubber.
9. Etch holes in the silicon from the bottom in an anisotropic etchant, in the one-sided silicon etch fixture.
10. Etch the oxide windows in buffered HF.
11. Removing the sacrificial photoresist layer in Microposit at about 80 to 100  $^{\circ}\text{C}$ .
12. Wafer dicing.

An optional extra step is the definition of holes through the rubber in defined locations. This can be done at the wafer level with laser drilling, or at the chip level by manually cutting the rubber. Although we have not yet experimented with this process step, it is not anticipated to be a problem.

### 7.3 *Testing of four way valve arrays*

The number of tests that can be done on a four way valve arrays is immense. First, each of the four valves can be tested individually, with the other ones being kept closed. An example of such a measurement is shown in Fig. Si-22, which shows the flow through a single valve of an array as a function of driving pressure, with zero closing pressure. This measurement shows that this valve behaves in the same way as the individual valves.

The next test is the ability of the four way valve array to switch flow from one fluid path to another. We will test not only the ability to do an all-or-nothing, or binary, switch, but also the continuous transition between the two modes. The experimental setup is shown in Fig. Si-23. Two of the four valves are kept closed, while an input pressure of 2 psi is applied to the vertex located between the other two valves. The closing pressure is initially zero for one of the valves, and 5 psi for the other, and the flow through each valve is recorded. Then the closing pressure on the first valve is increased, and that on the second valve is decreased, in such a way that the two pressures always add up to 5 psi. As a result, the flow gradually switches from one valve to the other. The flow data are also shown in Fig. Si-23. Note that there is a region where the flow in both valves is essentially zero. This is due to the fact that the driving pressure is less than half the total closing pressure. If the driving pressure used were higher (4 psi, for instance), there would be region where both valves are open at the same time. This shows that it is possible to control the nature of the switching transition. In most cases, it will be preferable to use a transition such as shown here, where there is never flow in the two valves at once.

It is also noteworthy that the flow in Fig. Si-23 is shown on a logarithmic scale. It can be seen that in both valves, the on/off ratio is in the order of  $10^6$ . This is probably limited by our ability to measure ultra-low flows, rather than by true leakage. But it does show that these devices meet the requirements stated above, in Section 2.

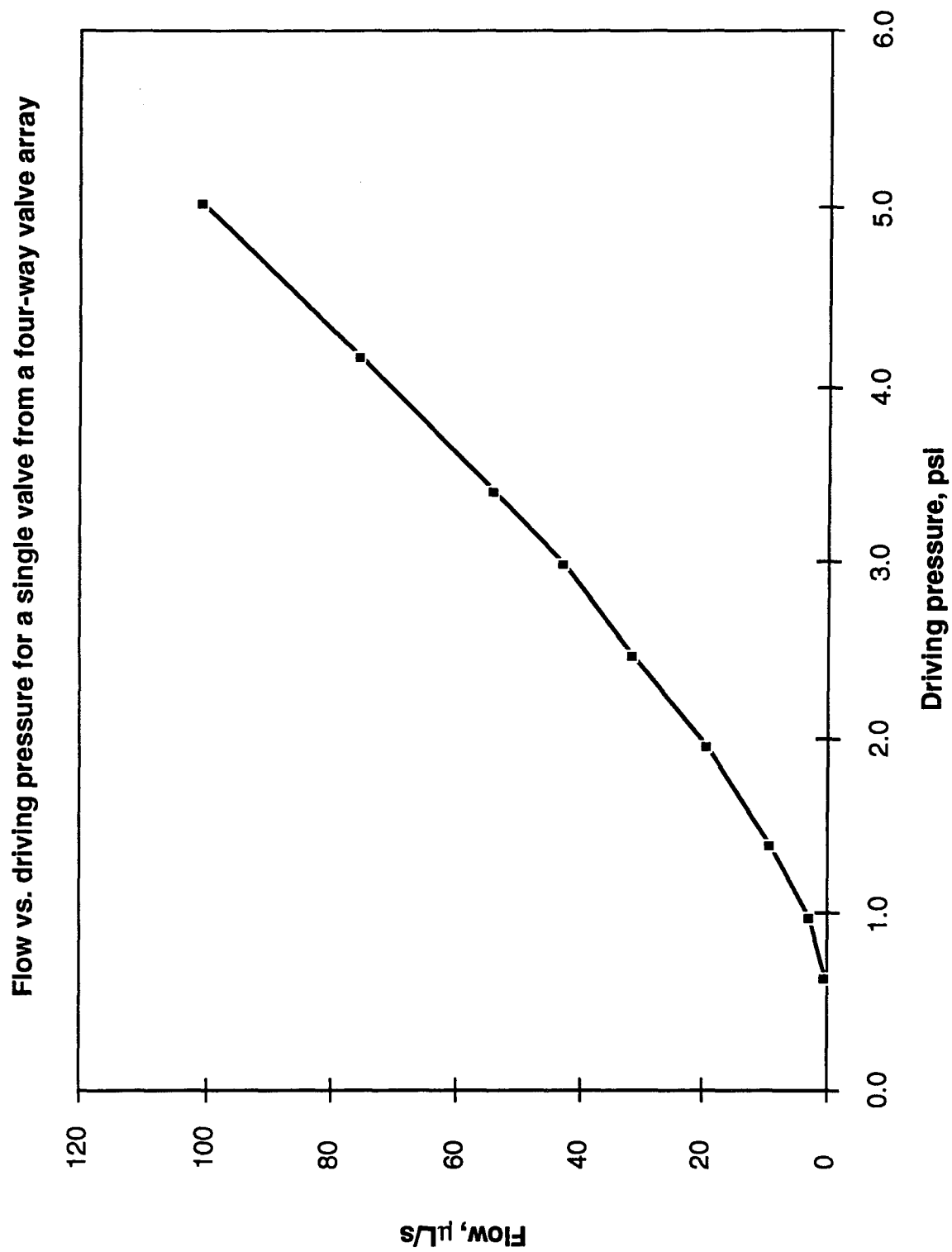


Figure SI-22. Flow vs. Driving Pressure for Four-Valve Array



## Testing of four way valve

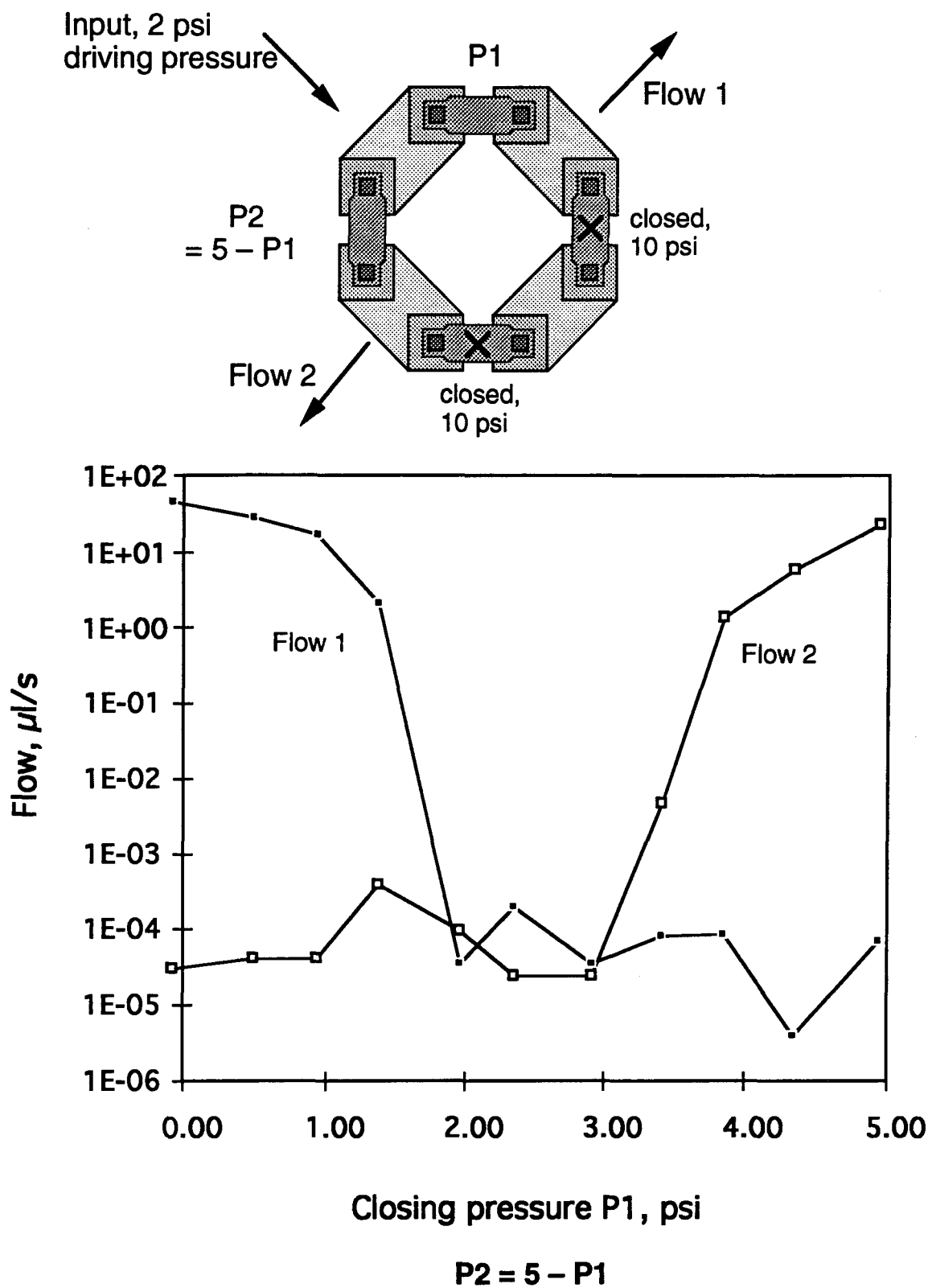


Figure Si-23. Testing of Four-Way Valve

#### 7.4 Future integration with the flow-through chip

In the discussion in Section 1 about valve density requirements, it was established that to minimize the dead volume between valves and the channels in the flow-through chip, it was necessary to directly connect the valve array and the flow-through chip. The best way to do that is to stack the two chips on top of each other, and line up the outputs of the valve chip directly with the flow channel inputs. This immediately implies that one side of the wafer can only contain the fluid outputs to the flow-through chip, and that both the actuation and the inputs to the valve have to be on the other side of the wafer. Since the actuation must be on the rubber side, that means that the valve inputs must also come from the rubber side. This is the basic motivation of the structure shown in Fig. Si-21, with both actuation and one fluid connection on the rubber side of the wafer.

Fig. Si-24 shows a cross-section of a valve chip combined with a flow-through chip. The process needed for the valve chip is the one described in section 7.2, with the addition of the openings through the rubber layer. Fig. Si-25 shows a view of the layout of three of the four-way valve arrays in a chip 1 cm on a side. The spacing between two adjacent four-way valves is 2.8 mm. The total valve density on this chip is  $12 \text{ cm}^{-2}$ .

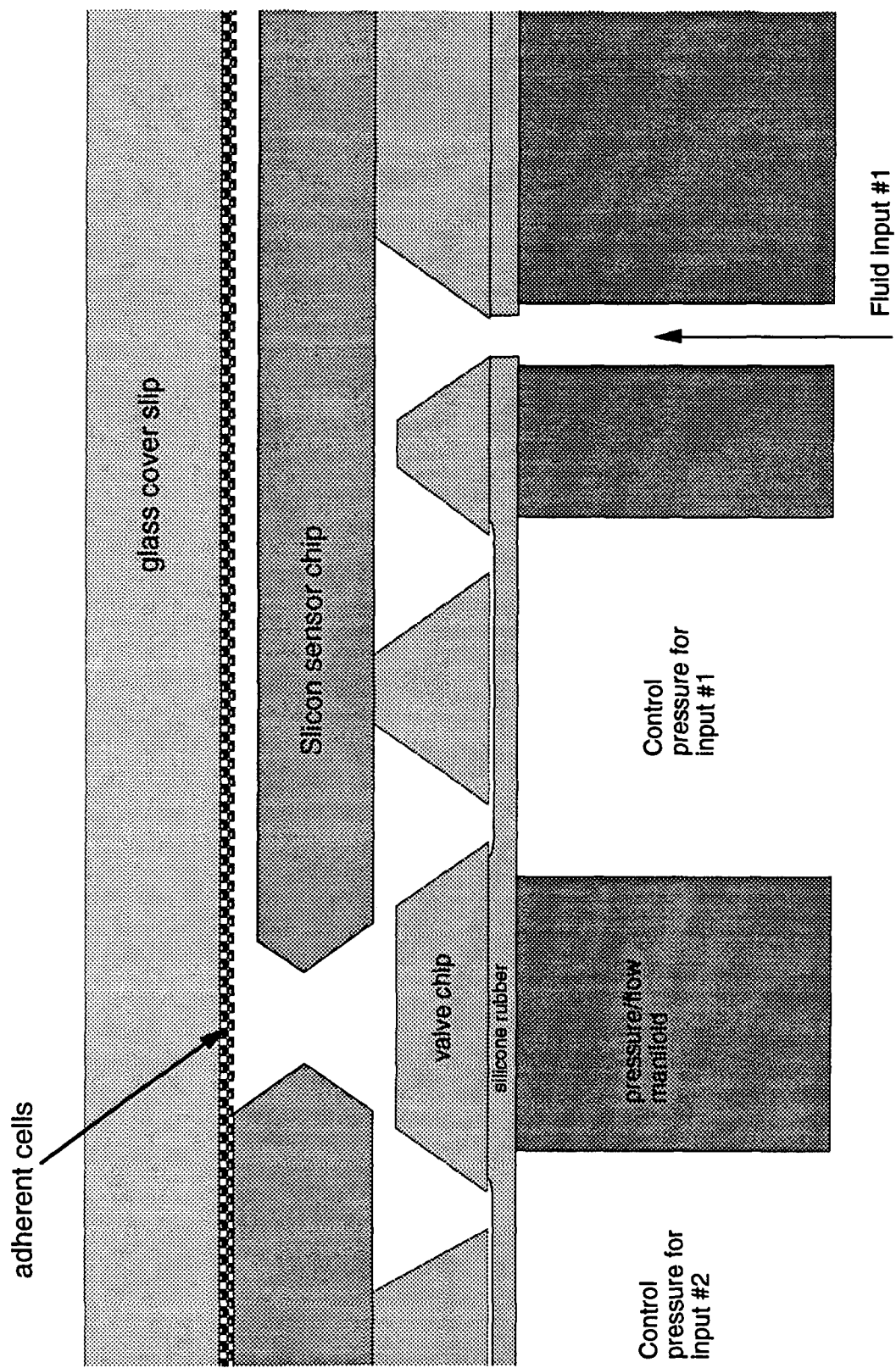
The chip shown in Fig. Si-25 has been fabricated but not yet tested. In terms of the dimensions needed to interface with a flow-through chip, the spacing of 2.8 mm is still larger than the current 2 mm spacing between flow channels. This means that a new design of both the valve array chip and the flow-through chip will be needed to interface with each other. Our results so far demonstrate the feasibility of such an integrated design. That would also make it possible to accomplish more elaborate fluid switching between different flow channels such as contemplated in the proposal.

### 8. Conclusions

We have developed and tested a novel technology of making high-density fluid microvalve arrays, with the goal of demonstrating high performance microfluidics. A set of performance specifications was derived from the application we intend for high performance microfluidics, and the devices we have fabricated were tested to demonstrate that they meet these specifications. In particular, the specifications of density, dimensions, flow rates, and on/off ratios have all been met. More work will be needed to address the issues of materials compatibility and compound carryover. However, since silicone rubber is a material with well-known properties, no major surprises are expected on this topic.








### 9. References for silicon engineering section

- [1] P. Gravesen, J. Branebjerg, and O.S. Jensen, Microfluidics - a review, *J. Micromech. Microeng.*, 3 (1993) 168-182.
- [2] B.H. van der Schoot, A. van den Berg, S. Jeanneret, and N.F. de Rooij, A miniaturized chemical analysis system using two silicon micro pumps, *Transducers 91. San Francisco, 1991*, pp. 789-791.
- [3] S. Shoji, S. Nakagawa, and M. Esashi, Micropump and sample injector for integrated chemical analysis systems, *Sensors and Actuators, A21-A23* (1990) 189-192.



**Figure Si-24.** Cross Section of Four-Way Valve Array Compatible with High-Performance Microphysiometer

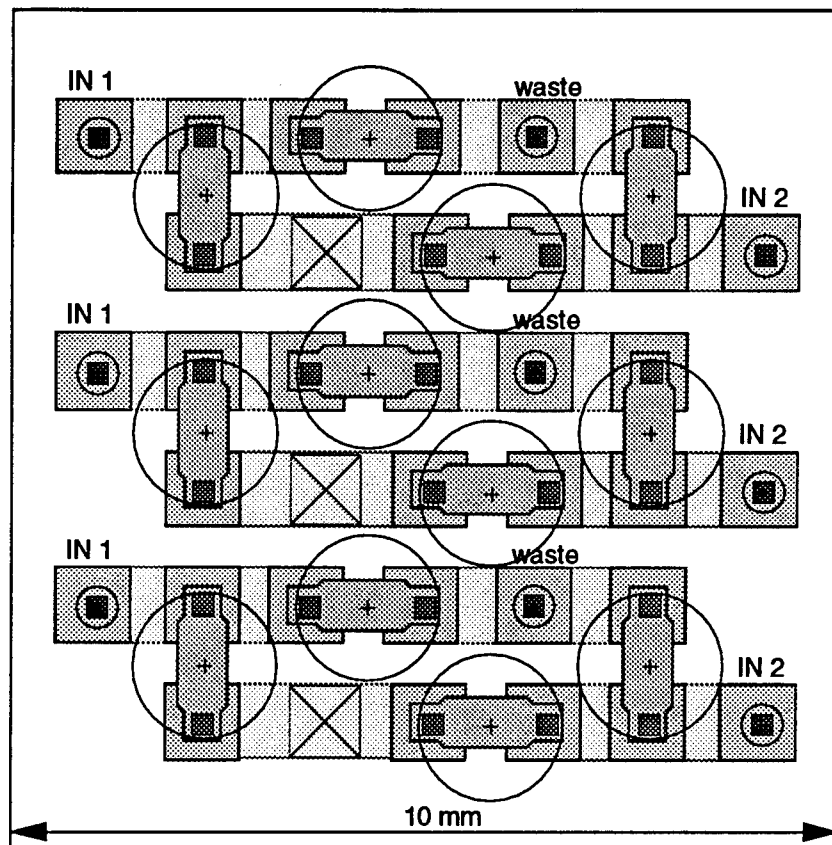
**Key to layers:**

	Bottom channel		Sacrificial layer for valve formation (photoresist)
	Bottom openings (to front)		Manifold opening on top side Small openings: fluid in/out Large openings: actuation pressure
	Top openings covered with sac layer, for valve		Connection to HTμø chip on bottom side
	Top openings coinciding with opening in rubber		

Top side: silicone rubber side, where actuation occurs, fluid inputs, waste output

Bottom side: silicon side, where the HTμø chip is.

Scale 14X



**Characteristics of this type:**

1. 2.3 mm wide and 8.925 mm long
2. 2.8 mm pitch (spatial periodicity); 8 valves are 20.45 mm wide on HTμø side
3. This drawing shows 3 four-way valves in a 1 cm square
4. Top holes are 0.25 mm square
5. Channels are 0.6 mm wide

**Figure Si-25.**

Design for a Valve Manifold Compatible with High-Performance Microphysiometry

- [4] M.J. Zdeblick and J.B. Angell, A microminiature electric-to-fluidic valve, *Proceedings of the 4th International Conference on Solid-State Sensors and Actuators. Tokyo, 1987*, pp. 827-829.
- [5] Z.D. Zdeblick, R. Anderson, J. Jankowski, B. Kline-Schoder, L. Christel, R. Miles, and W. Weber, Thermopneumatically actuated microvalves and integrated electro-fluidic circuits, *Technical Digest IEEE Solid State Sensor and Actuator Workshop. Hilton Head, S.C., 1994*, pp. 251-255.
- [6] B. Bustgens, W. Bacher, W. Menz, and W.K. Schomburg, Micropump manufactured by thermoplastic molding, *IEEE Micro Electro Mechanical Systems Conference. Oiso, Japan, 1994*, pp.
- [7] S. Shoji, B. Van der Schoot, N. de Rooij, and M. Esashi, Smallest dead volume microvalves for integrated chemical analysis systems, *Transducers '91. San Francisco, 1991*, pp. 1052-1055.
- [8] C. Vieider, O. Ohman, and H. Elderstig, A pneumatically actuated micro valve with a silicone rubber membrane for integration with fluid-handling systems, *Transducers '95. Stockholm, 1995*, pp. 284-286.
- [9] M.G. Allen, M. Mehregany, R.T. Howe, and S.D. Senturia, Microfabricated structures for the in situ measurements of thin films using load deflection of composite rectangular membranes, *J. Appl. Phys.*, 51 (1987) 241-243.
- [10] F. Maseeh, M.A. Schmidt, M.G. Allen, and S.D. Senturia, Calibrated measurements of elastic limit, modulus, and the residual stress of thin films using micromachined structures, *IEEE Solid State Sensor and Actuator Workshop. Hilton Head, S.C., 1988*, pp. 84-87.

## B. SYSTEM ENGINEERING

- **Demonstrate two-dimensional microphysiometry.**

It is of fundamental importance to analyze the factors which limit the signal to noise ratio (S/N) in a LAPS pH sensor in order to understand and predict the performance of a two dimensional (2-D) device. The first step in our analysis was to develop an analytical model for the S/N of the silicon sensor (chip) employed in the Cytosensor Microphysiometer marketed by Molecular Devices Corp. The model is based on the pertinent physical properties of the Cytosensor chip, i.e., the active area, field insulator, and depletion layer dimensions and capacitances combined with a noise model of the current to voltage (I-V) converter circuit shown in Figure Sys-1 used to convert the current generated by photonic excitation of a LAPS device into an electrical state variable representative of pH (voltage).

The S/N model for Cytosensor shown in Figure Sys-2 is formatted in a self-documenting spreadsheet. Inputs to the model are listed in the far left hand column. Variable names are given in the second column and the outputs and their associated units appear in the third and forth columns, respectively. Since the formulas used to calculate the outputs are hidden within the output cells, the actual formulas used are reproduced in the sixth column for reference. The LAPS capacitance and photocurrent at the inflection point of the photocurrent versus DC bias voltage curve or "S" curve (see Figure Sys-3) are experimentally determined inputs to the model. The value of the DC bias voltage at the photocurrent inflection point is referred to as  $V_{pip}$  and, at this value, the magnitude of the photocurrent is reduced to about one half of its maximum value.

The value of 1.63 nF used for the LAPS shunt capacitance in Figure Sys-2 was calculated using a highly detailed physical model which is believed to be in excellent agreement with actual devices, given the approximately  $\pm 20\%$  variations in device processing which are normally encountered and the corresponding effects on the capacitance. The value of 0.2  $\mu A$  used for the rms LAPS current is typical of what is measured in production Cytosensor instruments. As can be seen in Figure Sys-2, the predicted S/N for Cytosensor is about 35,000 to 1.

The S/N model developed for the 1-D Cytosensor case was then extended to model the S/N of the 8 and 32 sensor chips (eight fluid channels with 1 or 4 sensors in each channel, respectively). The physical layout of the Cytosensor chip consists of a 1.73 mm diameter sensor surrounded by a insulator area of approximately 7.7 mm in diameter. The layouts of the 8 and 32 sensor chips are shown in Figure Sys-4.

The 8 sensor chip was used as a test case to quantifiably verify the S/N model. When no light excitation is present, the S/N model predicts the rms noise present at the output of the I-V converter circuit. The value predicted by the S/N model, 13.7  $\mu V$ , was found to agree quite well with the value of 14  $\mu V$  measured with a spectrum analyzer as can be seen in Figures Sys-5 and Sys-6. The eight sensor chip was used rather than the Cytosensor chip because the 32 sensor chip was not available at that point in the research program and the Cytosensor chip and its associated electronics were

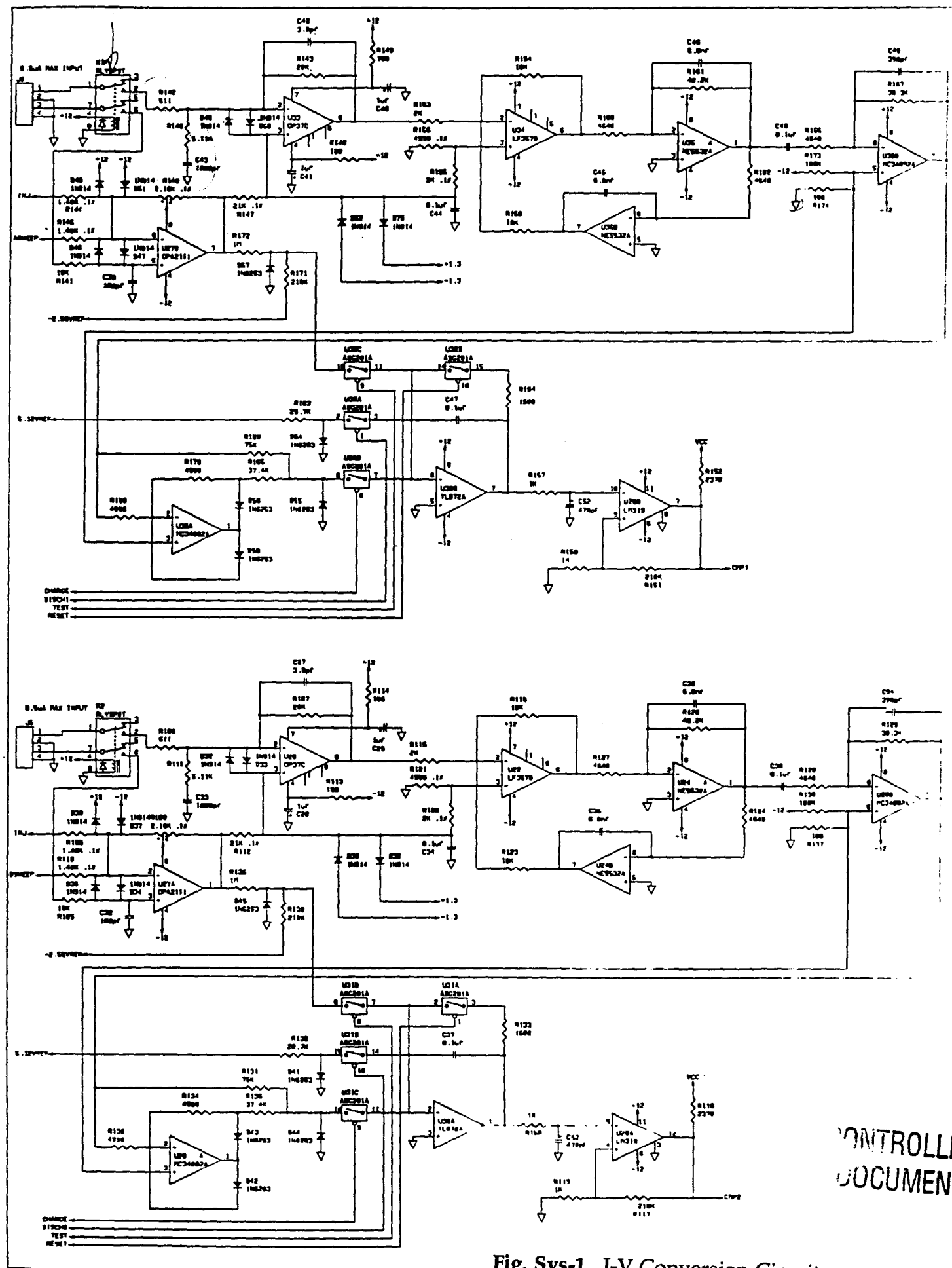


Fig. Sys-1. I-V Conversion Circuit

CONTROLLE  
DOCUMENT

# Signal to Noise Model for Cytosensor

Inputs	Name	Outputs	Unit	Comment	Formula
Physical Constants:	1.38E-23 k		J°K	Boltzman's constl.	Assume MJC-90 electronics
	3.00E+02 T		°K	Temperature	40 samples per S-curve
	1.60E-19 q		Coulomb	electric charge	1 S-curve per second
LAPS parameters:	1.63E-09 Cs		Farads	LAPS shunt capacitance	
	1.00E+09 Rs		Ohms	LAPS shunt resistance	
Component Values:	1.70E-11 Cf		Farads	Feedback capacitance	
	2.00E+04 Rf		Ohms	Feedback resistance	
	5.11E+02 Rsl		Ohms	I-V converter series resistance	
System parameters:	2.00E-07 iLaps		µAmps	LAPS photo current	
	5.00E+03 f		Hz	LED operating frequency	
	1.82E-02 Ts		sec	Sampling interval	
Op-amp parameters:	4.00E-13 ia		arms/Hz^1.5	amp current noise per sqt Hz	
	3.00E-09 ea		vrms/ Hz^1.5	amp voltage noise per sqt Hz	
Intermediate results:	is	1.78E-24	arms^2	Shot noise squared	$is = 2 \cdot q \cdot iLaps \cdot BW$
	iRs1	6.10E-25	arms^2	LAPS shot noise voltage squared	$iRs1 = 4 \cdot K \cdot T \cdot Rs1 \cdot BW / ((Rs1)^2 + (.159/(f \cdot Cs))^2 \cdot .5)^2$
Noise components:	eno	1.01E-15	vrms^2	Amp voltage noise squared	$eno = (ea \cdot (BW)^{0.5} \cdot (1 + Cs/Cf \cdot (1 + (0.159/(f \cdot Rs \cdot Cs))^2)^{0.5} / (1 + (0.159/(f \cdot Cf))^2)^{0.5}))^2$
	enRf	9.10E-15	vrms^2	Resistor thermal noise squared	$enRf = 4 \cdot K \cdot T \cdot BW \cdot Rf$
	iaRf	1.76E-15	vrms^2	Amp current noise squared	$iaRf = (ia \cdot (BW)^{0.5} \cdot Rf / (1 + (6.28 \cdot f \cdot Rf \cdot Cf)^2)^{0.5})^2$
	isRf	7.03E-16	vrms^2	Shot noise squared	$isRf = is \cdot (Rf / (1 + (6.28 \cdot f \cdot Rf \cdot Cf)^2)^{0.5})^2$
	iRs1Rf	2.44E-16	vrms^2	LAPS shunt R noise squared	$iRs1Rf = iRs1 \cdot (Rf / (1 + (6.28 \cdot f \cdot Rf \cdot Cf)^2)^{0.5})^2$
Noise calculations:	Noise	1.13E-07	Vrms	Total noise at output	$Noise = (eno + enRf + iaRf + iRs1Rf + isRf)^{0.5}$
SNR calculations:	SNR <sub>p</sub>	1.51E+05	none	Photon limited noise SNR	$SNR_p = (Ts \cdot iLaps / q)^{0.5}$
	SNR <sub>a</sub>	3.53E+04	none	Actual SNR from OP-amp output	$SNR_a = iLaps \cdot (Rf / (1 + (6.28 \cdot f \cdot Rf \cdot Cf)^2)^{0.5}) / Noise$

Fig. Sys-2



A ☐ B ☐ C ☒ D ☐

## Overnight Cleanup Single Sweep 1

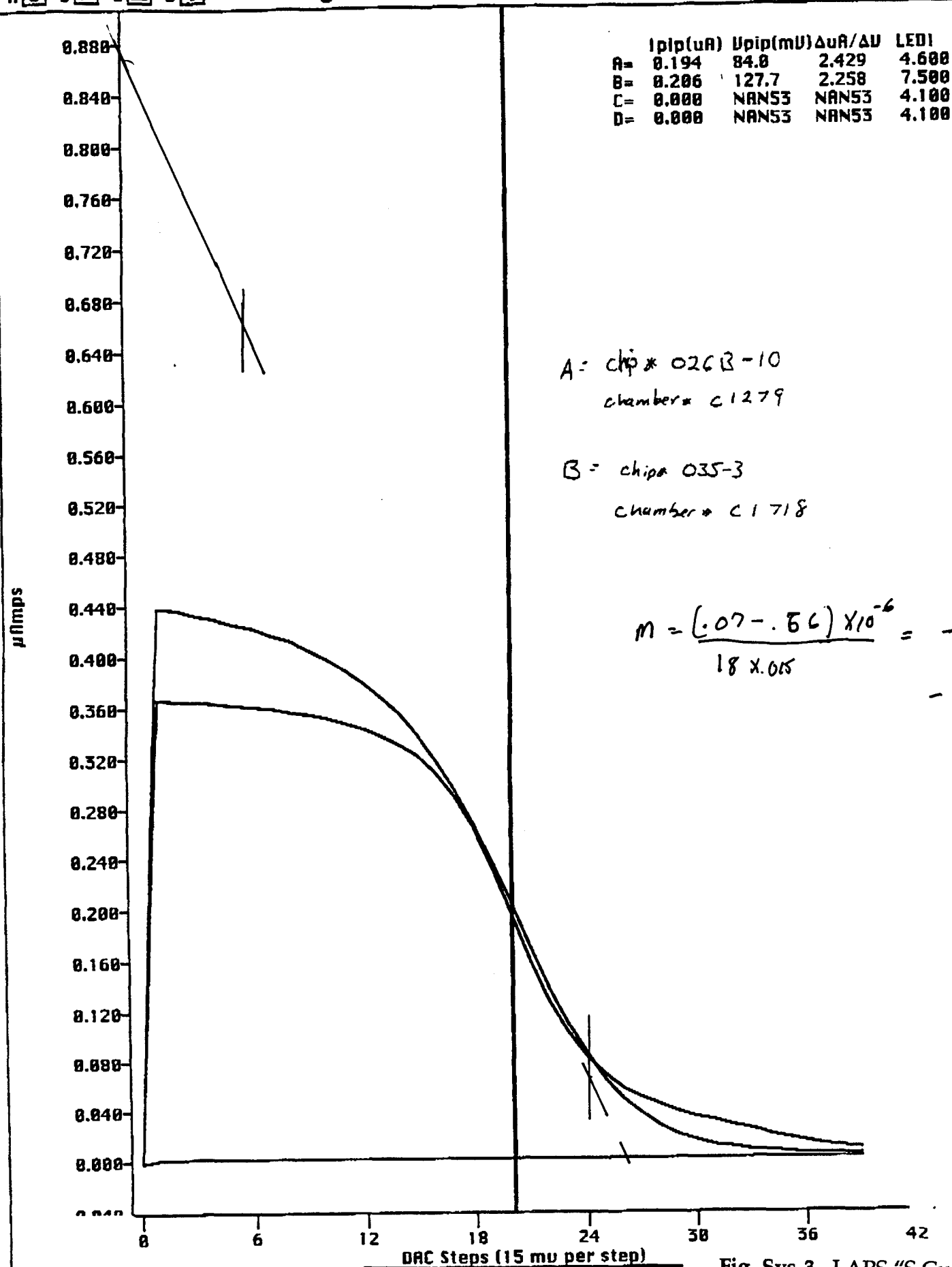
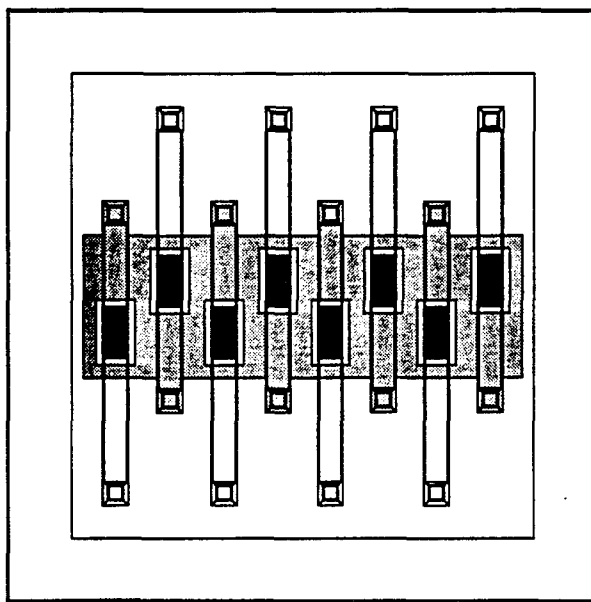
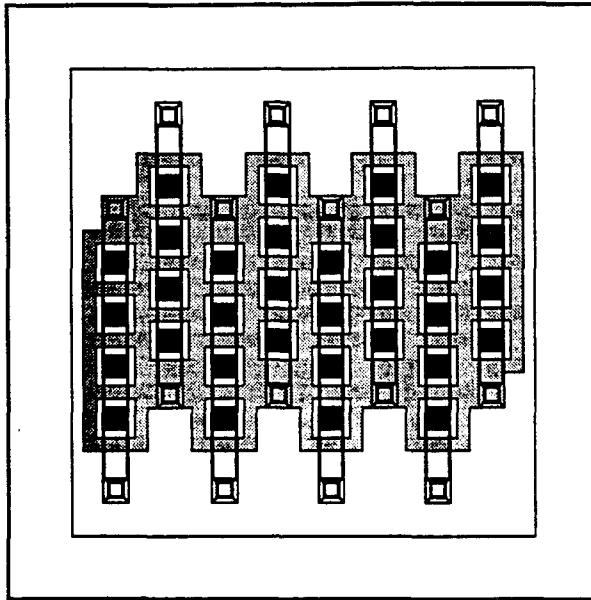


Fig. Sys-3. LAPS "S Curve"



8 x 1 Channels



8 x 4 Channels

Fig. Sys-4. Layout of Sensor Chips

# Noise Model Calculation for 8 Sensor, 8 Fluid Channel Chip

Inputs	Name	Outputs	Unit	Comment	Formula
Physical Constants:	1.38E-23 k		J°K	Boltzman's const.	Assume MDC-90 electronics
	3.00E+02 T		°K	Temperature	40 samples per S-curve
					8 S-curves per second
LAPS parameters:					
	1.25E-08 Cs		Farads	LAPS shunt capacitance	
	1.00E+09 Rs		Ohms	LAPS shunt resistance	
Component Values:					
	3.50E-12 Cf		Farads	Feedback capacitance	
	2.00E+04 Rf		Ohms	Feedback resistance	
	5.11E+02 Rs1			I-V converter series resistance	
System parameters:					
	5.00E+03 f		Hz	LED operating frequency	
	1.82E-02 Ts		sec	Sampling interval	
	BW	27	Hz	Measurement bandwidth	BW = 1/(2*Ts)
	342 Gf			measured gain of test fixture	
Op-amp parameters:					
	4.00E-13 ia		arms/root Hz	OP-37 (MDC-90 electronics) amp current noise per sqt Hz	
	3.00E-09 ea		vrms/root Hz	amp voltage noise per sqt Hz	
Intermediate results:					
	iRs1	3.44E-23	arms^2	LAPS Rs noise current squared	$iRs1 = 4 * K * T * Rs1 * BW / (((Rs1)^2 + (.159/(f * Cs))^2)^{.5})^2$
Noise components:					
	eno	1.93E-14	vrms^2	Amp voltage noise squared	$eno = (ea * (BW)^{.5} * (1 + Cs * Rf * f / .159))^{.2}$
	enRf	9.10E-15	vrms^2	Resistor thermal noise squared	$enRf = 4 * K * T * BW * Rf$
	laRf	1.76E-15	vrms^2	Amp current noise squared	$laRf = (ia * (BW)^{.5} * Rf / (1 + (6.28 * f * Rf * Cf)^2)^{.5})^2$
	iRs1Rf	1.37E-14	vrms^2	LAPS shunt R noise squared	$iRs1Rf = iRs1 * (Rf / (1 + (6.28 * f * Rf * Cf)^2)^{.5})^2$
Noise calculations:					
	Noise	2.10E-07	Vrms	Total noise at output	$Noise = (eno + enRf + laRf + iRs1Rf)^{.5}$
		4.00E-08	Vrms/(Hz)^{.5}	Output noise per root Hz	
		1.37E-05	Vrms/(Hz)^{.5}	noise to HP spectrum analyzer	output to analyzer = $Gf * F37 / (F25)^{.5}$

Fig. Sys-5

RANGE: -51 dBV STATUS: PAUSED  
EXP: 512 OVLD

A: MAG

-51  
dBV

X: 5000 Hz  
Y: -77.03 dBV

$14 \mu V/\sqrt{Hz}$

15  
dB  
/DIV

-171

START: 0 Hz  
X: 5000 Hz

BW: 95.485 Hz  
Y: -77.03 dBV

STOP: 10 000 Hz

Fig. Sys-6. S/N Data for 8 Channel Chip

packaged within a commercial product such that the output from the I-V converter was very difficult to access physically when the instrument was operating. Since the prediction of the S/N model was confirmed for the 8 channel chip, it was assumed that the model would also be valid for the Cytosensor and the 32 sensor chip since the fundamental physics and technology of all three devices are very similar. The noise model has been applied to the 32 channel chip and the results are shown in Figure Sys-7.

From Figures Sys-2, Sys-5, and Sys-7, it can be seen that the noise at the output of the I-V converter increases from about  $0.1 \mu\text{V}$  for the Cytosensor chip to almost  $2 \mu\text{V}$  for the 32 sensor chip. This is due to two factors, the increased input capacitance associated with 31 additional sensors and the decreased signal integration time allowed in order to update the pH reading from each sensor once every second. In addition, since the sensor area of the 32 sensor chip is over a factor of two less than the sensor area of the Cytosensor chip, one expects that the S/N ratio will decrease by a factor of about 40 when both of the above effects are accounted for. Since a primary goal of the program was to maintain the pH sensitivity (and the associated acidification rate sensitivity) of Cytosensor, a study of alternate detection schemes was undertaken to determine whether or not a superior method could be found.

Previous work had shown that illumination from the top side of the silicon wafer rather than the bottom produced a large pulse of photocurrent, and thus it was hypothesized that the S/N ratio might be improved by top side illumination. Subsequent measurements showed, however, that the magnitude of the photocurrent at the fundamental excitation frequency increased only modestly above what can be collected using back-side illumination (by roughly a factor of 2.5 or to about  $0.5 \mu\text{A}$ ). This is because the highly peaked waveforms obtained with top-side illumination contain the majority of their energy in high frequency harmonics. For the case of the 8 and 32 sensor chips, top-side illumination has the added benefit of providing more room on the bottom side of the chip for the fluidic connections required to support the 8 fluid channels.

In addition to the sequential time domain modulation (STDM) detection scheme described above, which uses a lock-in amplifier synchronized to the LED excitation frequency (typically 5 kHz), two alternative detection schemes were also analyzed and compared. The first alternative detection scheme investigated was frequency domain modulation (FDM) in which all sensors are simultaneously excited, but each with a separate LED frequency. A computer with a DSP engine must digitize in real time and analyze the composite photocurrent signal by deconvolving the individual frequency components and thus recovering the 32 separate sensor signals. In the case of FDM, the integration time for all sensors remains the same as for Cytosensor (18.2 ms). The integration time of 18.2 ms was used in Cytosensor because it is roughly half way between one line cycle at 50 and 60 Hz and will thus provide a fair degree of line noise immunity whether or not the product is used in the United States or in Europe. The FDM detection scheme under consideration here would employ the same (or very similar) I-V converter circuit shown in Figure Sys-1 and thus the S/N model of Figure Sys-2 applies with only one minor modification. This modification is that the integration time is reduced by roughly a factor of two due to the fact that the digitized data must be multiplied by a windowing function prior to further digital processing.

# Noise Model Calculation for 32 Sensor, 8 Fluid Channel Chip

Inputs	Name	Outputs	Unit	Comment	Formula
Physical Constants:	1.38E-23 k		J°K	Boltzman's const.	Assume MDC-90 electronics
	3.00E+02 T		°K	Temperature	40 samples per S-curve
					32 S-curves per second
LAPS parameters:	2.15E-08 Cs		Farads	LAPS shunt capacitance	
	1.00E+09 Rs		Ohms	LAPS shunt resistance	
Ccomponent Values:					
	3.50E-12 Cf		Farads	Feedback capacitance	
	2.00E+04 Rf		Ohms	Feedback resistance	
	5.11E+02 Rs1			I-V converter series resistance	
System paramentrs:					
	5.00E+03 f		Hz	LED operating frequency	
	5.70E-04 Ts		sec	Sampling interval	
	BW	877	Hz	Measurement bandwidth	$BW = 1/(2 \cdot Ts)$
Op-amp parameters:					
	4.00E-13 ia		arms/root Hz	OP-37 (MDC-90 electronics) amp current noise per sqt Hz	
	3.00E-09 ea		vrms/root Hz	amp voltage noise per sqt Hz	
Intermediate results:					
	iRs1	3.04E-21	arms^2	LAPS Rs noise current squared	$iRs1 = 4 \cdot K \cdot T \cdot Rs1 \cdot BW / (((Rs1)^2 + (.159/(f \cdot Cs))^2)^{.5})^2$
Noise components:					
	eno	1.67E-12	vrms^2	Amp voltage noise squared	$eno = (ea \cdot (BW)^{.5} \cdot (1 + Cs \cdot Rf / (.159)))^2$
	enRf	2.91E-13	vrms^2	Resistor thermal noise squared	$enRf = 4 \cdot K \cdot T \cdot BW \cdot Rf$
	iaRf	5.61E-14	vrms^2	Amp current noise squared	$iaRf = (ia \cdot (BW)^{.5} \cdot Rf / (1 + (6.28 \cdot f \cdot Rf \cdot Cf)^2)^{.5})^2$
	iRs1Rf	1.22E-12	vrms^2	LAPS shunt R noise squared	$iRs1Rf = iRs1 \cdot (Rf / (1 + (6.28 \cdot f \cdot Rf \cdot Cf)^2)^{.5})^2$
Noise calculations:					
	Noise	1.80E-06	Vrms	Total noise at output	$Noise = (eno + enRf + iaRf + iRs1Rf)^{.5}$

Fig. Sys-7

The second alternative detection scheme is gated integration (GI). In GI, the photocurrent from the LAPS is collected on a feedback capacitor rather than a resistor (see Figure Sys-8). Initial estimates showed that GI is capable of very rapid measurements (about 400  $\mu$ S per sensor) and could easily sequentially address a 32 channel chip by acquiring 32 or more S-curves per second with 40 points in each bias voltage sweep (similar to Cytosensor). An S/N model was developed for the GI scheme and is shown in Figure Sys-9. A key input parameter to the model is the charge collected from the LAPS device each time a light pulse is applied, qLAPS. This charge was measured experimentally to be about 10 picoCoulomb for a Cytosensor chip in a test fixture and must be scaled down to account for the smaller sensor areas of the 8 and 32 channel chips, respectively.

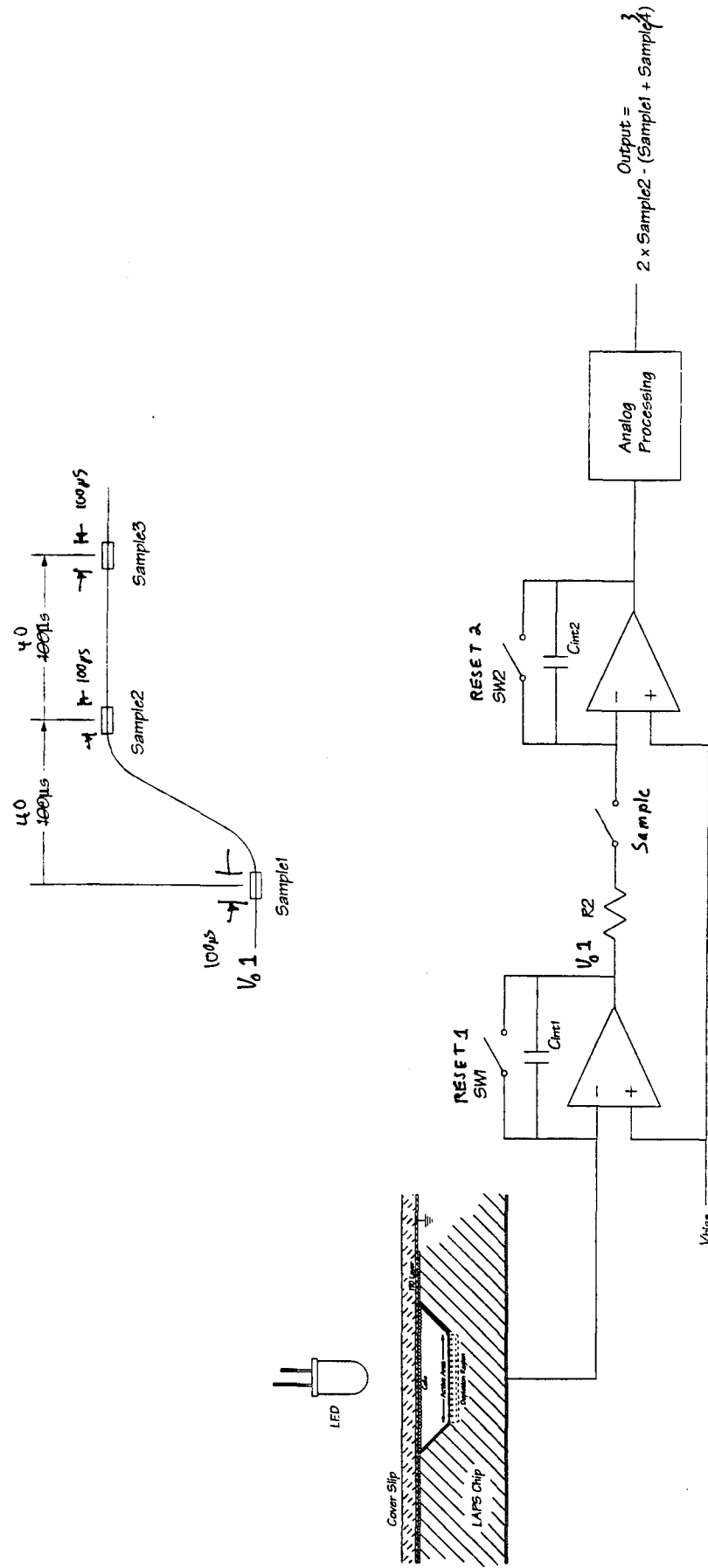
The results of our S/N analysis are summarized in Figure Sys-10 for the nine cases we wish to compare; three chips layouts and three separate detection schemes. In Figure Sys-10 (A) and (B), raw and normalized noise data are presented, respectively. The reader is reminded that the S/N for the back-side illuminated Cytosensor data is used as the reference standard.

For the 32 sensor chip, the best S/N appears to be associated with FDM, although the S/N for triple sampled GI is only about 30% lower than that for FDM. Given the large number of assumptions and approximations in this analysis, it would be imprudent to eliminate either detection scheme on the basis of our S/N analysis alone. For this reason, our initial approach was to develop STDM, GI, and FDM and use the one that worked best or first.

As it turned out, the FDM method was difficult to implement given the DSP hardware and the software development tools available on the market at the time of this research program. Generation and synchronization of 32 separate frequencies of known phase to existing DSP hardware proved to be a complex undertaking as was finding a high-speed, high-resolution A to D converter (16 bits at 100k Hz). It was also hypothesized that intermodulation products caused by the inherently non-linear properties of the LAPS device and the A to D converter could result in an unacceptable level of crosstalk between channels. Although in principle it is possible to overcome the problems with FDM described above, our FDM effort was discontinued since our efforts to implement the GI method were successful prior to completing the implementation of FDM. With GI working and having a higher potential S/N than STDM (see Figure Sys-10 (B)), our effort on STDM was also discontinued.

In Figure Sys-10 (B) it can be seen that single sampled GI gives a S/N of 0.22 normalized to Cytosensor. Unfortunately, experiments showed that double correlated sampling had insufficient crosstalk reduction to achieve acceptable levels when the sensors were sequentially illuminated at a rate of 32 S-curves per second. The crosstalk was hypothesized to be caused by photocurrent flowing in sensors which had been illuminated prior to the most recent one. The timing of the sequential sensor illumination scheme will be described in more detail later.

In order to better understand the temporal nature of the photocurrent signal from the LAPS, the SPICE model shown in Figure Sys-11 was developed. In the model, a Shottkey diode is used to simulate the depletion region of the LAPS device. Although



Schema, Gated Integrator

PL 7/26/94

Fig. Sys-8



# Noise Model for Gated Integrator LAPS Photodetector

Inputs	Name	Outputs	Unit	Comment	Formula
Physical Constants:	1.60E-19 q		Coulomb	electronic charge	
LAPS parameters:	2.15E-08 Cs		Farads	LAPS shunt capacitance	
	1.00E+10 Rs		Ohms	LAPS shunt resistance	
Component Values:					
	1.00E-10 Cf		Farads	Feedback capacitance	
	1.00E+09 Rf		Ohms	Feedback resistance	
System parameters:					
	4.24E-11 qLaps		Watts	rms optical power to LAPS	
	1.00E-05 Tr		sec	Sampling interval per channel	
	1.00E-04 Ts		Hz	Measurement bandwidth	$BW = 1/(2 \cdot Ts)$
		5,000	Hz		
	1.00E-04 T_2		sec	2nd integrator time	
	BW_2	5,000	Hz	2nd integrator bandwidth	
Op-amp parameters:					
	7.00E-15 ia		arms/root Hz	amp current noise per sqt Hz	AD745
	3.20E-09 ea		vrms/root Hz	amp voltage noise per sqt Hz	
Intermediate results:					
	iLaps	4.24E-06	arms	LAPS photo current	$iLaps = qLaps/Tr$
	Vout	0.42	volts	1st integrator output in Volts	$Vout = qLaps/Cf$
Noise components:					
	eno	2.39E-09	vrms^2	Amp voltage noise squared	$eno = (ea \cdot (BW_2)^{0.5} \cdot (1 + Cs/Cf))^{*2}$
	iaZf	2.45E-13	vrms^2	Amp current noise squared	$iaZf = (ia \cdot (BW)^{.5} \cdot Ts/Cf)^{*2}$
	isZf	6.78E-10	vrms^2	Shot noise squared	$isZf = (qLaps/q)^{*0.5} \cdot q/Cf)^{*2}$
Noise calculations:					
	Noise	5.54E-05	vrms	Total noise at output	$Noise = (eno + iaZf + isZf)^{*0.5}$
SNR calculations:					
	SNRp	1.63E+04	none	Photon limited noise SNR	$SNRp = (qLaps/q)^{*0.5}$
	SNRa	7.65E+03	none	Actual SNR from OP-amp output	$SNRa = qLaps/(Cf \cdot Noise)$

Fig. Sys-9

# Signal to Noise Ratio Analysis for LAPS Detection Schemes

## (A) RAW NOISE DATA

### Assumptions:

One pH reading per second for each sensor  
(one 40 point S-curve per sensor per second)

	capacitance nF	sensor area square mm	sequential detection (TDM)		parallel detection (FDM)	Gated Integration	
			S/N	noise (vrms)		0.1 ms sample S/N	triple sampled S/N
Cytosensor chip	1.6	2.36	3.53E+04	1.10E-07	6.01E+04	1.41E+05	1.15E+05
8 sensor chip	12.5	2	1.41E+04	5.90E-07	2.81E+04	3.64E+04	2.91E+04
32 sensor chip	21.5	1	2.35E+03	1.80E-06	9.39E+03	7.65E+03	6.25E+03

### Notes:

1. Shaded cell is bottom side illuminated. (iLAPS = 0.2  $\mu$ A). All others are top side illuminated.
2. iLAPS = 0.5  $\mu$ A rms @ Vpip for topside continuous detection with Cytosensor chip.
3. qLAPS = 0.1 nC @ Vpip for topside gated integration with Cytosensor chip.

## (B) NORMALIZED NOISE DATA

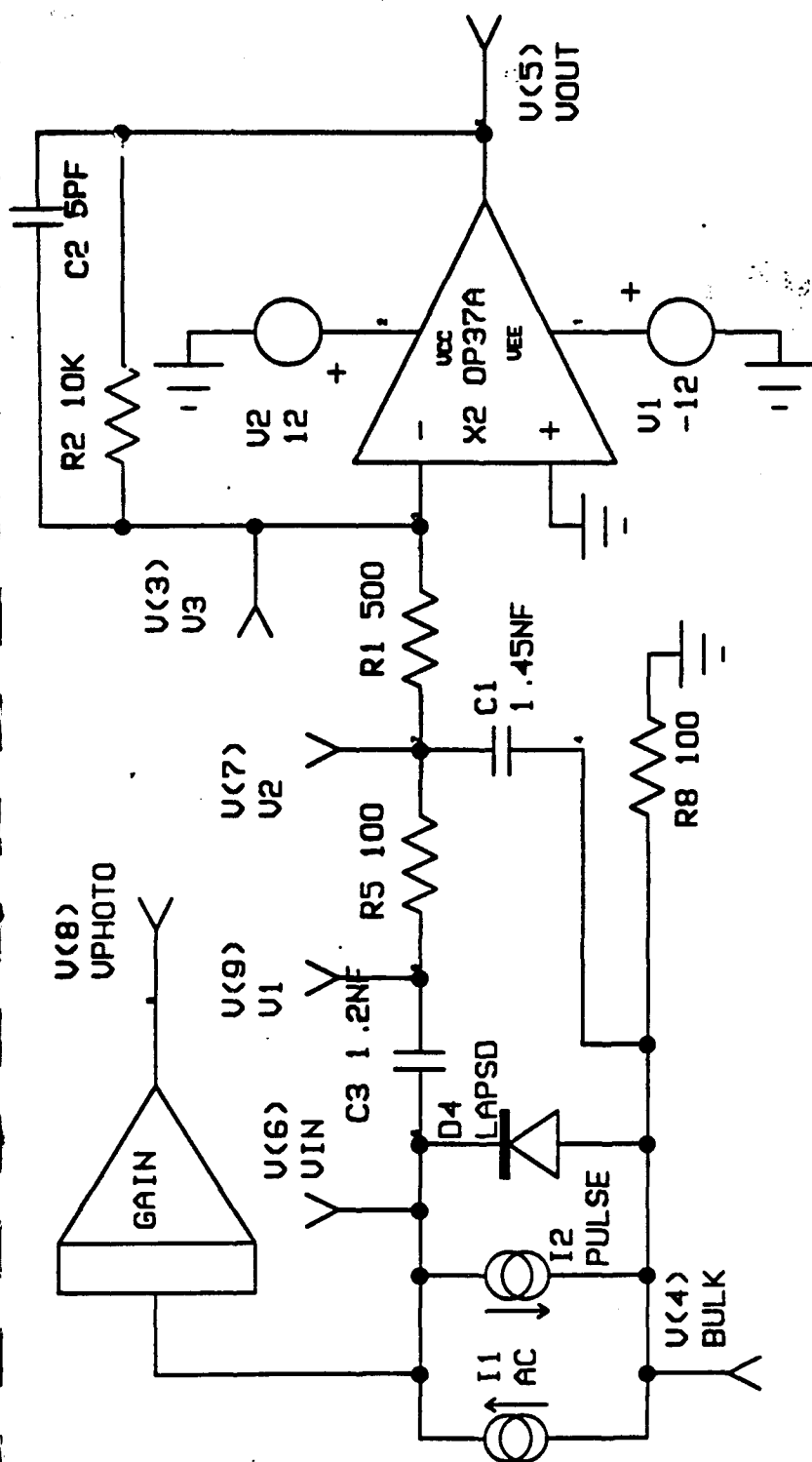
### Assumptions:

One pH reading per second for each sensor  
(one 40 point S-curve per sensor per second)

	normalized capacitance	normalized sensor area	sequential detection (TDM)		parallel detection (FDM)	Gated Integration	
			normalized S/N	sampling interval		0.1 ms sample normalized S/N	triple sampled normalized S/N
Cytosensor chip	1.00	1.00	1.00	18.2 ms	1.70	3.99	3.25
8 sensor chip	8.38	0.85	0.40	2.3 ms	0.80	1.03	0.84
32 sensor chip	13.46	0.42	0.07	0.57 ms	0.27	0.22	0.18

### Notes:

1. Shaded cell is bottom side illuminated.
2. All S/N are normalized to Cytosensor with 18.2 ms sampling interval.



**Fig. Sys-11. SPICE Model of LAPS**

this is only a crude approximation, the model does indeed provide a qualitative explanation for the dynamic performance of the LAPS device.

Figure Sys-12 shows the output of the model when the current source,  $I_2$ , is switched on and off repetitively. This corresponds to switching the LED on and off. Figure Sys-13 shows the output of an actual LAPS device printed from a digital oscilloscope. The lower trace in both figures is the LAPS photocurrent output. The upper trace in the simulation (Figure Sys-12) is the voltage across the diode, whereas in Figure Sys-13, the upper trace is the integral of the lower trace. Since the LAPS insulator effectively differentiates the photovoltage which is developed across the depletion layer, the integrated waveform shown in the upper trace is assumed to be a reasonable approximation of the internal photovoltage. The magnitude of the internal photovoltage can be estimated by dividing the charge output from the LAPS by the magnitude of the insulator capacitor. For the case shown in Figure Sys-13, the photovoltage is thus equal to  $0.33 \text{ nC} / 1.2 \text{ nF}$  or  $0.28 \text{ V}$ . Since this is in reasonable agreement with what one expects for the forward voltage of a Schottky diode, its use in the model appeared to be appropriate.

Several features of the model are helpful in explaining what was actually observed in implementing GI detection for the LAPS device. One can see that in both the model and the real photocurrent tracing, the amplitude of the negative going current pulse is lower than that of the positive pulse and its decay time is significantly longer. This can be explained as follows. When the current source in Figure Sys-11 is switched on, i.e., the light is switched on in an actual LAPS device, the voltage builds up very rapidly across the Schottky diode. Charging the diode capacitance causes it to become forward biased. When the current is turned off, the diode voltage decays very rapidly at first but rapidly slows down because the dynamic resistance of the diode increases exponentially as the diode current decreases. Thus the discharge time can be very long compared to the charge time. In fact, if the diode is not fully discharged when the light is turned on again, the situation shown in Figure Sys-12 will occur where the photovoltage does not return to the fully discharged state before the next light pulse occurs.

An additional feature of the actual LAPS device is that although the top of the photovoltage curve looks flat in Figure Sys-13, in a 32 sensor chip it actually has a slight slope due at least in part to changes in depletion capacitance of LAPS devices on the chip other than the one being photonically excited due to local surface potential variations.

Several innovations were required to make GI work. The first was to develop and implement the triple correlated sampling method illustrated in Figure Sys-8. The algorithm is to take  $2 \times \text{sample } 2 - (\text{sample } 1 + \text{sample } 2)$  as the sensor response. This algorithm was found to compensate to within 1% for the baseline drift due to slowly discharging LAPS devices. Unfortunately, the triple sampling algorithm reduces the S/N by a factor of  $\sqrt{1.5}$  or to 18% of Cytosensor. The second innovation was to recognize that it was better to leave the LEDs on during the sweep reset period, but with the photonic excitation at an extremely low level (about 1% of the normal "on" level). Low level LED "simmering" significantly reduced the amount of waiting time required to reach a stable photocurrent baseline at which time the sensors could be re-illuminated.

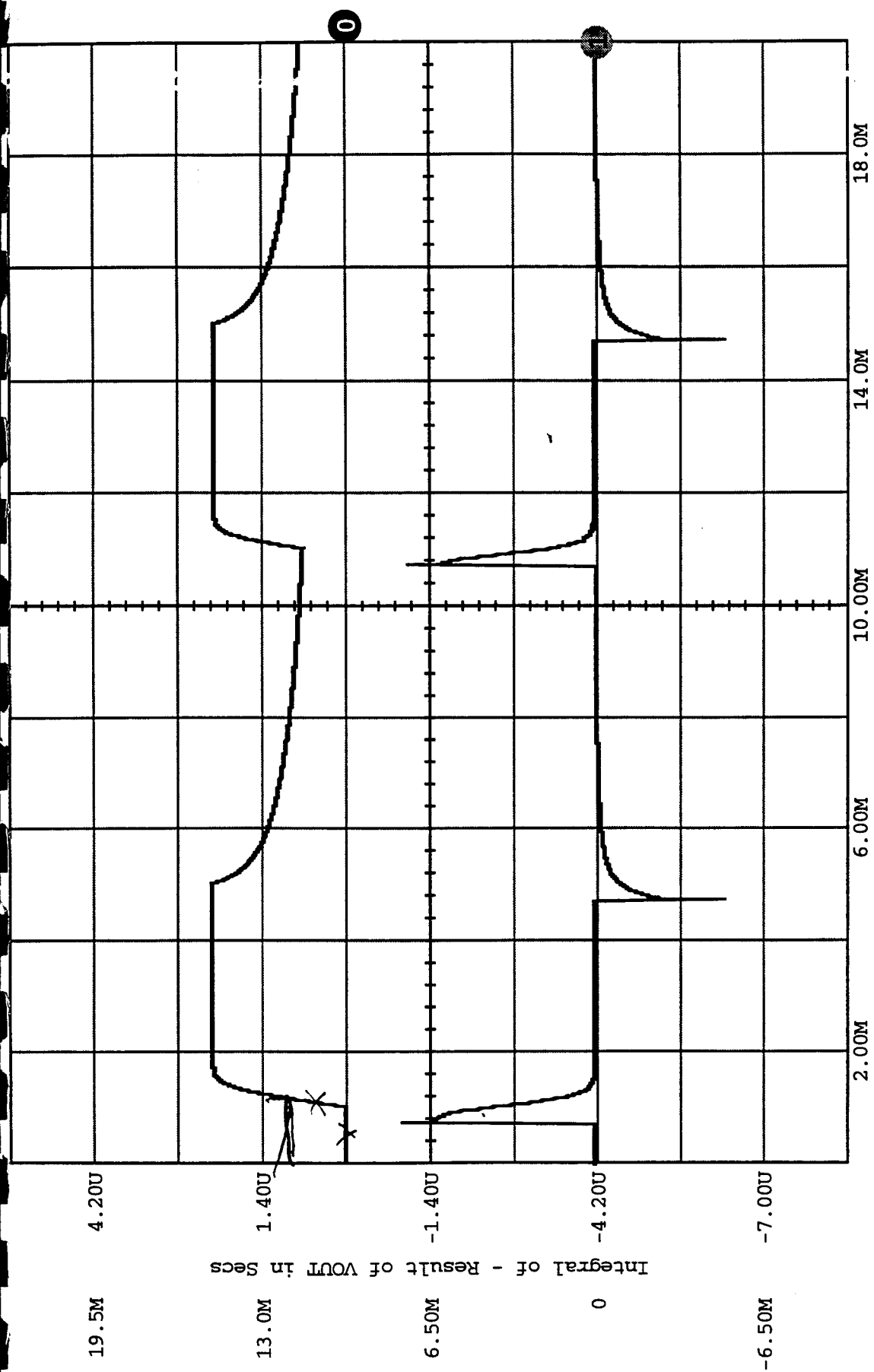


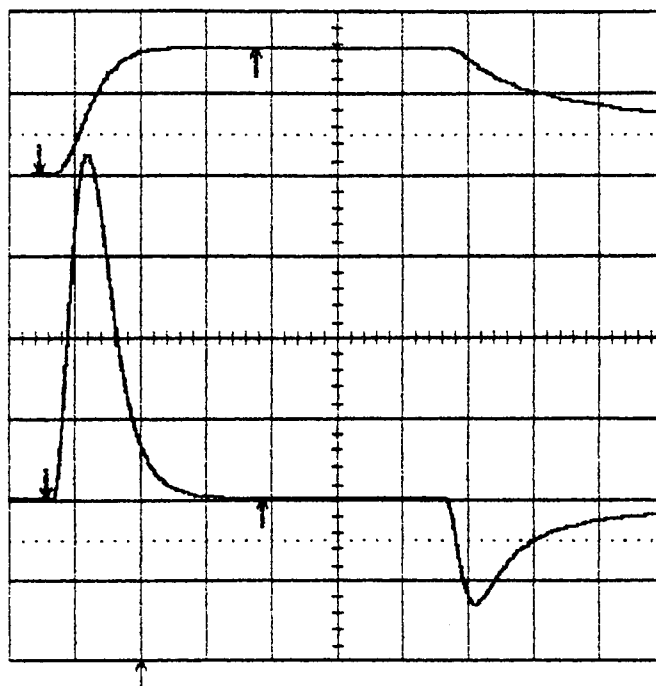
Fig. Sys-12. Output of SPICE Model

25  $\mu$ W

21-Oct-93  
16:59:40

0:  $\int (D+K) dt$   
10  $\mu$ s  
2.15  $\mu$ Vs  
3.3398  $\mu$ Vs  
1000 swps

0: Average(4)  
10  $\mu$ s  
100 mV  
0.93 mV  
1000 swps



MEASURE

OFF **Cursors**  
Parameters

mode  
**Time**  
Amplitude

type  
**Relative**  
Absolute

Reference  
cursor  
Track **Off** On

Difference  
cursor

.1 ms

1 50 mV AC  $\boxtimes$   
2 2 mV DC  $\boxtimes$   
3 0.97 V DC  
4 .1 V DC

$\Delta t$  32.95  $\mu$ s  $\frac{1}{f_c}$  30.349 kHz



Ext DC 1.97 V

☐ AUTO

50 Ms/s

21-Oct-93

MEASURE

Fig. Sys-13. Experimental LAPS Output

The third innovation was to synchronize the sample taking process to the line frequency.

Each voltage sweep step and subsequent photocurrent measurement (set of 32) are spaced at intervals of 16.67 ms. This insures that any constant line interference will appear as a constant offset in the output data and will therefore be rejected by the triple correlated sampling algorithm. The integration time for each of the three samples is 100  $\mu$  sec. and the time between samples is 40  $\mu$  sec. At the end of each sweep, about 330 ms is provided to reset the sweep, to allow the LAPS devices to equilibrate to the LED simmer levels, and to transfer the data acquired for the 32, 40 point sweeps from the voltmeter to the computer.

Our final challenge was to find a way to gain a factor of five in S/N in order to achieve performance equivalent to Cytosensor. This was accomplished by implementing an improved algorithm for finding  $V_{pip}$  from the 40 point S-curve. The analog data from each sensor were digitized using an HP 3458A voltmeter, which contained a true 16 bit A-D converter. The raw data were transferred to a Macintosh Quadra 840AV computer running a LabVIEW application program. This computer was referred to as the acquire machine or "Allen." The data was then transferred to a second computer, "Gertrude," which handled the graphical user interface. The algorithm used to find the  $V_{pip}$  ran on the Gertrude computer. The raw data set for each 40 point S-curve was multiplied by a Blackman-Harris windowing function and then convolved with the previous reading. The peak in the convolution curve was found by finding the maximum value of a polynomial function which was fit to the convolution data set. It was found that this algorithm provided a S/N improvement of 5-10 over the algorithm used in Cytosensor, thus bringing the S/N of the 32 sensor chip to a level comparable to Cytosensor under ideal conditions.

In practice, the actual S/N achieved with LAPS devices embedded in an instrumentation system and viewed at the level of acidification rate noise is greater than expected from the electronics noise of the detection circuit. For Cytosensor, one way to show this is to start with the best case  $V_{pip}$  noise measured on a production Cytosensor (about 10  $\mu$ V rms) and back-calculate the noise expected at the output of the detection circuit. Assuming an S-curve slope of 2  $\mu$ A/V, one calculates the noise at the output of the I-V converter to be about 0.4  $\mu$ V rms whereas the S/N model predicts only about 0.1  $\mu$ V rms. This discrepancy is accounted for by including the effects of noise pick-up from internal and external sources of electromagnetic interference along with the effects associated with the LAPS electrical contacts and fluidic system as well as noise associated with the LAPS surface to fluid interface and reference electrode.

In very controlled experiments where the effects of electromagnetic interference and LAPS noise sources were minimized, it was found that the  $V_{pip}$  noise from each sensor on the 32 sensor chip with GI detection was comparable to Cytosensor ( $V_{pip}$  noise between 20 and 30  $\mu$ V rms). However, when the system was operated in the presence of the motors and electronics required to run the complete automated fluidics sampling system, the performance at the level of acidification rate was degraded by as much as a factor of 10 from that of Cytosensor. Under good conditions, and for short time intervals, the acidification rate noise in Cytosensor is about  $\pm 1$   $\mu$ V/sec peak to peak. For the 32 sensor chip, the acidification rate noise was found to be between  $\pm 5$  and  $\pm 10$   $\mu$ V/sec peak to peak depending on conditions.

# Prototype High-Performance Microphysiometer

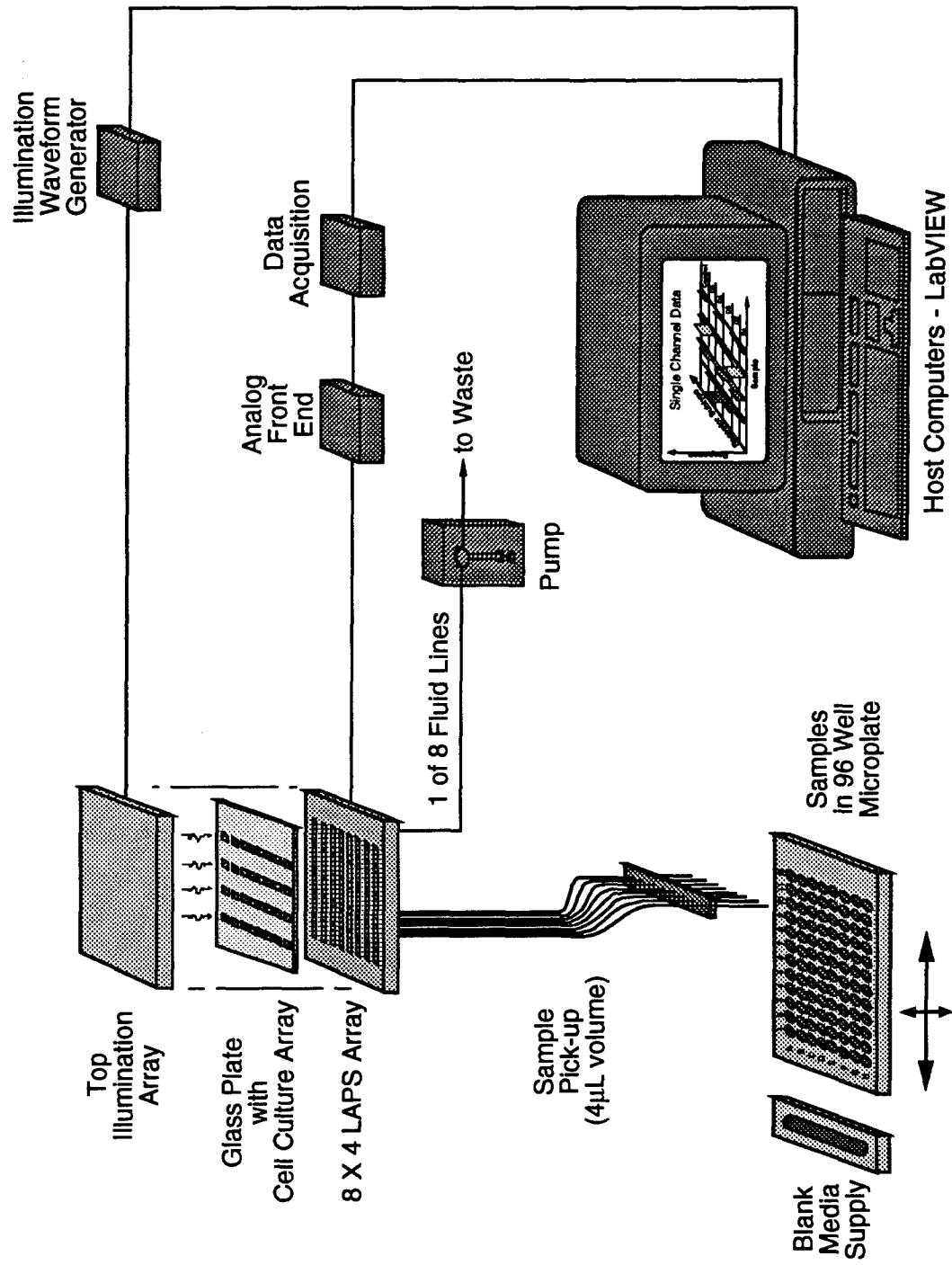


Fig. Sys-14



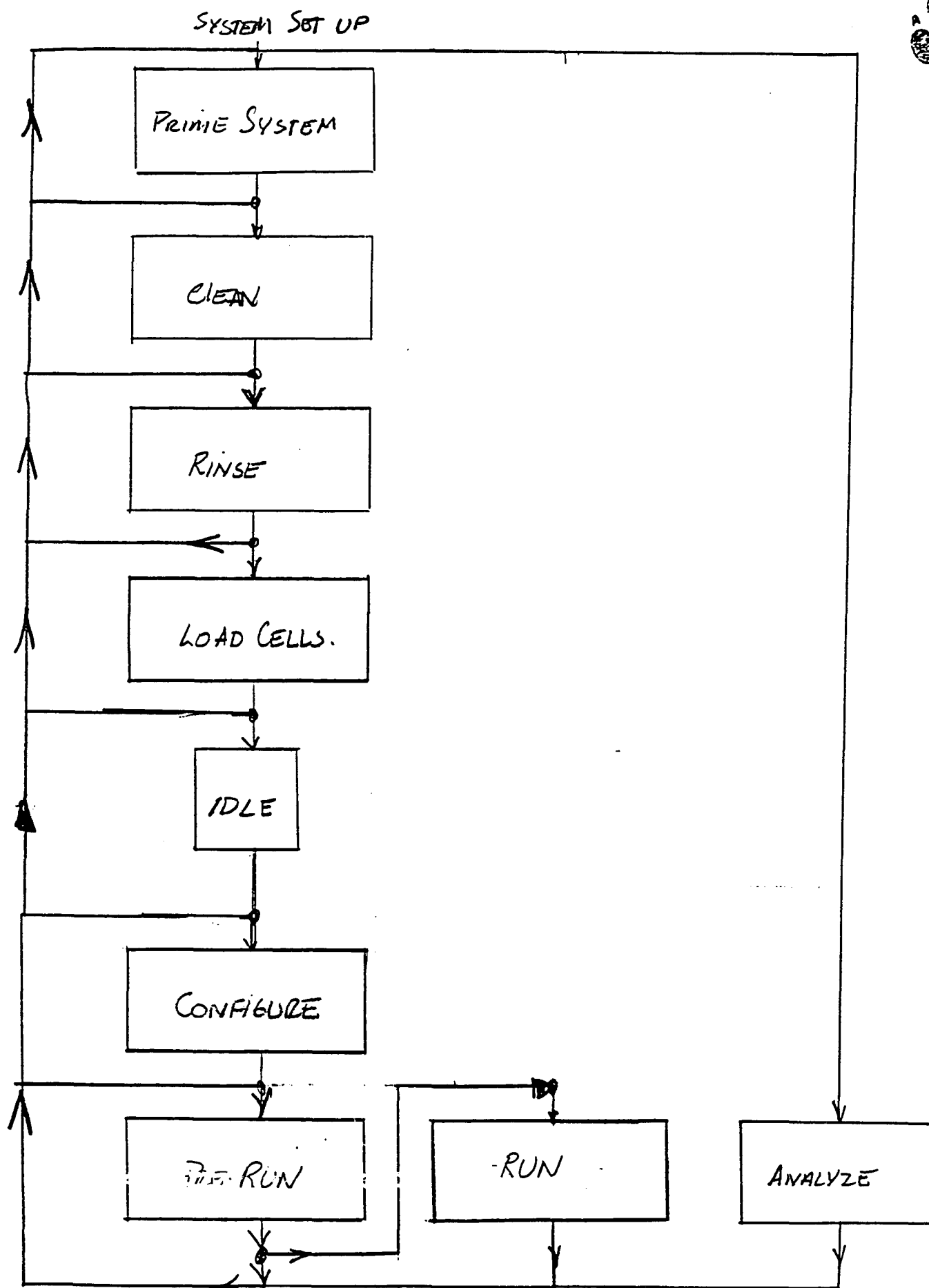


Fig. Sys-15. System Setup Operations

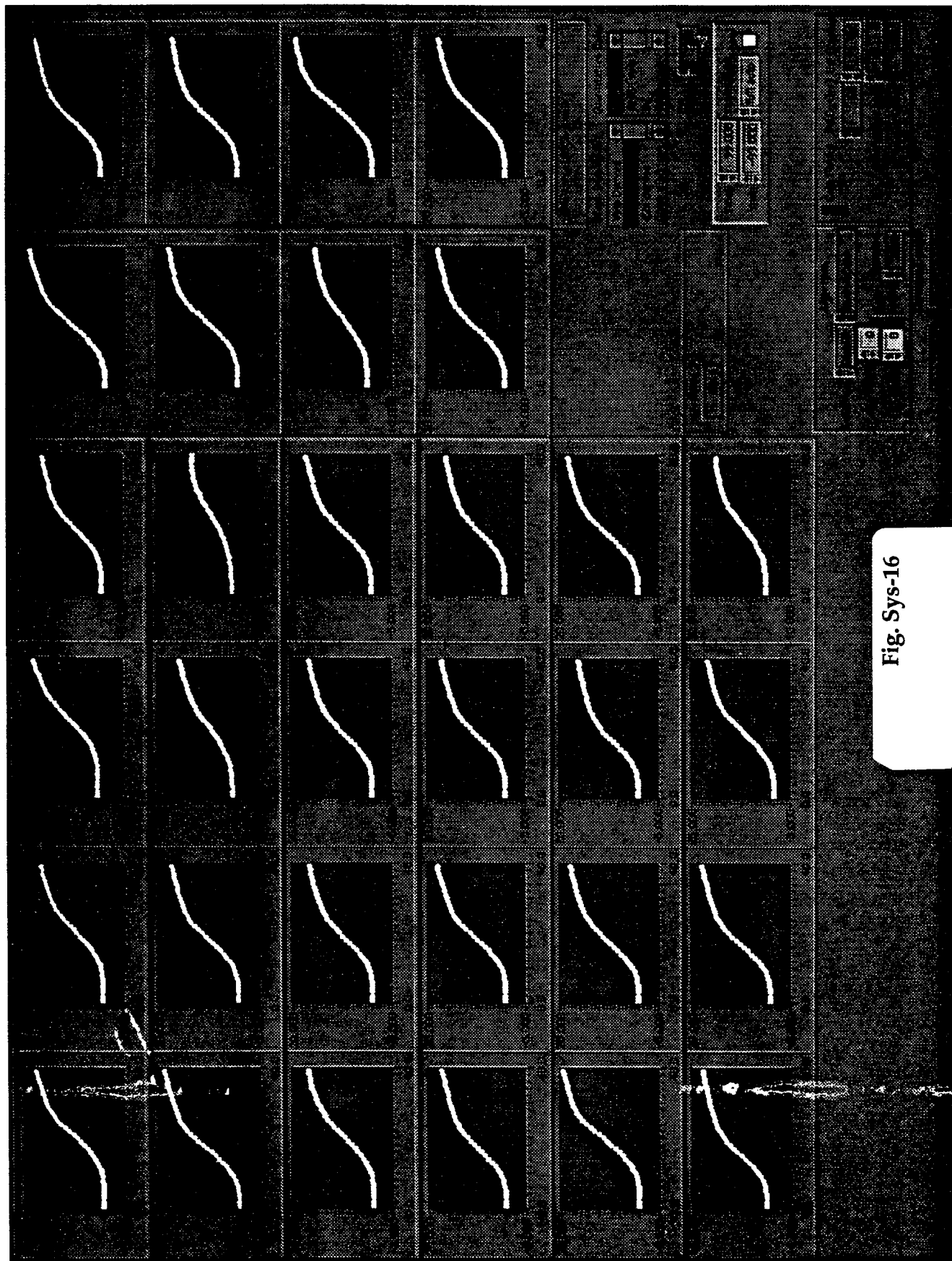


Fig. Sys-16

SIS-19

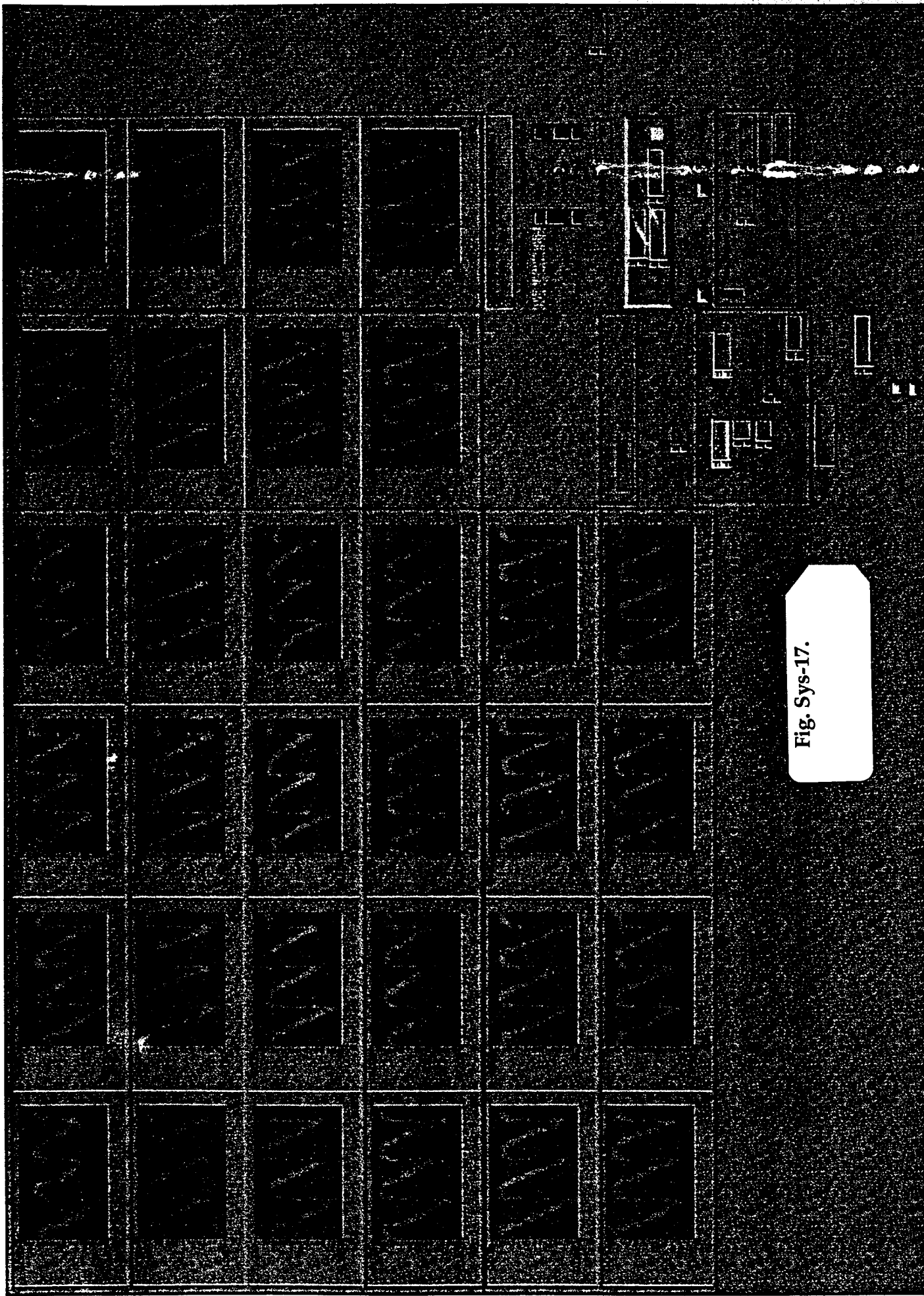


Fig. Sys-17.

The operator's manuals for the software are included in Appendix 1

## **2. Example experiment on instrument**

The structure of an experiment to demonstrate the detection of neuroreceptor activation in the new instrument is shown in Figure Sys-18. We loaded the same four cell types into each of the eight channels of the sensor flow chamber: cells exogenously expressing the m3 muscarinic receptor, the  $\beta_2$  adrenergic receptor, and the  $\mu$  opioid receptor, as well as control cells not exogenously expressing any receptor. CHO-K1 cells were used for all host cells and for the control. In different flow channels the cells were challenged with a muscarinic agonist (carbachol), an adrenergic agonist (isoproterenol), an opioid agonist (DAGO), or a mixture of the three. This was done in duplicate to fill the eight channels. Figure Sys-19 summarizes the results obtained in the microphysiometer within ten minutes of exposure of the 32 samples of cells to the test fluids. It is apparent that in this assay the agents displayed appropriate pharmacological selectivity.

- **Demonstrate metabolic signal from tissue slices.**

The standard cell chambers used on the Cytosensor Microphysiometer are unsuitable for tissue slices, since they do not deliver oxygen and nutrients efficiently to the side of the slice that is in contact with the LAPS chip. Therefore, we designed and fabricated a plunger (plungers are the components of the cell chambers that house the bulk of the fluidics) optimized for use with tissue slices; see Figure Sys-20. This new design bathes both sides of the slice in culture medium and hence maintains tissue viability much better than the standard plunger design used for cultured cells. It has been possible to keep slices of brain (perhaps the most delicate tissue) alive in the microphysiometer for several days; see Figure Sys-21. We have also studied slices of heart, skeletal muscle, fat, liver, and kidney. Data from brain and kidney slices, showing the metabolic effects of manipulating the ionic permeability of the cell membranes, are shown in Figure Sys-22.

Having accomplished the contract goal of demonstrating metabolic signals from tissue slices, we investigated the feasibility of detecting pharmacological responses from the slices by microphysiometry. With some exceptions, the slices proved to be much less responsive than cultured cells. The reasons for this are not proven, but we think that two contributory factors are: (1) Most cells *in vivo* rely on aerobic metabolism much more than glycolysis, the opposite of cells in culture. We have evidence that often the microphysiometric signals that we see associated with receptor activation are associated with glycolysis. (2) Many tissues comprise a variety of kinds of cells, only one of which might respond to a particular pharmacological stimulus; this reduces the signal-to-background ratio. For example, if a sub-population of 10% of the cells in a tissue responds by increasing acidification rate by 20% and the other 90% do not respond at all, the overall acidification rate only changes by 2%. Tissue slices look less promising for the detection of CBW agents than they did at the time of our proposal.

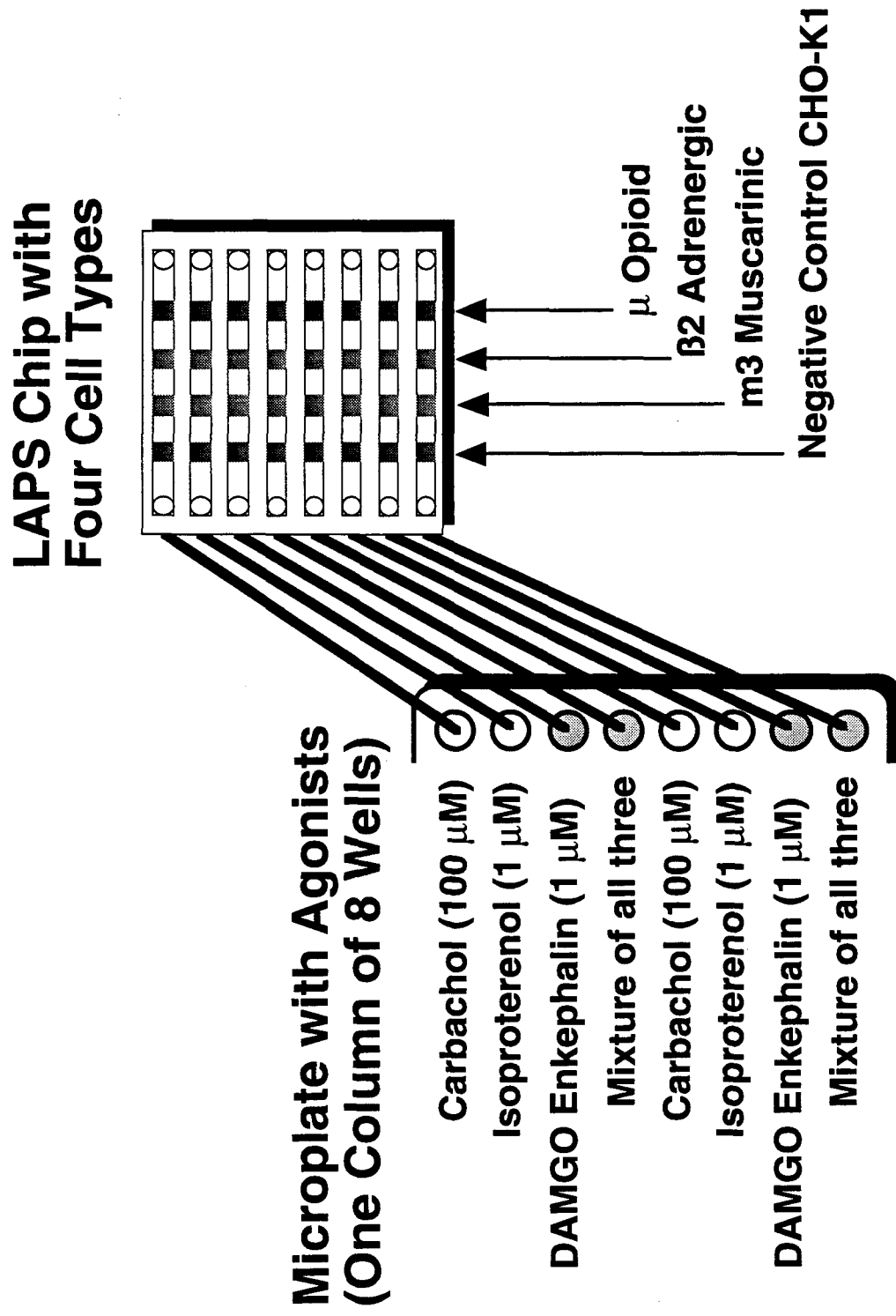


Fig. Sys-18 Layout of experiment on high-performance microphysiometer

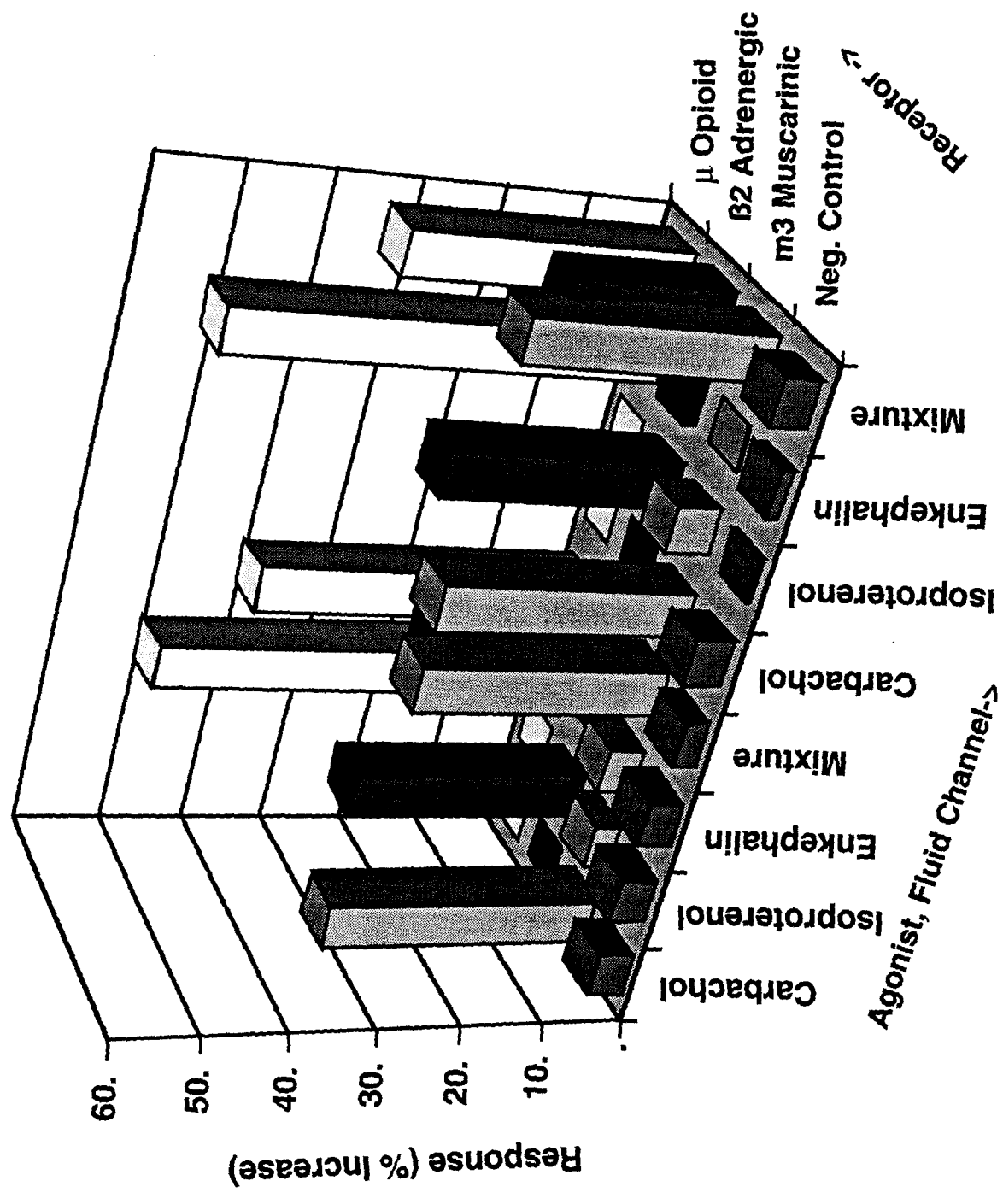
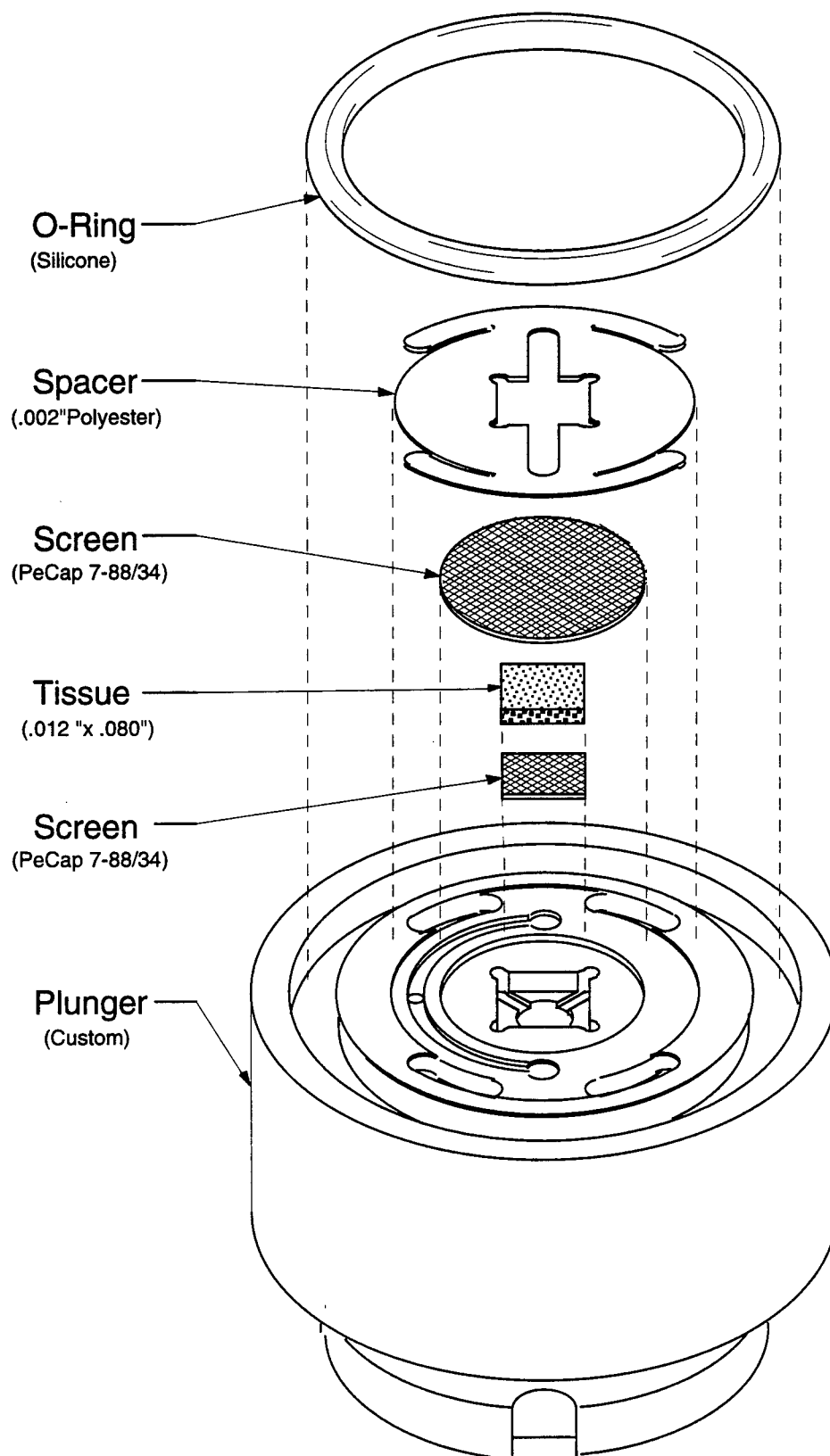


Fig. Sys-19 Results of experiment on high-performance microphysiometer



**Fig. Sys-20 Tissue-Slice Plunger**

# Maintenance of Metabolic Activity of Rat-Brain Slice for Three Days

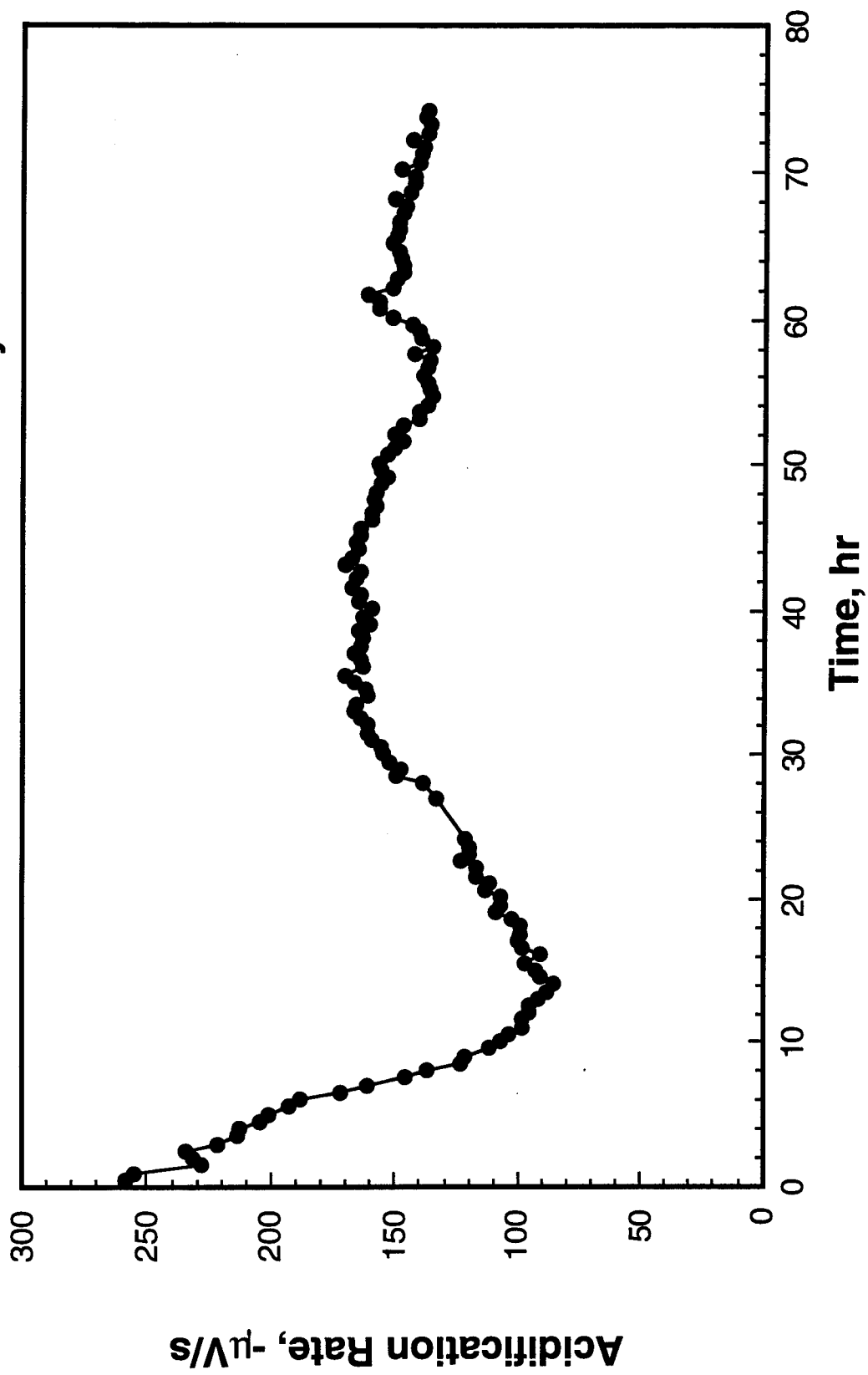


Fig. Sys-21.



## Effects of moneisin & ouabain on kidney and brain slices

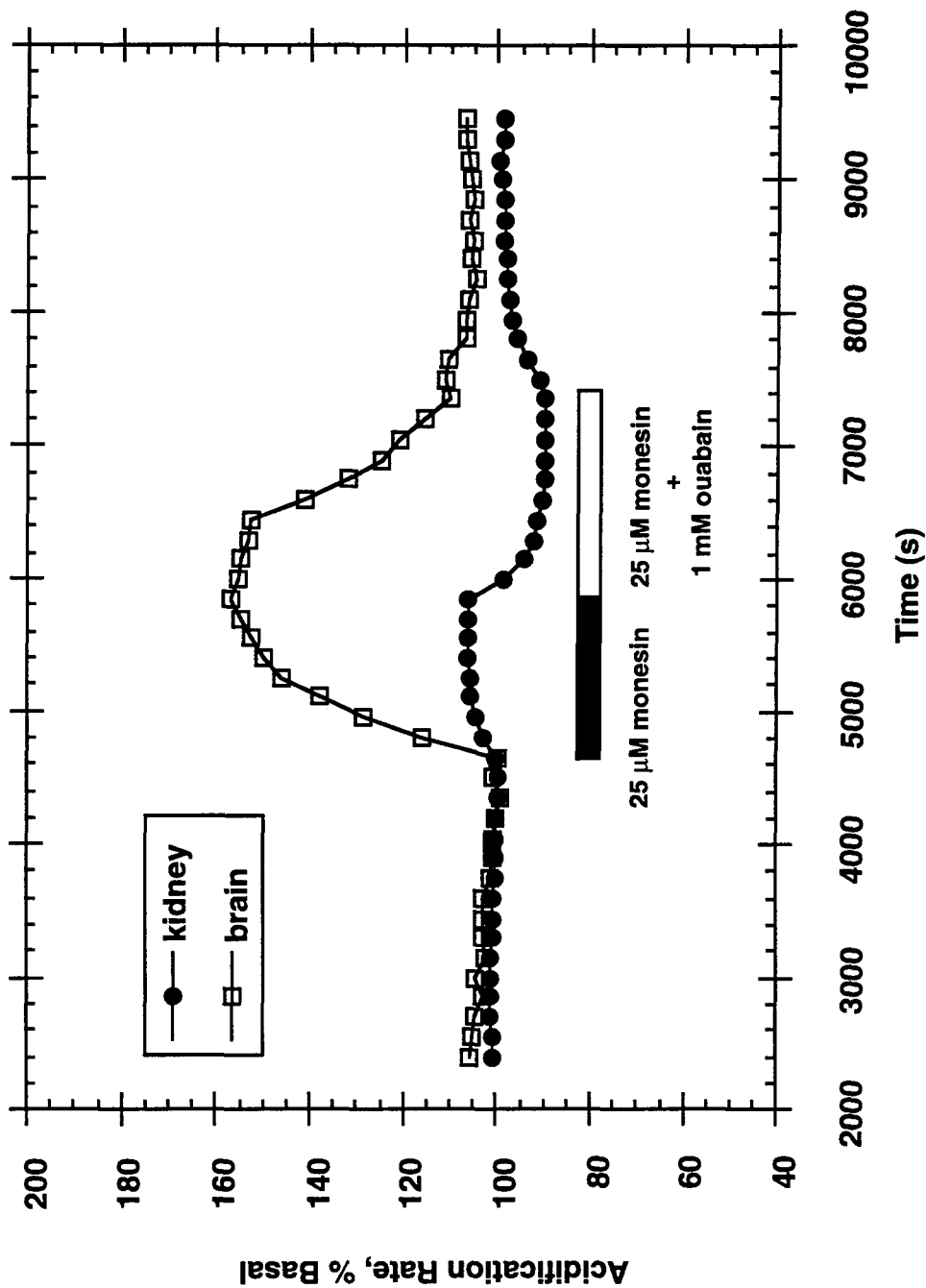


Fig. Sys-22 Disrupting ionic permeability of the cell membranes of tissue slices detectably alters metabolic activity. This effect is antagonized by ouabain, an inhibitor of the Na pump

- **Demonstrate virtual electrodes for tissue slices .**

This was a more high-risk foray off the main thrust of the contract, based on the following concept. The LAPS is sensitive to the potential between the controlling electrode and the bulk of the semiconductor, which includes a surface potential that is typically modulated by pH. However, electrically active cells can alter the electrical potential in the surrounding aqueous medium; this is the basis of extracellular recording of action potentials. Such effects can appear as an RC circuit with voltage sources between the controlling electrode and the bulk of the semiconductor, so it should be possible to measure them with a LAPS under the proper conditions. Some of the important technical issues include signal-to-noise ratio for small illuminated regions and fast time resolution. The potential advantage over the use of conventional metal electrodes is that it should be possible to make measurements wherever cells happen to be, just by choosing the site of illumination, while conventional microelectrodes are either tedious to position or are fixed in place by microfabrication.

Last year Prof. Hermann Gaub, a well-known biophysicist at Ludwig-Maximilians University in Munich, approached us about collaborating on virtual electrodes. We agreed and have been working with his group since then. The plan is to begin by characterizing and optimizing the spatial resolution of LAPS measurements to determine whether it is indeed possible to collect data from regions about the size of individual cells. Preliminary data suggest that this is so. In parallel, a model biological system is being set up, comprising embryonic heart myocytes. In culture under appropriate conditions these cells organize into functional sheets that resemble the architecture of the intact tissue, and they can be made to beat.

## **C. BIOLOGY**

- **Demonstrate detection of anti-metabolic agents in thawed cells using LAPS.**
- **Demonstrate detection of anti-receptor agents in thawed cells using LAPS.**
- **Demonstrate detection of anti-metabolic agents in rehydrated cells using LAPS .**
- **Demonstrate detection of anti-receptor agents in rehydrated cells using LAPS .**

Since mammalian (human) cells are the targets of CBW agents, mammalian cells are the natural choice to incorporate into a broad-spectrum CBW detection instrument. However, as they are normally used in culture, mammalian cells require a degree of environmental control that might be difficult to achieve in the field. Part of the work on the contract has been devoted to overcoming this problem by two distinct approaches: Increasing the durability and "shelf life" of mammalian cells during storage before use, and incorporating mammalian targets into more durable cells (yeast) that can be stored dehydrated until use.

### **1. Cryopreserved mammalian cells.**

Mammalian cells for use in cell biology are routinely cryopreserved at liquid-nitrogen temperatures and remain viable for years under those conditions. Cryopreservation of such cells in disposable cell-capsule containers for use in a microphysiometer soon after thawing would significantly enhance the utility of mammalian cells in the field. Small transportable liquid-nitrogen dewars are available that can maintain cryopreserved cells for a week without recharging, and indefinitely with recharging. This would obviate the need for cell-culture facilities at the point of use.

In typical laboratory use, cells are thawed and then allowed to proliferate for several days before use. It is the descendants of the cryopreserved cells that are used, not the cryopreserved cells themselves. Prior to our studies, little work had been done to determine how quickly metabolic and receptor responsiveness is restored in cells after thawing.

We were able to freeze cells in the cell capsules that fit the commercial Cytosensor® Microphysiometer System, watch the restoration of metabolic activity one to two hours after thawing, and determine the responsiveness of the cells. Responses to anti-metabolic agents were as expected for never-frozen cells and are summarized in the table below. Effects of a variety of agents that activate receptors were likewise substantially similar to the effects in never-frozen cells. These results are presented in detail in a journal article, attached in Appendix 3 (Kuo et al., 1993).

Effects of anti-metabolic agents on TF-1 human erythroleukemia cells		
Agent	Concentration	Effect on acidification rate
Ionomycin	1 $\mu$ g/mL	Immediate transient increase, typically 50-100%
Dinitrophenol	1 mM	Transient increase, followed by ~20% decrease within 20 min.
Ouabain	10-100 $\mu$ M	Immediate ~15% decrease, followed by gradual decline in rate; effect much less for 0.1 or 1 $\mu$ M
2-deoxyglucose	5 mM	Immediate ~40% decrease (with 11 mM glucose present )
Oxamate	5 mM	Immediate ~50% decrease

Routine optimization of freezing conditions improved the results for adherent cells over those reported by Kuo et al. This work on cryopreservation has been sufficiently successful that we often use recently thawed cells for cell-biology work at Molecular Devices.

## 2. Rehydratable cells (yeast).

Dehydrated yeast would be easy to store and robust once stabilized after rehydration. We first sought to verify that stable metabolic activity could be obtained shortly ( $\leq 1$  hour) after rehydration. Next, and more importantly, we sought to determine whether microphysiometry could detect the activity of agents that alter the metabolism or receptor behavior of mammalian cells could be detected with suitably constituted yeast.

A sample of commercial active dry baker's yeast was rehydrated and placed in a Cytosensor Microphysiometer. As is shown in Figure Bio-1, stable metabolic activity, with a slow increase due to cell growth, was seen essentially immediately. These cells responded to a metabolic insult (the glycolytic inhibitor 2-deoxyglucose) in the expected way. In another experiment, not shown here, a proton-ATPase inhibitor (miconazole) also inhibited cellular metabolism.

Expressing mammalian receptors and ion channels in the plasma membranes of yeast so that they couple to the biological processes of the yeast has been more difficult. After our original proposal for the contract, a paper appeared reporting the expression of a mammalian adrenergic receptor in the yeast *S. cerevisiae* (Thorner & Lefkowitz paper). To achieve functional activity of the receptor, it was also necessary to express a mammalian accessory protein, a G protein.

We chose a different approach. Another species of yeast, the fission yeast *S. pombe*, in many ways behaves more like a mammalian cell than does *S. cerevisiae*. Therefore, we reasoned that it might not be necessary to co-express any mammalian accessory

# Inhibition of Metabolism of Freshly Rehydrated Yeast

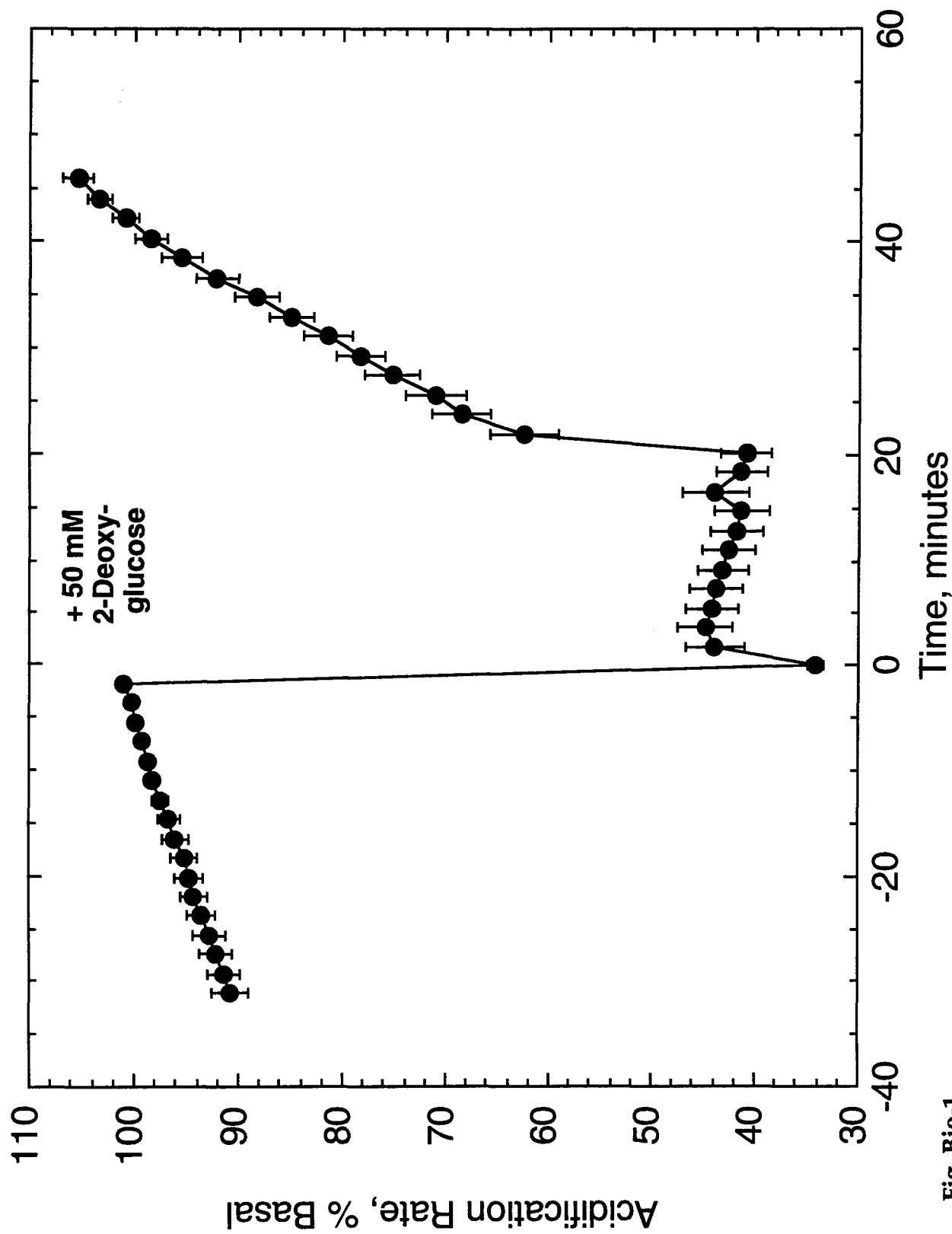


Fig. Bio-1

proteins with the receptors. By using this and a variety of other strategies on both types of yeast, we were unable to detect functional activity of exogenously expressed mammalian G-protein linked receptors. That this is a difficult problem has been confirmed by colleagues in the pharmaceutical industry, who have made similar attempts.

On the other hand, we have successfully used microphysiometry to observe changes in the activity of a variety of mammalian (and other) ion channels exogenously expressed in yeast. Ion channels are the targets of many natural toxins and are strong candidates for targets of CBW agents. One example is the inward-rectifier potassium channel (KIR) expressed in the mammalian heart muscle, which regulates the heartbeat. In collaboration with Dr. Steven Kurtz of Bristol-Myers Squibb we have demonstrated that this channel protein can be expressed functionally in the yeast *S. cerevisiae* and that microphysiometry can promptly and reliably detect the presence of agents that block its function in that environment. See, for example, Figure Bio-2.

Similar successes include a member of the widely distributed Shaker family of potassium channels (in collaboration with Prof. Toshi Hoshi of Iowa State Univ.) and the proton channel from influenza virus (in collaboration with Dr. Kurtz). The latter work has been published as Kurtz et al. (1995); see Appendix 3.

In summary, microphysiometry using yeast is an efficient way to detect general metabolic insults and appears to be an excellent method of monitoring the activity of a variety of ion channels. It may be possible to monitor the activity of G-protein linked receptors in this way, but that is more difficult and is as yet unproven.

- **Demonstrate enzyme capability and sensitivity in cell-system format.**
- **Demonstrate immunoassay capability and sensitivity in cell-system format.**

Microphysiometry is an excellent means of detecting most CBW threats, but of course it has limitations. By microphysiometry here we mean our cell-based LAPS detection scheme. We have investigated how a single LAPS-based platform can be generalized beyond microphysiometry to extend its utility to areas not best addressed by cell-based assays.

For example, the anticholinesterase war gases are directed against enzymes rather than receptors (and extracellular enzymes, at that). Although it may be possible to construct cell-based detection schemes for such agents, direct detection of changes in enzyme activity is probably to be preferred. In an earlier ARPA/ARO contract, we demonstrated that LAPS can be used to detect the activity of acetylcholinesterase sensitively by monitoring changes in pH (acetylcholine  $\rightarrow$  choline + acetic acid). This was shown in a system rather unlike a microphysiometer, and a goal of the present contract was to show that anticholinesterase agents could be detected by monitoring enzyme activity in a microphysiometer.

Eel AChE was derivatized with biotin using maleimide chemistry and was stably but non-covalently linked to biotinylated nitrocellulose membrane (100  $\mu$ m thick) via a

# Microphysiology Detects Blocker of Mammalian Ion Channel Expressed in Yeast

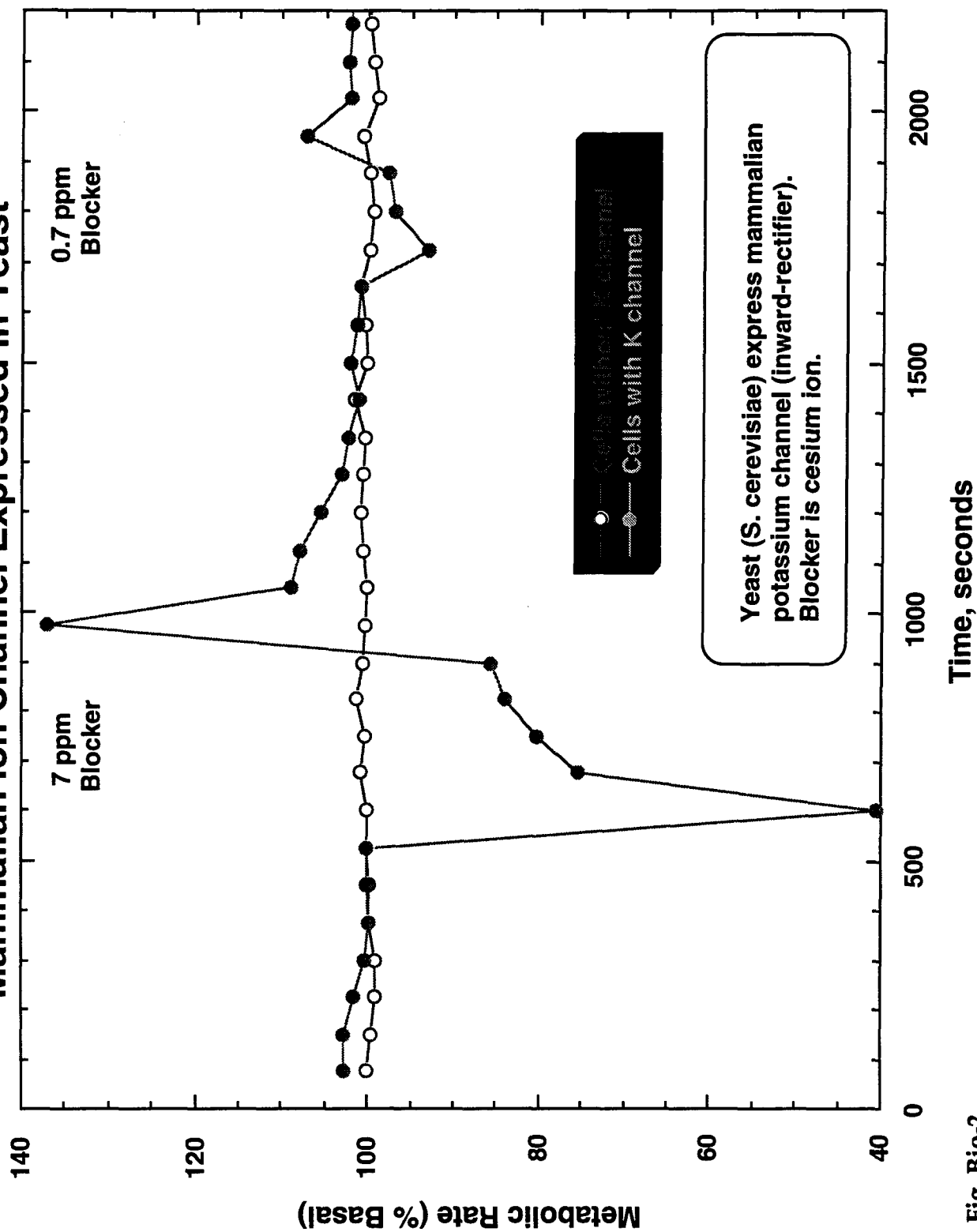


Fig. Bio-2

streptavidin bridge. The membrane was cut into circles 5mm in diameter and put into slightly modified microphysiometer cell capsules in place of cells. A schematic cross-section of this system is shown in Figure Bio-3.

Instead of cell-culture medium, a substrate solution was used: 1 mM acetylcholine, 1 mM phosphate, 150 mM NaCl, pH 7.0, temperature 25 C). The same start-stop fluidic protocol used for cells was employed, and the output of sensor voltage vs. time closely resembled that for cells. Acidification rates were relatively stable, decaying with a half-life of greater than ten hours.

Di-isopropylfluorophosphate (DIFP), a potent inhibitor of AChE, was introduced via an injection loop (100  $\mu$ L, 100  $\mu$ M, or 10 nmol in all). The enzyme was incubated with the inhibitor for five minutes with the flow off. After flow resumed and the DIFP solution was replaced with substrate solution, measurement of acidification rates resumed.

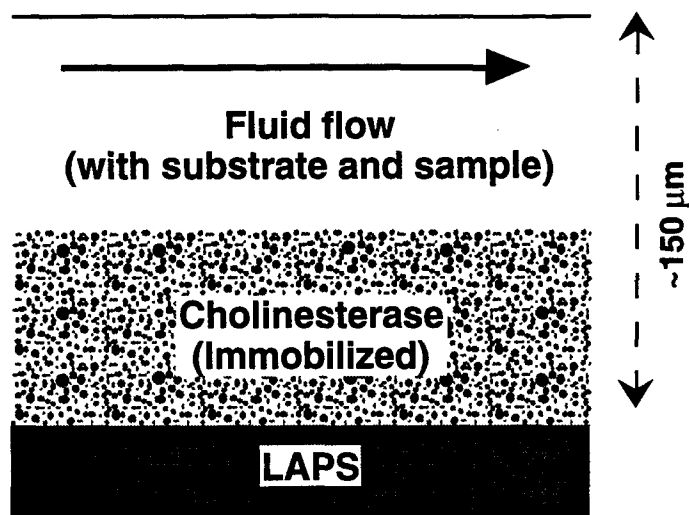
Inhibitions of 10% to 24% of the acidification due to the activity of AChE were obtained; Figure Bio-4 shows one such result. A second similar bolus of DIFP (cumulatively 20 nmol) further reduced enzyme activity, cumulatively by 24% to 43%. The inhibition of AChE by organophosphates is reversed by treatment with 2-pyridine aldoxime methiodide (2-PAM). Using the same fluidics protocol, the enzyme was exposed to two boluses of 1  $\mu$ mole each of 2-PAM (100  $\mu$ L, 10 mM, 5 min). Substantial regeneration of enzyme activity was observed.

The lower limit of detection of DIFP using the above protocol was about 1 to 2 nmol. Easily envisioned modifications of the microphysiometer could reduce the volume of DIFP solution by a factor of 10 without substantially decreasing the time of exposure of the enzyme to the inhibitor. Coupled with improvements in precision, the lower limit of detection of DIFP could rather easily be improved to about 100 pmol or below.

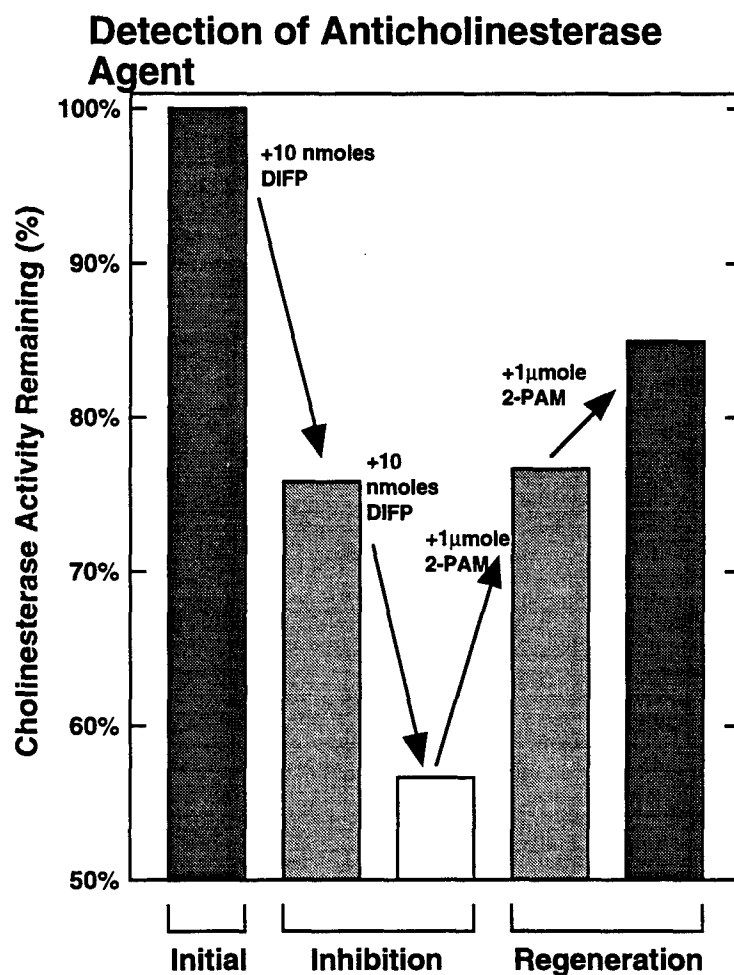
Having shown an enzyme-detection capability in microphysiometer format, we began to work on demonstrating the same for immunoassays. Immunoassays do not report functional consequences of exposure to an agent, but they are capable of identifying the presence of a particular agent if specific antibodies are available. Thus, they complement the cell-based functional detection of microphysiometry. The Threshold<sup>TM</sup> Immunoassay System, a LAPS-based immunoassay system developed by MDC, has been of significant use in CBW detection, and has been adopted by the U.S. Army and allied forces. We sought to adapt Threshold principles to the microphysiometer format.

A tissue slice plunger (see task earlier in this report) was modified to perform immunoassays using Cytosensor. As seen in Figure Bio-5, the filtration membrane is located precisely where the tissue slice and screens holding the tissue slice would be. The sample (ricin toxin A chain) is preincubated with Threshold<sup>TM</sup> capture reagent (biotinylated antibody & fluoresceinated antibody) and loaded into the Cytosensor through the injection loop (roughly 200 $\mu$ L). The sample/capture reagent bolus is then filtered through the membrane in the plunger using Cytosensor's regulated peristaltic pumps. This is followed by a bolus of Threshold Enzyme Reagent (anti-fluorescein-urease, 100-400 $\mu$ L). Figure Bio-6 shows the configuration of fluid lines on Cytosensor necessary to deliver the sample/ capture reagent and enzyme reagent to the membrane. Air bubbles are used to keep the fluid boluses intact. They are removed by

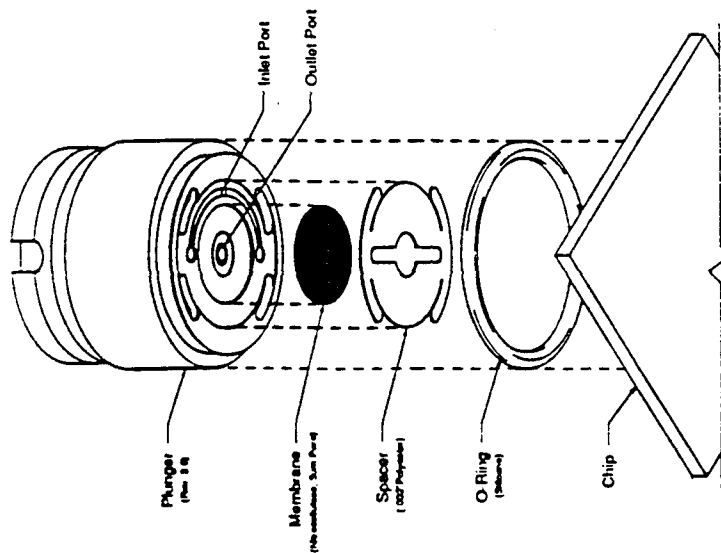




**Fig. Bio-3** Cross section of flow chamber for detection of anti-cholinesterase agents

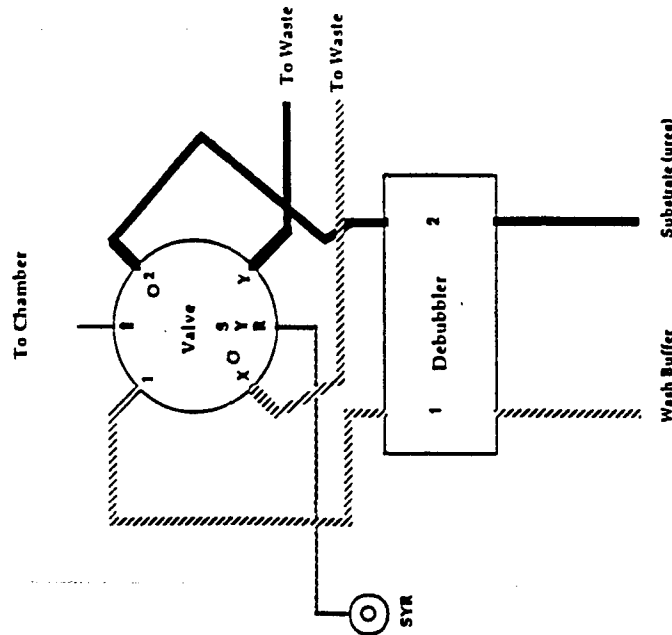


**Fig. Bio-4** Results of experiment on inhibition and regeneration of cholinesterase activity



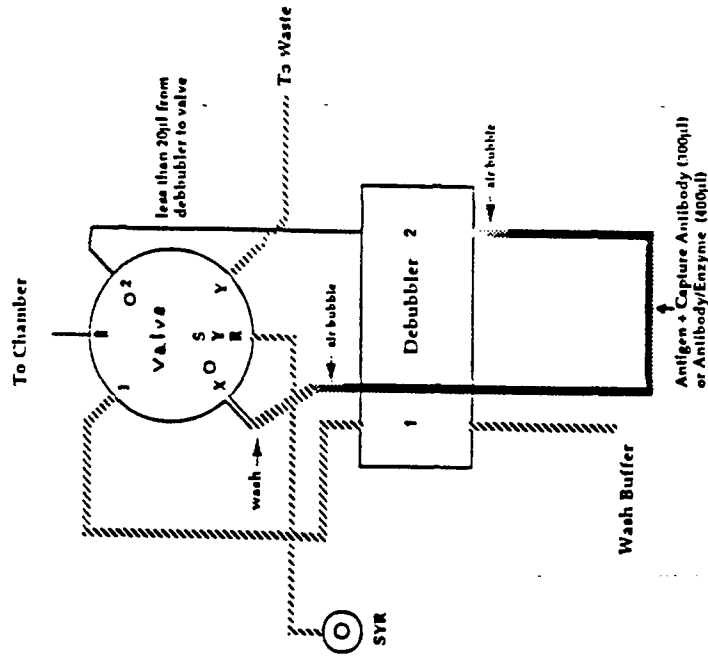
Modification to Cytosensor Chamber Plunger to allow filtration through a 5µm pore NC membrane.

Fig. Bio-5



Fluidic Configuration for Enzyme detection with Urea Substrate

Fig. Bio-6



Fluidic Configuration to filter Antigen + Capture Antibody and Antibody/Enzyme through the NC membrane in the modified plunger

Fig. Bio-7

the debubbler just before delivery to the plunger. After the complete antibody/sample antibody/enzyme complexes have been formed on the membrane, the substrate is delivered to the plunger using the fluidics as setup in Figure Bio-7. Figure Bio-8 shows the measurement of enzyme through the rate of substrate turnover. In the top graph of Figure Bio-8 the switch from urea to wash buffer demonstrates the presence of the enzyme urease on the membrane which can be quantified by the rate of alkalization in the bottom graph. Figure Bio-9 shows three trials with two plungers. The results demonstrate the ability to detect the presence of the sample. More work would be needed to quantify the amount of sample present.

- **Demonstrate device gain by manipulation of transfected receptor density.**
- **Demonstrate device gain by genetic manipulation of second-messenger system.**

The detectability of CBW agents by microphysiometry depends on the sensitivity of both the physical and biological components of the system. Hence, two tasks under the contract involve engineering the cells to increase the biological signal-to-noise ratio.

The first of these tasks was to demonstrate how sensitivity depends on the number of receptors expressed per cell, under the hypothesis that more is better. A rationale for this is the prevalent model of signal transduction whereby the signal depends on the number of activated receptors; with an excess of ligand (the common case), the number of activated receptors is proportional to the total number of receptors expressed. For this work we used a model system in which  $m_1$  and  $m_3$  muscarinic acetylcholine receptors were each expressed in CHO cells at three different levels. The concentration of carbachol (an analog of acetylcholine) necessary to produce 50% of maximum response (EC50) was determined as a function of expression level. More than an order of magnitude improvement in EC50 was observed for high expressors over low expressors for the  $m_1$  system, and varying expression level affected even the detectability of receptor activation for the  $m_3$  system. These results were published in the journal article by Baxter et al. (1994) attached in Appendix 3

The second task in this section was to investigate increasing sensitivity by genetically manipulating signal-transduction (i.e., second messenger) pathways. As a first step, we investigated which biochemical processes were involved in the microphysiometric responses to receptor activation (Baxter et al., 1993; Wada et al., 1993; Davis et al., 1994). One important component was identified as the sodium/proton exchanger (NHE-1) in the plasma membrane. We reasoned that over-expressing NHE-1 was likely to potentiate responses. We therefore stably transfected CHO-K1 cells with the human NHE-1 gene (a gift from J. Pouyssegur, Nice, France). Increased response to the blood-clotting factor thrombin in these cells, compared to wild-type cells, is shown in Fig. Bio-10. Additional work needs to be done to increase the reproducibility of such observations. In other preliminary work, not reported here in detail, we found that CHO-K1 cells expressing the large T antigen of the Epstein-Barr virus can show enhanced responses to the activation of some receptors.

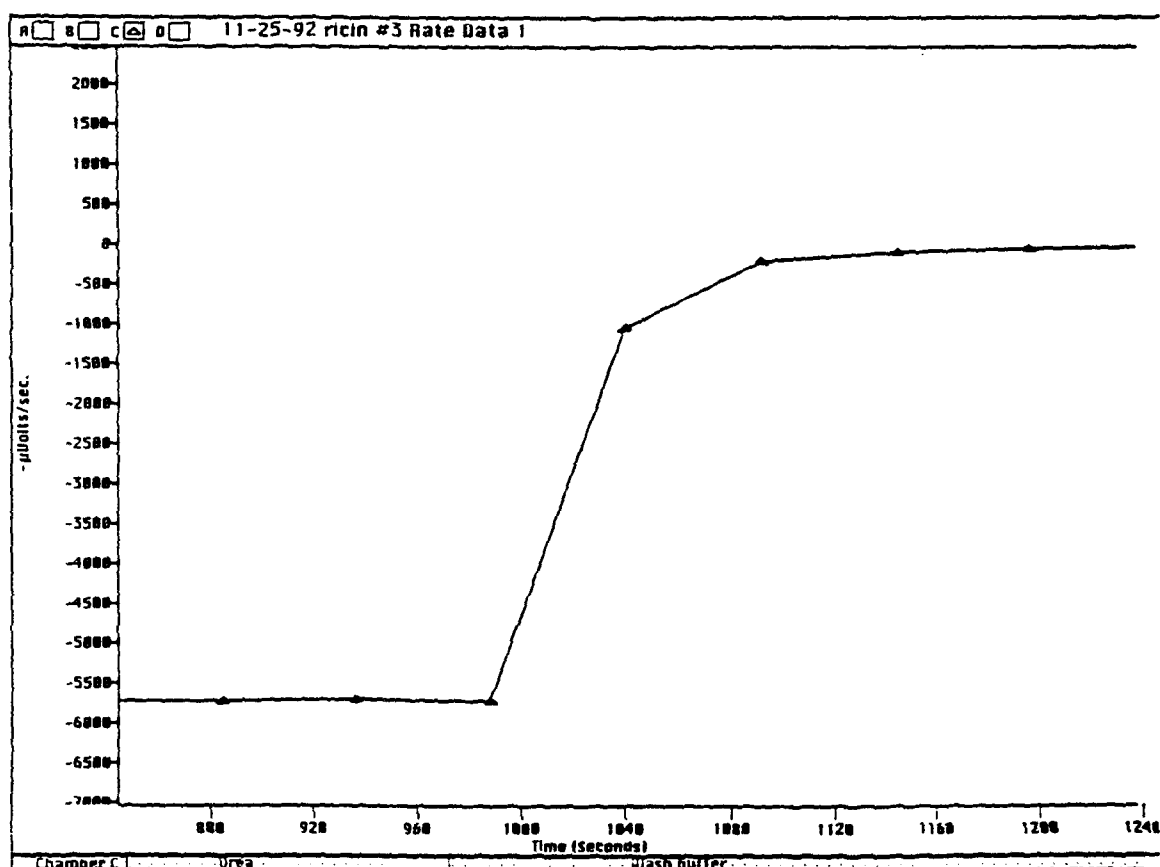
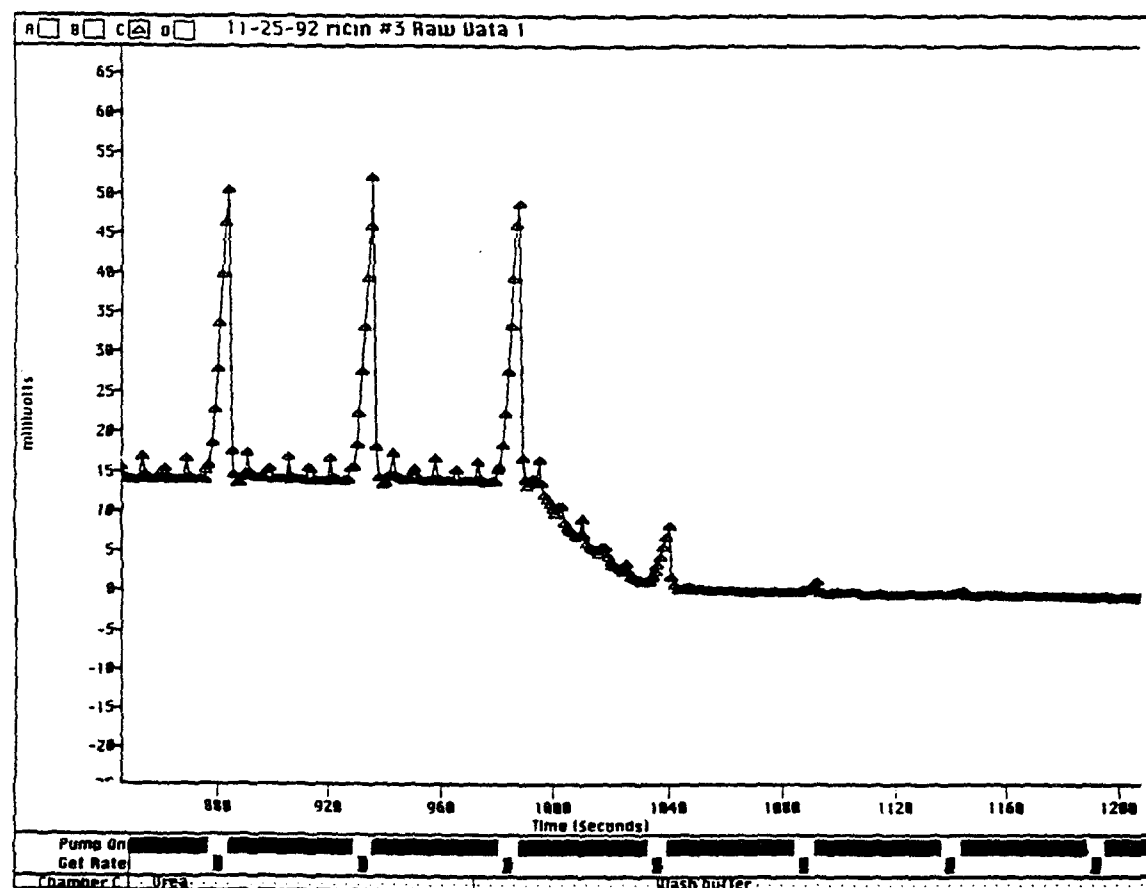


Fig. Bio-8 The urease detection step using Cytosensor™ fluid control. Note that urease activity alkalinizes the solution instead of acidifying it and that the urea substrate washed out after two cycles.

# Repeatability of signal from 0 pg & 2400 pg of ricin

11/25/92

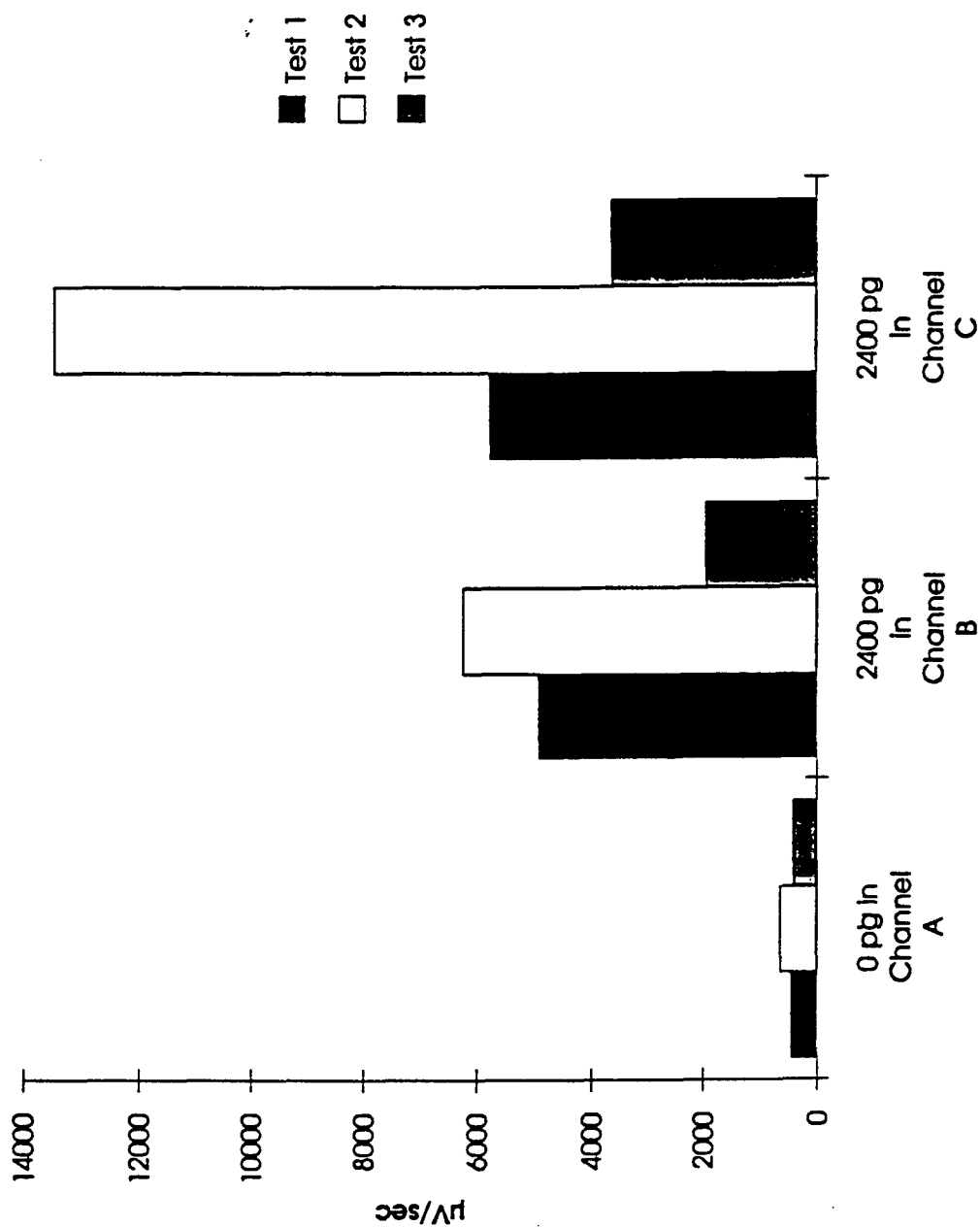
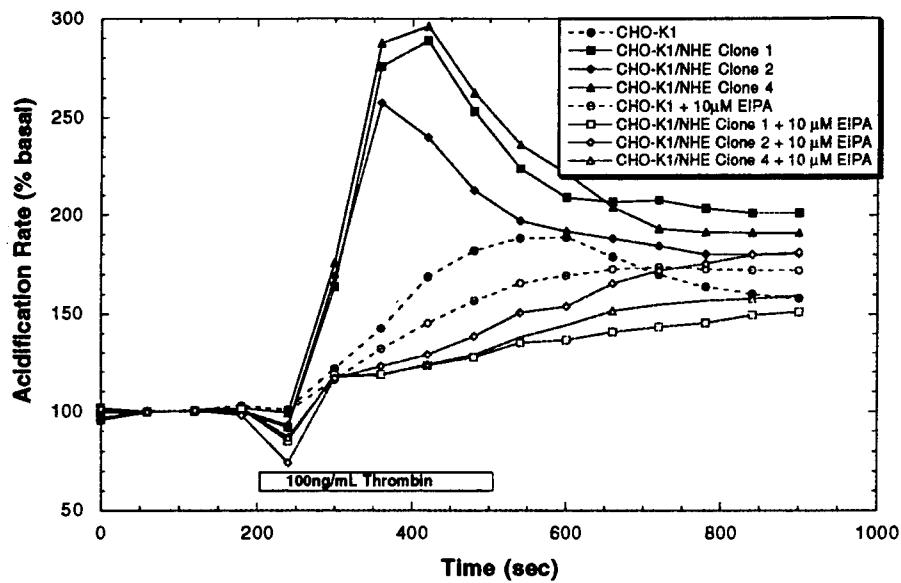


Fig. Bio-9 Detection of 2400 pg of ricin using the immunoassay-modified Cytosensor™

### NHE Inhibitor (EIPA) Eliminates the Enhanced Response to Thrombin in NHE-Transfected CHO-K1 Cells



### Exogenously Expressing NHE Improves Responses to Thrombin in CHO-K1 Cells

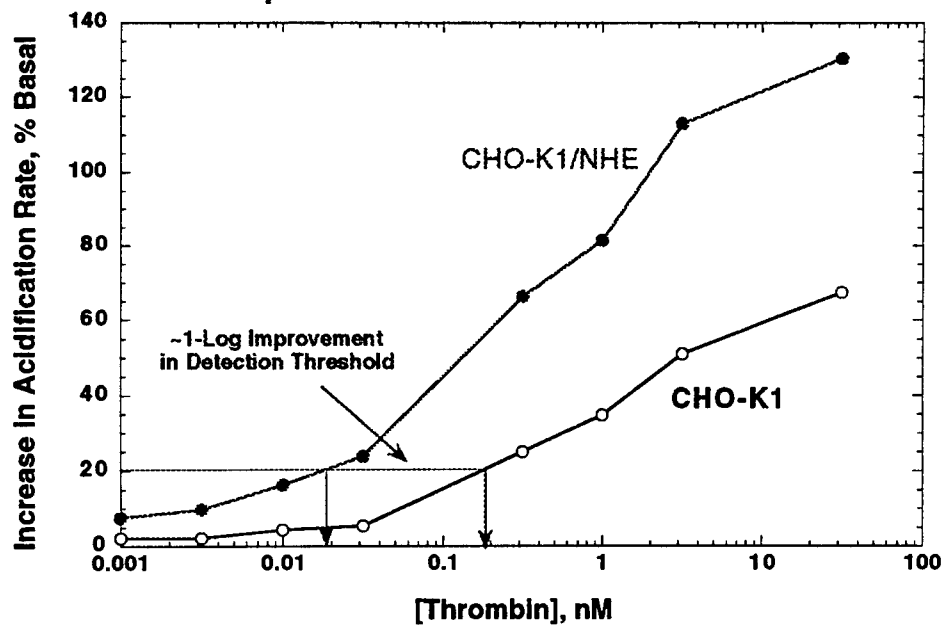


Fig. Bio-10. Enhanced Responses in CHO-K1 Cells Over-Expressing NHE-1

- **Demonstrate mixed-cell system for detection of secondary toxins .**

The goal here was to determine whether microphysiometry can detect the following process: An agent interacts specifically with cell type A, which processes the agent so that it affects a different cell type B. This happens, for example, when a non-toxic precursor molecule is activated by reaction in the liver and then goes on to injure cells in other organs. In collaboration with Prof. Harden McConnell at Stanford, we have tested this "agent pre-processing" concept in another type of model system, drawn from immunology.

The agent in this case is a specific peptide that binds to a cell-surface receptor (a major histocompatibility complex molecule, MHC) on the surface of an antigen-presenting cell; this antigen-presenting cell plays the roll of cell type A. This MHC/peptide pair, still on the surface of the antigen-presenting cell, comes into contact with the T-cell receptor on the surface of a nearby T-helper lymphocyte. The T-helper cell (playing the role of cell type B) becomes activated to carry out a variety of functions. The key point is that the peptide is unable to activate the T-helper cell directly; it first must be processed by an antigen-presenting cell.

In the journal article by McConnell et al. (1995) attached in Appendix 3, we demonstrated the detection of this T-cell activation when T cells and antigen-presenting cells were mixed in the chamber of a microphysiometer and then exposed to peptide. Appropriate controls showed that the signal was indeed derived from the process described in the previous paragraph. It is also interesting to note that the experiments suggest that a small number of MHC/peptide pairs per antigen-presenting cell—perhaps as low as one—are sufficient to generate a detectable signal in the microphysiometer.

- **Demonstrate detection feasibility with all major types of (non-transfected) neuroreceptors.**

In our proposal we stressed the promise of microphysiometry as a general means of detecting receptor activation, largely independent of the mechanisms of signal transduction. A major task was to flesh out the data on this subject that we had acquired at the time of the proposal. We decided to investigate non-transfected neuroreceptors (non-transfected because that was easier, neuroreceptors because the nervous system is the classic target for CBW agents). In fact, the availability of cells expressing transfected receptors (produced by us and by others) was greater than we had anticipated, and much of our work was done with such systems; these are more likely to be representative of the systems used to detect CBW agents than are cells with endogenous receptors.

That goal involving neuroreceptors has been well accomplished and in fact extended to receptors in other systems, such as cardiovascular and immunological. The table below indicates the receptors whose activation has been through our efforts and also the efforts of other scientists who have published pharmacological studies based on work with the commercial version of the microphysiometer.

The table is organized by signal-transduction mechanism, since that is the factor that most influences the behavior and detectability of responses in the microphysiometer. Numerous examples of receptors that work by all the major signal-transduction mechanisms are shown, excluding the slowly acting steroid-family receptors, which are generally inappropriate for microphysiometry. The table excludes an additional 10 to 20 receptors of which the MDC commercial applications group has knowledge but cannot divulge due to proprietary considerations involving customers. Reprints of papers describing the ARPA-assisted detection of many of the receptors are included in Appendix 3.

### Functional Detection of Receptors and Ion Channels by Microphysiometry

Those demonstrated with ARPA support are asterisked.

#### G-Protein Linked

Adrenergic: $\beta_1^*$ , $\beta_2^*$ , $\beta_3$	Angiotensin: $AT_1^*$ , $AT_2^*$
Bradykinin: $B_2$	$\alpha$ -Chemokine: IL-8 <sub>A</sub>
$\beta$ -Chemokine: MIP1 $\alpha$ , MCP1	Cholecystokinin: CCK <sub>A</sub> , CCK <sub>B</sub>
Dopamine: $D_1^*$ , $D_2^*$ , $D_3$ , $D_4$	Endothelin: ET <sub>A</sub>
Histamine: $H_2^*$	Serotonin: 5-HT <sub>1A</sub> <sup>*</sup> , 5-HT <sub>1B</sub> <sup>*</sup> , 5-HT <sub>2B</sub>
Muscarinic: $m_1^*$ , $m_2^*$ , $m_3$ , $m_4$	Opioid: $\mu^*$ , $\delta$ , $\kappa$
Platelet Activating Factor <sup>*</sup>	Prostanoid: EP <sup>*</sup> , FP <sub>2<math>\alpha</math></sub>
Tachykinin: NK <sub>3</sub>	Cation-sensing: CaR

#### Protein Tyrosine Kinase

b-Fibroblast Growth Factor <sup>*</sup>	Epidermal Growth Factor <sup>*</sup>
HER2/HER3 <sup>*</sup>	Insulin <sup>*</sup>
Insulin-Like Growth Factor <sup>*</sup>	Nerve Growth Factor <sup>*</sup>
BDNF (trkB) <sup>*</sup>	

#### Ligand-Gated Ion Channel

GABA <sub>A</sub> <sup>*</sup>	Glutamate (Kainate) <sup>*</sup>
Nicotinic ACh (Muscle Type) <sup>*</sup>	Nicotinic ACh (Neuronal Type)

#### Other Receptors

CD28 <sup>*</sup>	Ciliary Neurotrophic Factor
Granulocyte-Macrophage CSF <sup>*</sup>	$\gamma$ -Interferon
Interleukins: IL-1, IL-2 <sup>*</sup> , IL-3 <sup>*</sup> , IL-4	Surface IgG (Antigen receptor) <sup>*</sup>
T-Cell Receptor <sup>*</sup>	Truncated BDNF (trkB.T1, trkB.T2) <sup>*</sup>
Tum. Necr. Fact. $\alpha$ : TNFR1 <sup>*</sup> , TNFR2 <sup>*</sup>	

#### Ion Channel

Calcium: L <sup>*</sup> , Ryanodine <sup>*</sup>	CFTR
Potassium: IRK1 <sup>*</sup> , IRK2 <sup>*</sup> , KAT1 <sup>*</sup>	Proton: Influenza M <sub>2</sub> <sup>*</sup>



- **Demonstrate LAPS response with transiently transfected human ion-channel receptor.**
- **Demonstrate LAPS response with stably transfected human ion-channel receptor.**

At the time of our original proposal, the scientific literature held few examples of the functional expression of ion-channel receptors by transfection. We expected this to be a hard problem and outlined a variety of approaches that we would take, including beginning with the easier accomplishment of transient transfection and then moving on to the more difficult case of stable expression. In fact, the task turned out to be not as difficult as anticipated. In the five years since we wrote the proposal, a number of labs have worked out means of exogenously expressing ion channels, of both the ligand-gated receptor and voltage-gated types.

We combined the two tasks (transient and stable expression) in this section into one that accomplished the goal of demonstrating a strategy for ion-channel expression that could be of practical use for the detection of CBW agents. That strategy, called semi-stable expression, combines the simplicity of transient transfection with the long-term advantages of stable transfection. Transient transfection is easy, but the expression only lasts a few days because the gene is not incorporated into the host chromosome and cannot replicate outside it; it is lost by nuclease activity or simply by dilution as the cells proliferate. Stable transfection, wherein the gene is incorporated into a host chromosome and therefore replicates with it, requires months of tedious selection to produce a cell line that reliably expresses the receptor. For semi-stable expression, the host cell is engineered to produce proteins that support extra-chromosomal replication of the vector containing the gene of interest. Thus, the gene is maintained over longer periods—weeks to months—by replication without the necessity to screen for the rare insertional events leading to stable expression. Given also that we have demonstrated the efficacy of cryopreserving cells indefinitely, semi-stable transfection is an acceptable strategy for the production of cells exogenously expression ion channels for the purposes of detecting CBW agents. The same conclusion applies to the expression of other proteins, including receptors of other types.

We demonstrated the semi-stable strategy on the expression of the GABA<sub>A</sub> ion-channel receptor in human embryonic kidney 293 cells that had been engineered for semi-stable expression (they were previously stably transfected with the large T antigen from the Epstein-Barr virus). The GABA<sub>A</sub> receptor is a ligand-gated chloride channel that is structurally related to the more familiar nicotinic acetylcholine receptor. While the nicotinic receptor generally mediates neuronal activation, the GABA<sub>A</sub> receptor is usually inhibitory. Antagonists of the GABA<sub>A</sub> receptor, such as picrotoxin, are convulsants. Figure Bio-11 shows typical data for the detection of the activation of transfected GABA<sub>A</sub> receptors in our hands. Such results were obtained as early as a week after the transfection protocol was begun and were maintained for at least two months without cryopreservation.

# GABA Response of 293 Cells Semi-Stably Expressing the GABA<sub>A</sub> Receptor

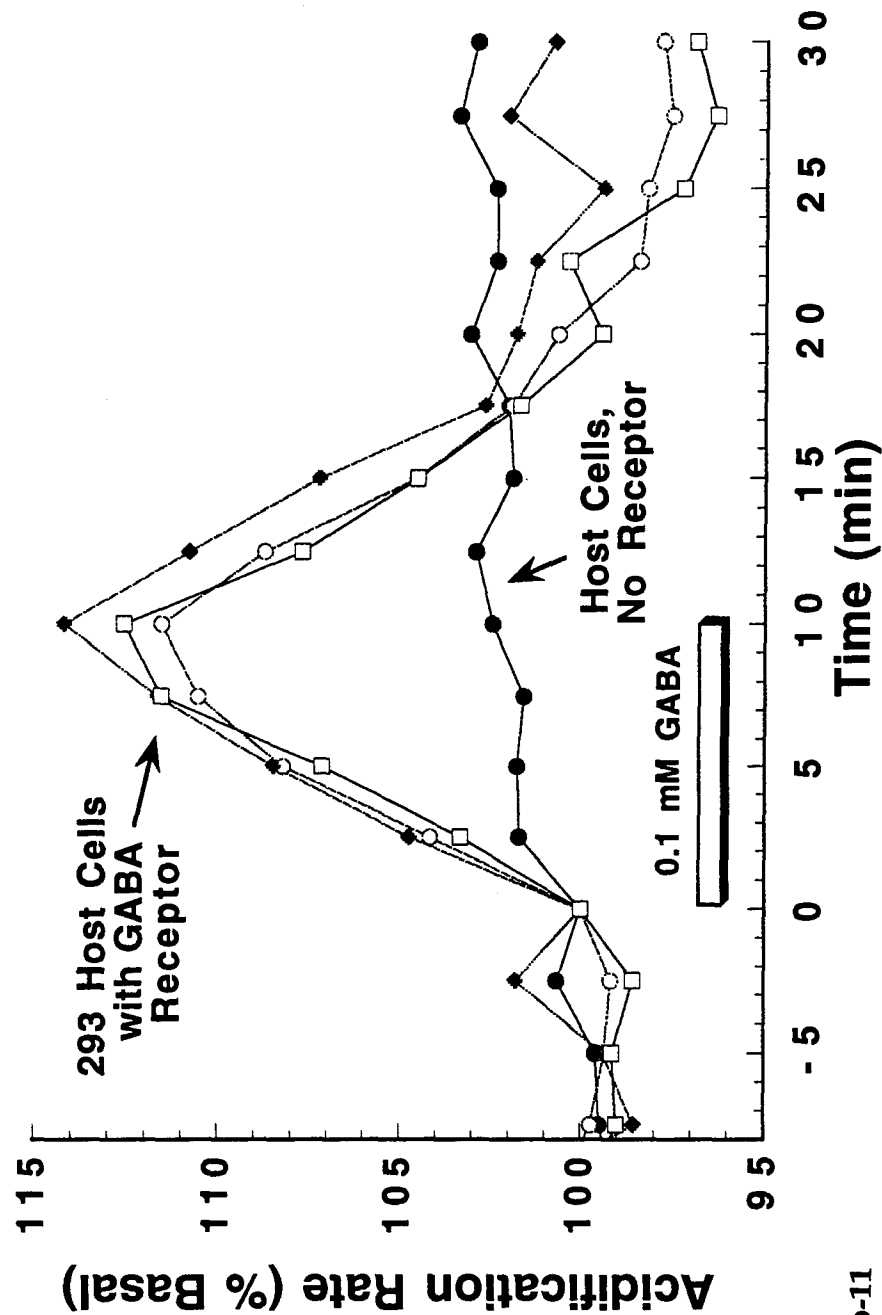


Fig. Bio-11